A study of interhemispheric magnetic conjugacy and large scale magnetosphere-ionosphere coupling using SuperDARN radars

Bharat Simha Reddy Kunduri

Dissertation submitted to the faculty of the Virginia Polytechnic Institute and State University
in partial fulfillment of the requirements for the degree of

Doctor of Philosophy
in
Electrical Engineering

Joseph B. H. Baker, Co-Chair
J. Michael Ruohoniemi, Co-Chair
Scott M. Bailey
Wayne A. Scales
Kathleen Meehan
Kevin A. Shinpaugh

Nov 8, 2013
Blacksburg, Virginia

Keywords: SuperDARN, interhemispheric conjugacy, magnetosphere, ionosphere

A study of interhemispheric magnetic conjugacy and large scale magnetosphere-ionosphere coupling using SuperDARN radars

Bharat Kunduri

ABSTRACT

Ionospheric convection dynamics is an important window for understanding the coupling of the solar wind and interplanetary magnetic field to the Earth's ionosphere and upper atmosphere. In this study, we use measurements of ionospheric convection made by the SuperDARN radars to investigate the role of interhemispheric magnetic conjugacy in magnetosphere-ionosphere coupling and study the large-scale interactions between the magnetosphere and ionosphere. SuperDARN radars cover large geographic regions in both hemispheres and have a dataset spanning more than a decade, making them ideal for such studies. We begin in chapter 2 with an analysis of the degree of interhemispheric conjugacy exhibited in a Sub-Auroral Polarization Stream (SAPS). We present simultaneous observations of a SAPS event in both hemispheres made by mid-latitude SuperDARN radars with magnetically conjugate fields-of-view. An interhemispheric comparison of the characteristics of the SAPS channel reveals that the channel was conjugate in terms of potential variations across the channel even though substantial differences in latitudinal width and electric fields were observed in the channel. In chapter 3, we use interhemispheric SuperDARN observations of high latitude ionospheric convection in the noon-dusk sector to investigate the effects of IMF B_Y penetrating into the closed magnetic field line region. The observations support the existence of an IMF B_Y associated interhemispheric potential difference and field-aligned current system resulting in the generation of the interhemispheric asymmetries in ionospheric convection. Four events are analyzed in this study and the strength of interhemispheric currents associated with IMF B_Y are estimated. Moreover, the strength of the interhemispheric currents is found to depend on the magnitude of IMF B_Y, proximity of the currents to open-closed field line boundary, ionospheric conductivity and magnetic local time. In chapter 4, we use data from the mid-latitude SuperDARN radars between Jan-2011 and Aug-2012 to compile a database of SAPS events spanning about six hours in magnetic local time. The event database is used to analyze the average spatial variations in the occurrence rate and velocities of the SAPS channel under different geomagnetic conditions. An empirical model based on Dst-index is then developed to estimate the occurrence rate of SAPS at a given latitude and magnetic local time.

Acknowledgments

I would like to start by thanking my advisors, Dr. Jo Baker and Dr. Mike Ruohoniemi, for giving me an opportunity when I needed one and for their guidance and support over the last several years. This dissertation would not have been possible without their encouragement. I take this opportunity to thank them for providing a great environment in the lab and encouraging me to learn about Python and many other software packages. I would also like to thank all my committee members for accepting to be on my committee and for all their valuable suggestions. A special thanks goes to all of my labmates for always keeping me motivated. I would like to specially mention Dr. Sebastien de Larquier, Evan and Dr. AJ Ribeiro for their advice, support and mentoring. It has been a really great experience working with you guys. Thank you Dr. Lasse Clausen for all the guidance and for showing great patience while answering my questions during my first year at Virginia Tech. A special thanks to Debbie Collins for making Space@VT a great place to work. I thank my friends Vishal and Aditya for their support and encouragement. Finally, I am deeply thankful to my parents for supporting me in innumerable ways and being a great source of strength at every stage of my life.

Contents

List of Figures

List of Tables

Chapter 1

Introduction

The near-Earth space environment consists of three major components : the magnetosphere, the ionosphere, and the solar wind. Together these three components form a tightly coupled interactive system. In this introductory chapter, we provide an overview of near-Earth space physics and finish with a description of the Super Dual Auroral Radar Network (SuperDARN).

1.1 The solar wind

The solar wind is a supersonic stream of plasma flowing away from the Sun in all directions [*Kivelson and Russell*, 1995]. The solar wind originates in the Sun's outer atmosphere (the corona) and flows into the interplanetary space creating the heliosphere : an enormous plasma bubble encompassing the entire solar system. Solar wind plasma is charge-neutral, (i.e., composed of roughly equal amount of ions and electrons), with most ions being protons (∼95 %) with small traces of helium and other heavier ions [*Hundhausen*, 1972]. The ion temperatures are typically of the order of 10^5 K and the number density tends to be a few protons / cm^3 [*Parker*, 1963]. Typically, the solar wind velocity varies between 300 and 700 km/s. The solar wind also carries remnant part of the Sun's magnetic field called the interplanetary magnetic field (IMF) [*Parker*, 1963; *Brandt*, 1973]. The IMF and solar wind plasma move together because charged particles are tightly bound to a magnetic field line

and always remain fixed to that field line. So as the plasma moves outward from the Sun, the magnetic field lines move along with it. This is called the "frozen-in-flux" condition. The magnitude of the IMF is variable over a range of values as low as 1 nT to values greater than 50 nT [*Kivelson and Russell*, 1995].

1.2 The Magnetosphere

The interaction between the solar wind and the Earth's magnetic field plays a significant role in influencing near-Earth space weather conditions. *Chapman and Ferraro* [1930] suggested the Earth's magnetic field acts as an obstacle to the solar wind plasma. The solar wind dynamic pressure confines of the Earth's quasi-dipolar magnetic field inside a cavity called the magnetosphere, which has a long comet-like tail and compressed dayside facing the Sun. The outer boundary of the magnetosphere (the "magnetopause") is the location where the pressure of the magnetic field and plasma inside the cavity maintain an equilibrium with the shocked solar wind dynamic pressure. Figure 1.1 shows an illustration of the Sun, the space along with solar wind, the IMF, and the Earth's magnetosphere. When the solar wind blows hard the cavity shrinks, and, when its pressure reduces, the cavity expands. Likewise, the IMF has an important role in determining the location of the magnetopause via magnetic reconnection (explained in section 1.3). The magnetosphere typically extends to about 15-20 R_E (Earth radii) on the dayside and stretches beyond 200 R_E on the nightside [*Schunk and Nagy*, 2009].

The Earth's magnetosphere is the region where the motion of charged particles is dominated by Earth's magnetic field. It shields Earth from the solar wind and other sources of radiation from space. In the absence of external influences, the Earth's magnetic field would be quasi-dipolar in nature, similar to that of a bar magnet. However, the changing solar wind and IMF conditions play an important role in distorting the shape and size of the

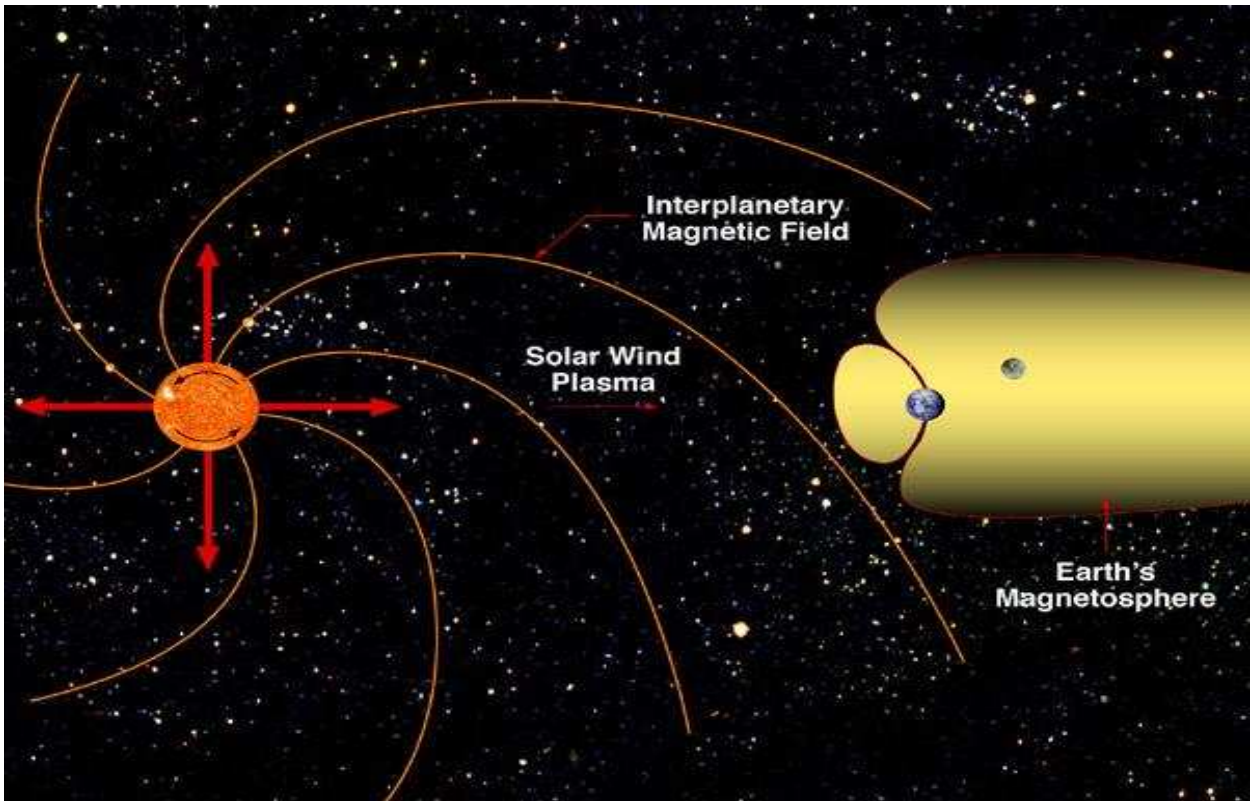

Figure 1.1: A cartoon showing the solar wind, interplanetary magnetic field (IMF) and the Earth's magnetosphere. Courtesy NASA.

magnetosphere and make it very dynamic. Some of the most important plasma regions and current systems in the magnetosphere are shown in Figure 1.2.

As mentioned before, the magnetopause separates geomagnetic field from solar wind and interplanetary space, suggesting the Earth's magnetic field immediately outside the magnetopause should be zero. This implies magnetopause is a current sheet (a common feature with most plasma boundaries [*Kivelson and Russell*, 1995]), which produces a magnetic field opposite in direction to the geomagnetic field outside the boundary. As shown in Figure 1.2, this current sheet is called the magnetopause current sheet. The magnetopause can further be divided into three distinct types of boundary layers based on the characteristics of the plasma (density, composition and flow) : the Low Latitude Boundary Layer (LLBL), the

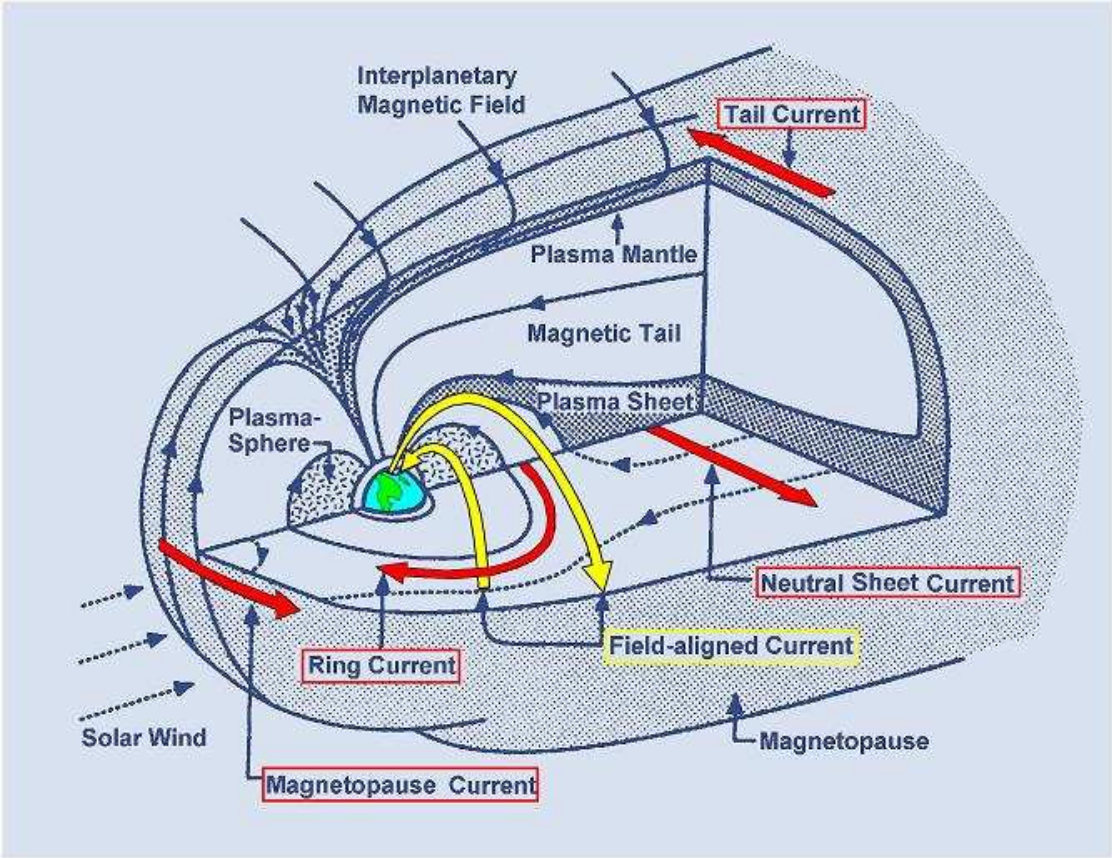

Figure 1.2: Plasma regions and current systems in the magnetosphere. See text for details. Courtesy NASA.

entry layer/high-altitude cusp, and the High Latitude Boundary Layer (HLBL) [*Kivelson and Russell*, 1995]. The region inside the magnetopause can broadly be divided into two subregions : the inner magnetosphere and the outer magnetosphere.

The outer magnetosphere is a reservoir of plasma and energy of solar wind origin and has a strong influence on the behavior of the inner magnetosphere. The nightside outer magnetosphere is divided into two lobe regions by a current sheet, which separates the oppositely directed magnetic fields emanating from the polar regions : the northern lobe (field is directed towards the Earth) and the southern lobe (field is away from the Earth). The current/plasma sheet typically consists of hot plasma (kilovolt) with densities varying

between 0.1-1 cm^{-3} [*Kivelson and Russell*, 1995]. Compared to the plasma sheet, the tail lobes have much lower plasma densities, typically less than 0.1 cm^{-3} with energies in the range of 5-50 keV. This is because the tail lobe magnetic field is "open" to the solar wind and the plasma can easily escape [*Kivelson and Russell*, 1995; *Schunk and Nagy*, 2009].

The inner magnetosphere has two main regions: (i) a trapped highly energetic plasma population consisting of two radiation belts (inner belt and an outer belt) and ring current and (2) a trapped low energy plasma population called the plasmasphere. The radiation belts consist of energetic particles trapped by the Earth's magnetic field and drifting across the magnetic field lines. Energies vary from a few keV to MeV [*Schunk and Nagy*, 2009]. Typically, the location of the inner belt varies between 1.5 to 3 R_E and the outer belt between 3 to 6 R_E [*Kivelson and Russell*, 1995]. Generally, the outer radiation belt is very dynamic with a strong dependence on the geomagnetic conditions [*Schunk and Nagy*, 2009] while the inner belt is relatively more stable. Very recent evidence from the Van Allen Probes spacecraft mission suggests the existence of a transient third radiation belt region [*Baker et al.*, 2013]. Differential gradient-curvature drift of energetic ions and electrons in the radiation belts produces an inner magnetosphere ring current, which flows westward around the Earth in the equatorial plane at locations varying between 2 to 7 R_E [*Kivelson and Russell*, 1995]. The highly dynamic nature of the ring current has primarily been attributed to injection of plasma into the outer radiation belt during periods of intense solar wind - magnetosphere coupling (geomagnetic storms). Finally, the plasmasphere is the region of the inner magnetosphere consisting of dense low energy plasma. It begins just above the Earth's upper atmosphere and generally co-exists in the same region as the radiation belts. Particles in the plasmasphere typically have densities on the order of 10^3 cm^{-3} and energies of $\sim$1 eV [*Kivelson and Russell*, 1995; *Schunk and Nagy*, 2009]. One of the important motivations for studying the magnetosphere is the fact that processes occurring in the magnetosphere

couple to the conducting layers of Earth's upper atmosphere through the highly conducting magnetic field lines.

1.3 The Dungey Cycle

One of the most important processes in the solar wind - magnetosphere interaction is the Dungey Cycle, [*Dungey*, 1961] which plays an important role in influencing the shape, size and electrodynamics of the magnetosphere.

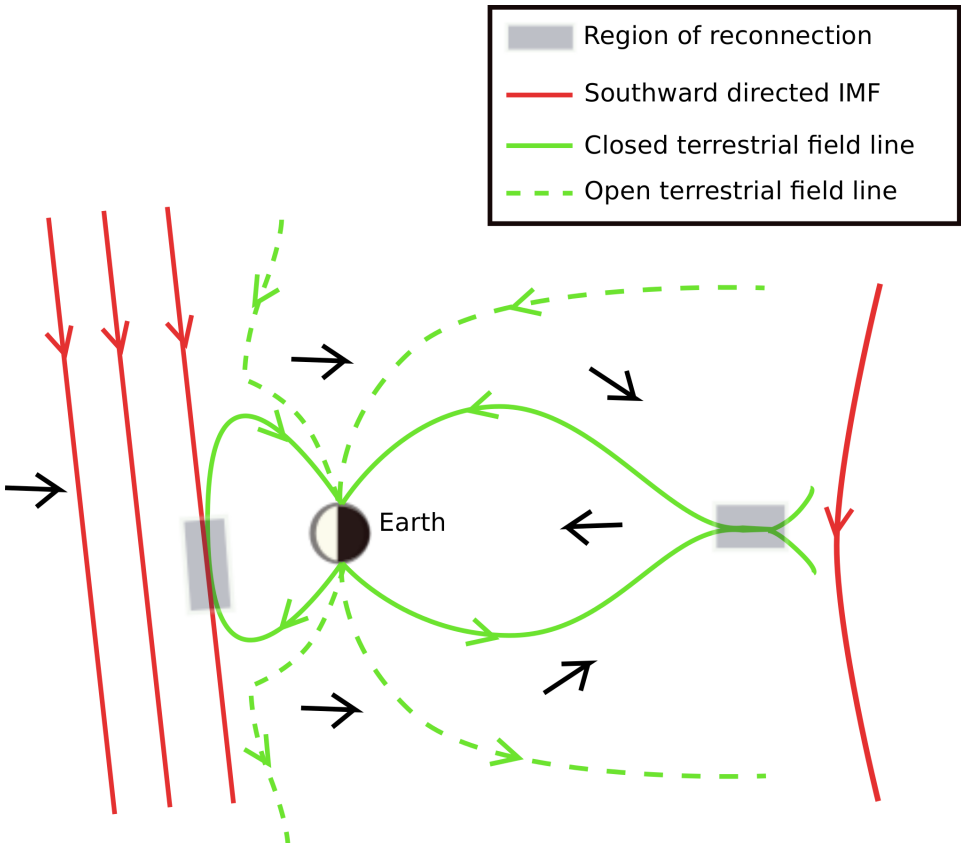

Figure 1.3: Duskside view of Dungey Cylcle. Magnetic reconnection occurs at the shaded regions. The direction of motion of the field lines is indicated by the black arrows.

Dungey [1961] suggested "magnetic reconnection" between the IMF and terrestrial magnetic field was the driving mechanism for energy transfer and the generation of plasma cir-

culation in the magnetosphere. Magnetic reconnection is the process whereby oppositely directed magnetic field lines essentially cut and merge with each other, thereby enabling plasma populations to transfer between the field lines. This scenario is most likely to occur when the B_Z component of IMF is negative/southwards and, thus, directed anti-parallel to the south-north orientation of the terrestrial magnetic field lines on the dayside. This process is illustrated in Figure 1.3. Reconnection between the IMF and geomagnetic field on the dayside leads to the generation of two new field lines of mixed character such that one end is attached to the Earth (one each in the northern hemisphere and the other in the southern) and the other end is "open" stretching out into interplanetary space. As the solar wind continues moving past the Earth, it pulls these two newly opened field lines anti-sunwards. Eventually, the magnetic tension becomes so great that two the open field lines move towards the center of the nightside tail where they "reconnect" back to each other to form a newly closed terrestrial field line and an IMF field line once more. The IMF field line eventually rejoins the solar wind flow while the terrestrial field convects back towards the dayside around the dawn or the dusk flanks thus closing the circuit. Because plasma is bound to the magnetic field lines, this motion of the field lines thus governs the motion of plasma in the magnetosphere. The Dungey Cycle, thus, provides a physical basis to explain the flow of plasma in the magnetosphere, called magnetospheric convection.

In the next subsection, we present a brief overview of the conducting layer of the Earth upper atmosphere, which couples with the magnetosphere - the ionosphere. We, then, present a discussion on the electrodynamic coupling between the magnetosphere and ionosphere.

1.4 Ionosphere

The ionosphere is the ionized region of the Earth's upper atmosphere. It generally stretches between 50 km to the edge of space at about 1000 km above the surface of the

Earth [*Kivelson and Russell*, 1995]. The ionosphere is a relatively weak plasma because it still has a significant number of neutrals [*Schunk and Nagy*, 2009; *Kelley*, 2009]. For this reason, it makes sense to think of the ionosphere (charged) and atmosphere (neutral) as being collocated. Figure 1.4 presents a temperature (left) and plasma density (right) profile of the Earth's atmosphere and ionosphere, respectively. The two main sources for the ionization are photoionization caused by EUV and UV radiation from the Sun and energetic particle precipitation (mainly from the plasma sheet) [*Kivelson and Russell*, 1995]. Photoionization is the dominant source for producing the low latitude dayside ionosphere while energetic electron precipitation is the dominant source on the nightside at higher (auroral) latitudes.

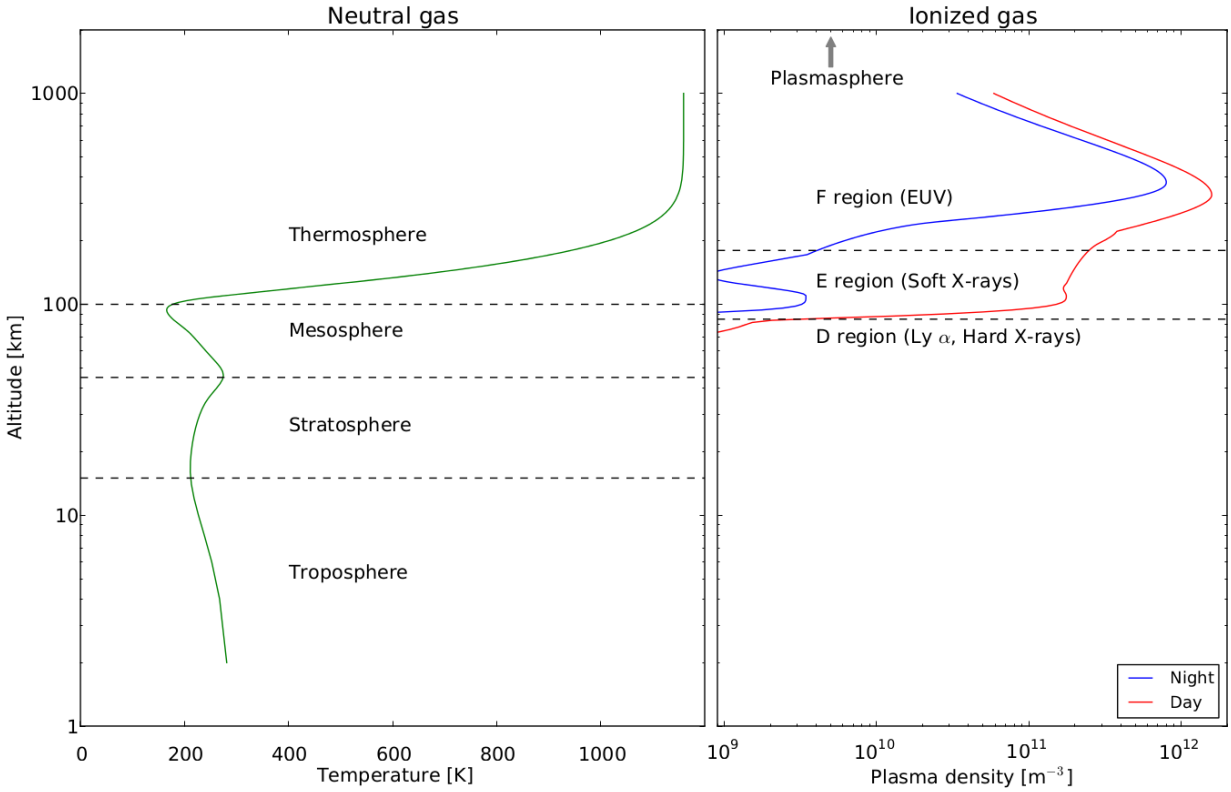

Figure 1.4: Altitude profiles of temperature in the atmosphere (left) and plasma density in the ionosphere (right).

The ionosphere is divided into three major regions. The lowest region below 90 km is

the D region and tends to disappear at night, the region between 90 to 150 km is called the E region and F region is the region above 150 km. The F region has the maximum plasma density in the ionosphere and is often further divided into F_1 and F_2 regions. The dominant species in the D region are molecular ions and neutrals and this region is composed of both positive and negative ions. The primary ions in the D region include NO^+ and O_2^+ while the neutral species include NO, CO_2, H_2O, O_3 [*Schunk and Nagy*, 2009]. The dominant ions in the E region are NO^+, O_2^+ and N_2^+ whereas O^+ is the dominant ion in the F region. In the next section, we discuss the various electrodynamic process in the ionosphere.

1.5 Magnetosphere-Ionosphere Coupling

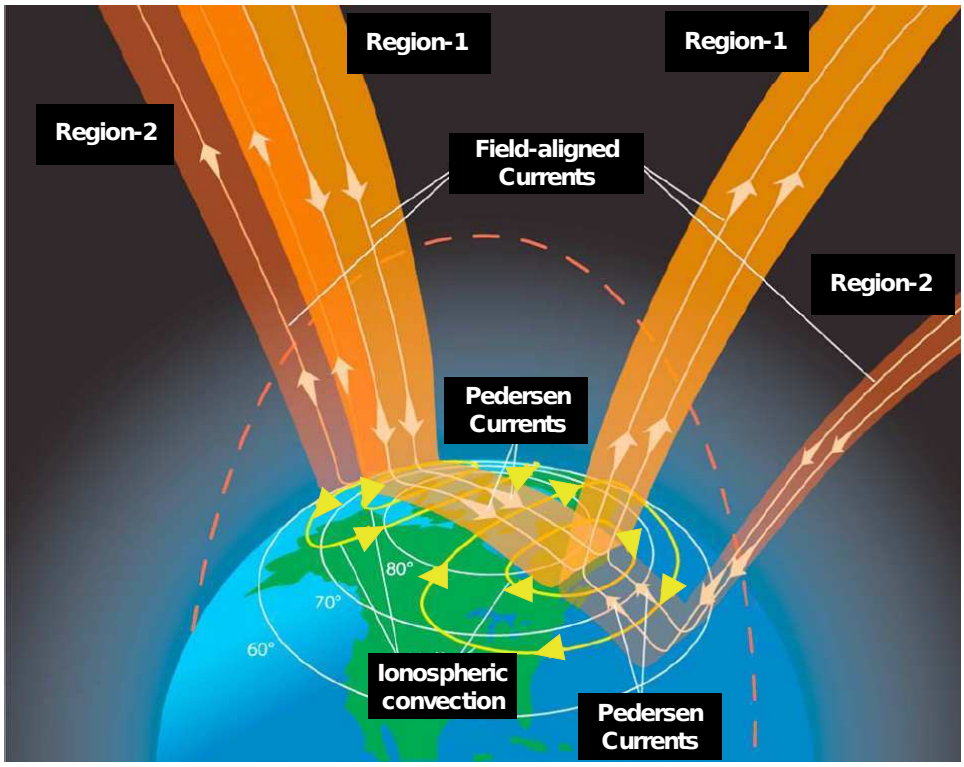

Figure 1.5: A cartoon demonstrating how field-aligned currents and electric fields couple the magnetosphere and ionosphere together. Adapted from *Le et al.* [2010].

The conducting ionosphere and the magnetosphere form a tightly coupled interactive

system in the near Earth space environment. Important electrodynamic parameters such as electric field , field-aligned current, and precipitating energetic charged particles are closely linked between the two regions, via the highly conducting magnetic field lines. Figure 1.5 ([*Le et al.*, 2010]) shows how the major current systems of the magnetosphere are connected to the ionosphere via the Region-1 and Region-2 field-aligned current systems. Namely, the magnetopause current is connected via the Region-1 field aligned currents and the ring current via the Region-2 field-aligned currents. The Region-1 currents flow into the ionosphere on the dawn side and leave it on the duskside. The Region-2 currents flow into the ionosphere on the dusk side and leave it on the dawn side. Pedersen currents provide current closure for the Region-1 and Region-2 current systems in the ionosphere. Another important manifestation of magnetosphere-ionosphere coupling is ionospheric convection. In section 1.3, we described the Dungey Cycle and its role in driving magnetospheric convection. This magnetospheric convection is mirrored in the ionosphere as the two cell convection pattern (shown by the yellow colored lines in Figure 1.5) produced by the $\mathbf{E} \times \mathbf{B}$ drift motion of plasma in the ionosphere. Here, $\mathbf{E}$ is the solar wind electric field mapping down into the ionosphere and $\mathbf{B}$ is the geomagnetic field [*Kivelson and Russell*, 1995]. At latitudes close to the poles (generally greater than 80° magnetic latitude) in the region of open magnetic field lines, plasma convects from the dayside towards the night side. At lower auroral latitudes, the plasma convects back to the dayside on closed field lines along the dawn and dusk flanks, completing the cycle. Finally, there are energetic charged particles, which spiral along the magnetic field lines and impact the Earth's ionosphere/atmosphere to produce aurora (or the northern lights). These particles originate in the plasma sheet and their precipitation maps into the ionosphere as an oval shaped region, termed the auroral oval. The auroral particles modify the background ionospheric conductance and, thus, play an important feedback role in modifying magnetosphere-ionosphere coupling.

1.6 Interhemispheric Magnetic Conjugacy

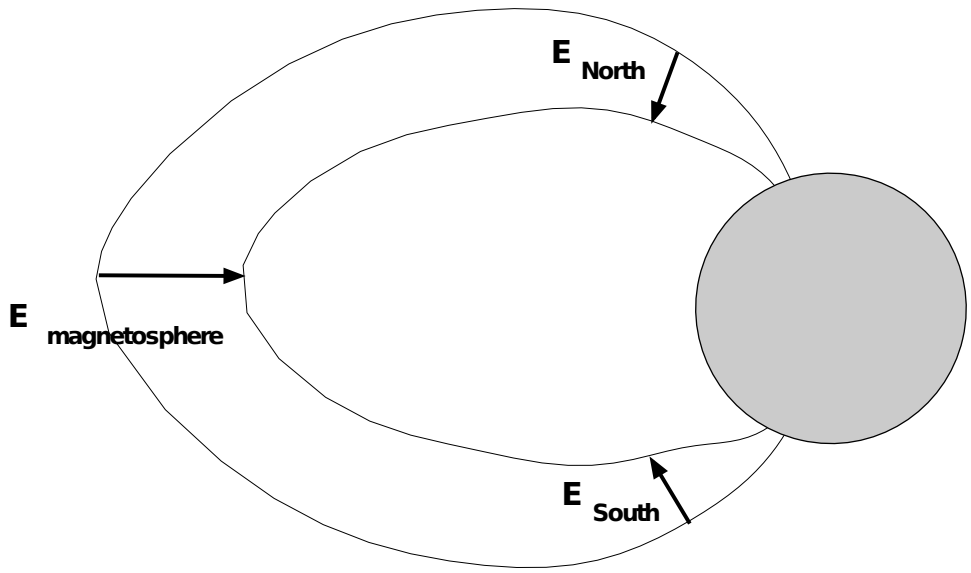

Figure 1.6: Interhemispheric conjugacy : Magnetospheric electric fields ($E_{magnetosphere}$) map equally into both hemispheres along magnetic field lines such that E_{north} and E_{south} should be similar.

Generally speaking, magnetic field lines can be assumed to behave like good conductors and are often treated as electrostatic equipotentials to the first order. Any potential difference should be neutralized by charged particles spiraling along the field line. This assumption implies that electrodynamic events occurring on closed magnetic field lines should be very similar at the northern and the southern ionospheric footprints, as shown in Figure 1.6. This is termed interhemispheric magnetic conjugacy. An example of such conjugate phenomenon occurring in the northern and the southern hemispheres is provided in Figure 1.7 (adapted from *DeWitt* [1962]), which shows all sky imager data from magnetically conjugate regions exhibiting a high degree of correlation in their dynamic variations in auroral luminosity, form, and motion. The observations clearly demonstrate that aurora occur simultaneously in both hemispheres. Of particular note in the figure is the increase in luminosity of aurora in both hemispheres simultaneously between 0930 and 1000 UT. This being said, several factors

such as ionospheric conductivity, geomagnetic disturbance level, and IMF can be expected to modify this picture and produce asymmetries between the hemispheres [*Sato et al.*, 1998; *Milan et al.*, 2001; *Kozlovsky et al.*, 2003]. For example, an increase in geomagnetic activity due to intense solar wind and IMF conditions can distort the configuration of the geomagnetic field lines, leading to asymmetric mapping of electric fields between hemispheres, as shown in Figure 1.8. On the left is a uniform grid of equal sized MLAT/MLT (magnetic latitude/magnetic local time) cells corresponding to the northern hemisphere (in blue color). On the right is the configuration when each of these northern hemisphere grid cells is traced into the southern hemisphere (in red color) using the Tsyganenko 'T01' magnetic field model [*Tsyganenko*, 2002a]. It can be observed that the traced grid is distorted and exhibits significant differences in the size and shape of the cells, especially at higher latitudes. This difference in the size/shape of the cells suggests that electric fields can map asymmetrically between hemispheres even when the magnetic field lines might behave like equipotentials.

An example of this sort of interhemispheric asymmetry in ionospheric electrodynamic phenomenon is presented in Figure 1.9, which shows simultaneous auroral images obtained from all sky imagers located in Husafell, Iceland and Syowa Station, Antarctica. These imagers are located at magnetically conjugate locations according to the IGRF model [*Finlay et al.*, 2010]. A detailed analysis of this particular event is presented in [*Sato et al.*, 1998] and the main feature to observe is that the spatial extent of the aurora seen at Syowa was larger than the aurora observed in Iceland. In this case, non-conjugate features observed during the event were attributed to the presence of interhemispheric field-aligned currents.

Events like this one serve to show how simultaneous and magnetically conjugate observations can be effectively used to further our understanding of the important role that factors such as ionospheric conductivity and geomagnetic field configuration play in producing and interhemispheric distortion in magnetosphere-ionosphere coupling. One dataset that

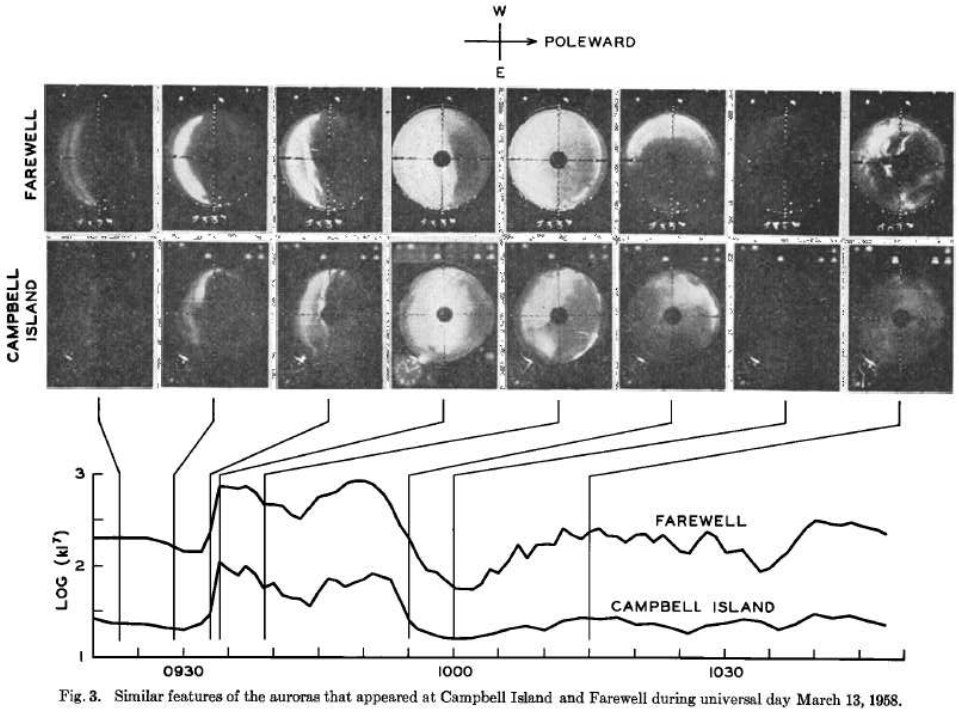

Fig. 3. Similar features of the auroras that appeared at Campbell Island and Farewell during universal day March 13, 1958.

Figure 1.7: All sky imager data from Farewell (northern hemisphere) in Alaska and Campbell Island (southern hemisphere) in New Zealand. The bottom most panel shows the variations in the luminosity of the aurora at both locations and can be seen to be very similar. Adapted from *DeWitt* [1962].

has been under-utilized for this purpose is the database of the SuperDARN radar network.

1.7 SuperDARN HF Radars

The Super Dual Auroral Radar Network (SuperDARN) is an international chain of radars, which measures the Doppler motion of ionospheric plasma over large geographical areas in both hemispheres [*Greenwald et al.*, 1985; *Chisham et al.*, 2007]. SuperDARN radars are low power (at ∼10 kw) and operate continuously throughout the year. SuperDARN radars are sensitive to coherent scatter from decameter-scale magnetic field-aligned

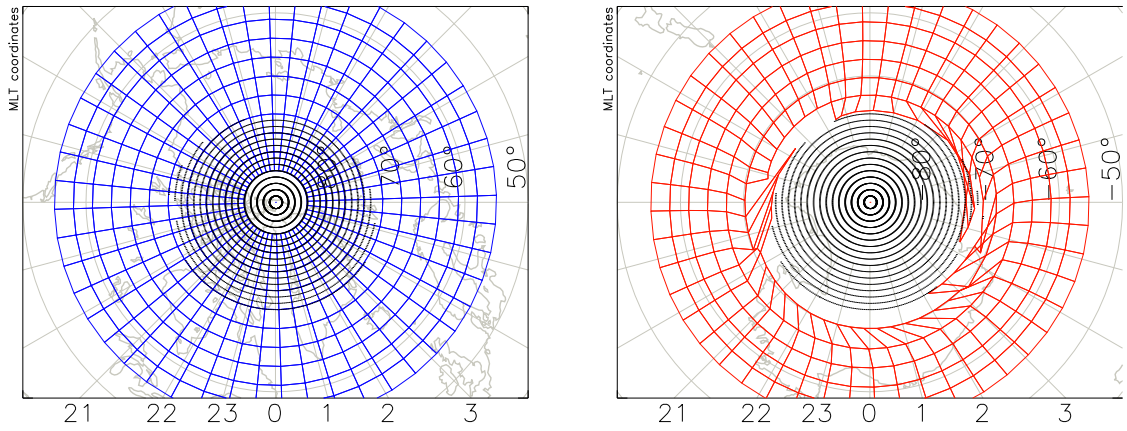

Figure 1.8: A grid of magnetic field lines (Tsyganenko 'T01' model [*Tsyganenko*, 2002a]) indicating level of distortion in field lines between hemispheres. The map on the right side shows a uniform grid of points overlayed on the northern hemisphere. The map on the right side shows the same grid formed in the southern hemisphere by tracing each edge of the northern hemisphere grid along magnetic field lines. The concentric circles indicate the open field line region.

irregularities in the F-region of the ionosphere [*Greenwald et al.*, 1985; *Ruohoniemi et al.*, 1987]. The Doppler shift of the backscattered signal is proportional to the line-of-sight component of the $\mathbf{E} \times \mathbf{B}$ drift in the scattering region [*Ruohoniemi et al.*, 1987]. SuperDARN radars usually operate in the 8-18 MHz (High Frequency) range. An important reason for choosing this band is to utilize refraction in the ionosphere to bend the signal so that the rays propagate nearly horizontally and thus orthogonal to the magnetic field to maximize cross section for the refraction from the field-aligned irregularities. Another effect of HF refraction is that the radar rays can be refracted back to the Earth's surface, resulting in backscatter from the ground (i.e., ground scatter).

In standard operating mode, SuperDARN radars use electronic phasing to steer an array of antennas through 16-24 beam directions covering an azimuth of $\sim 50°$. The radar typically dwells for 3.5 or 7 seconds on each beam along which line-of-sight measurements of the velocity are obtained in range gates separated by 45 km. The radar dwell time corresponds to the completion of a full azimuth scan in 1 or 2 minutes [*Chisham et al.*,

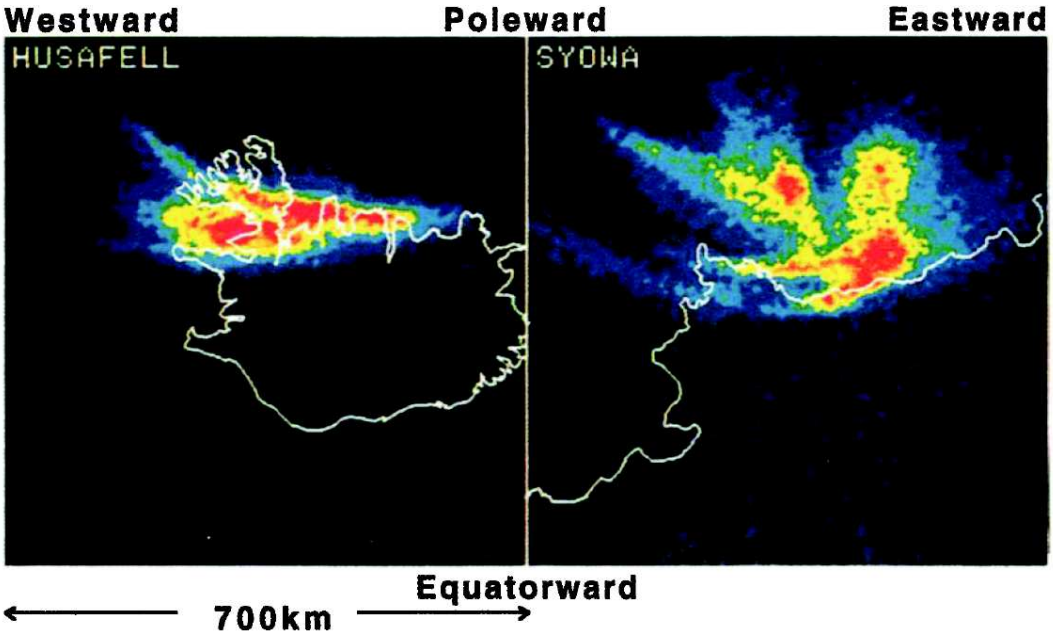

Figure 1.9: Simultaneous all sky images at conjugate regions (determined from IGRF model) in Husafell, Iceland (Northern Hemisphere) and Syowa Station, Antarctica (Southern Hemisphere). The spatial extent of aurora observed in the southern hemisphere was larger than the aurora observed in the northern hemisphere. Adapted from *Sato et al.* [1998].

2007]. An example of line-of-sight Doppler velocity measurements made by the Goose Bay (GBR) SuperDARN radar during one such full azimuth scan is presented in Figure 1.10. In the figure the low velocity (less than 25 m/s) gray portion of the velocities indicates the ground scatter whereas the colored portion indicates line-of-sight Doppler velocities from ionospheric backscatter. The velocities are color-coded according to the scale on the right, with positive velocities indicating flows towards the radar and negative velocities indicating flows away from the radar.

At the present time, the SuperDARN network consists of 32 radars that continuously monitor plasma dynamics in both the hemispheres and are operated by more than a dozen institutes around the world. The collective fields-of-view of the radars in both hemispheres is presented in Figrue 1.11.

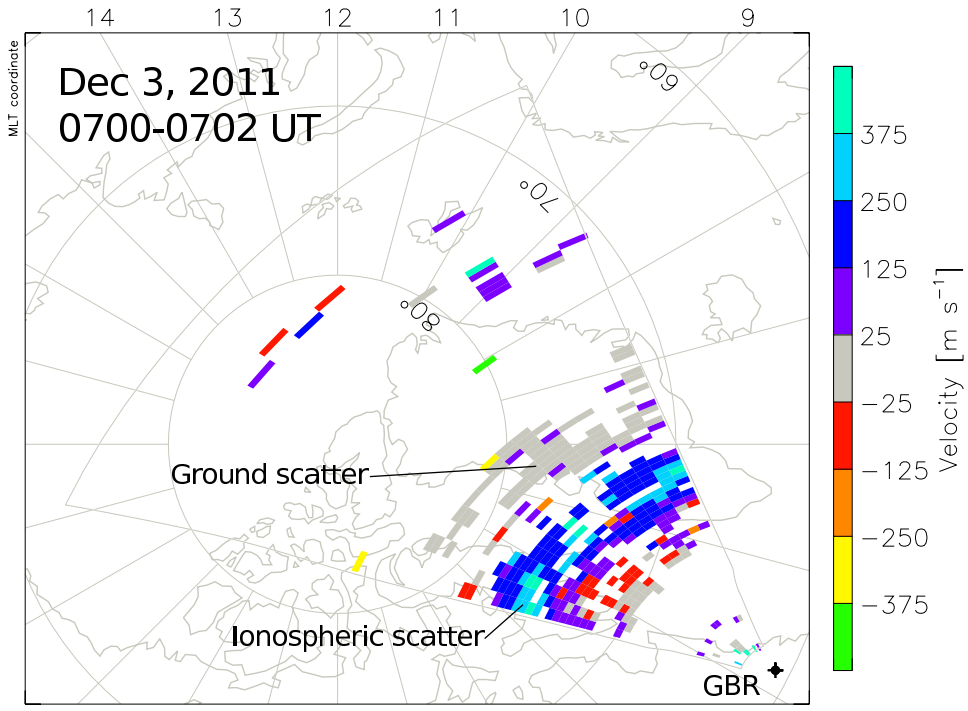

Figure 1.10: Line-of-sight Doppler velocity measurements obtained by the Goose Bay SuperDARN radar (GBR) during a full azimuth scan from 0700 - 0702 UT on Dec 3, 2011. Velocities are color coded according to the scale on the right and the gray portion of velocities indicates low velocity ground scatter.

1.8 SuperDARN convection patterns

All SuperDARN radars generate common data products, such that ionospheric measurements of line-of-sight Doppler velocities from all radars can be combined to produce global maps of ionospheric convection using the procedure described in *Ruohoniemi and Baker* [1998]. Example maps obtained in both the northern and southern hemispheres are shown in Figure 1.12. The left (right) panel in the figure shows estimated ionospheric convection pattern in the northern (southern) hemisphere. The convection patterns are derived using measurements corresponding to a full azimuth scan on March 30, 2002 beginning at 0700 UT. Also, overlayed on the figure are the fields-of-view of radars contributing to the measurements. The figure clearly shows interhemispheric differences in the convection pattern,

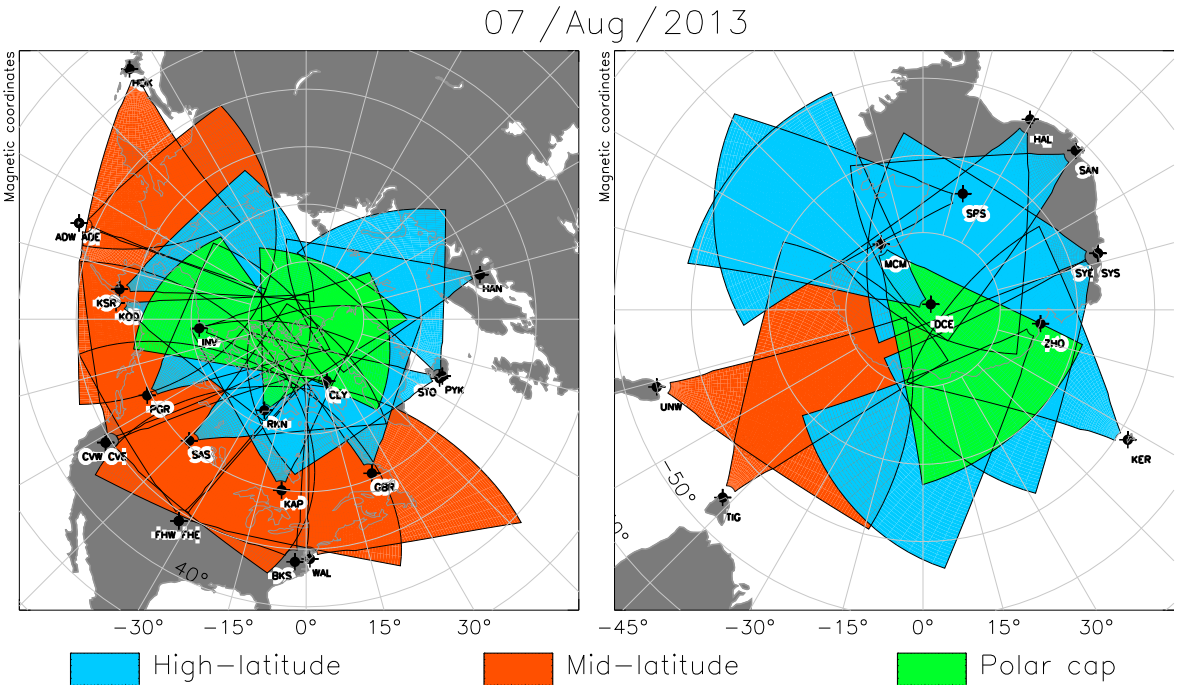

Figure 1.11: Fields-of-view of currently operational SuperDARN radars in the northern hemisphere (left) and the southern hemisphere (right).

especially near the noon sector (measurements coming from HAN radar in the north and KER/SYE radars in the south).

These SuperDARN convection maps are currently the only direct means to estimate ionospheric convection over large spatial scales and are, thus, important tools for understanding the dynamic impact of solar wind and magnetosphere interactions on the Earth's atmosphere/ionosphere. Moreover, such measurements can provide a useful overview of space weather activity and are thus widely used to add context to the analysis of other more spatially localized measurements. Furthermore, SuperDARN radars have accumulated a large dataset spanning more than a decade in both hemispheres, which provides an excellent opportunity to study interhemispheric magnetic conjugacy and large scale magnetosphere-ionosphere interactions. SuperDARN provides the primary dataset used in this study.

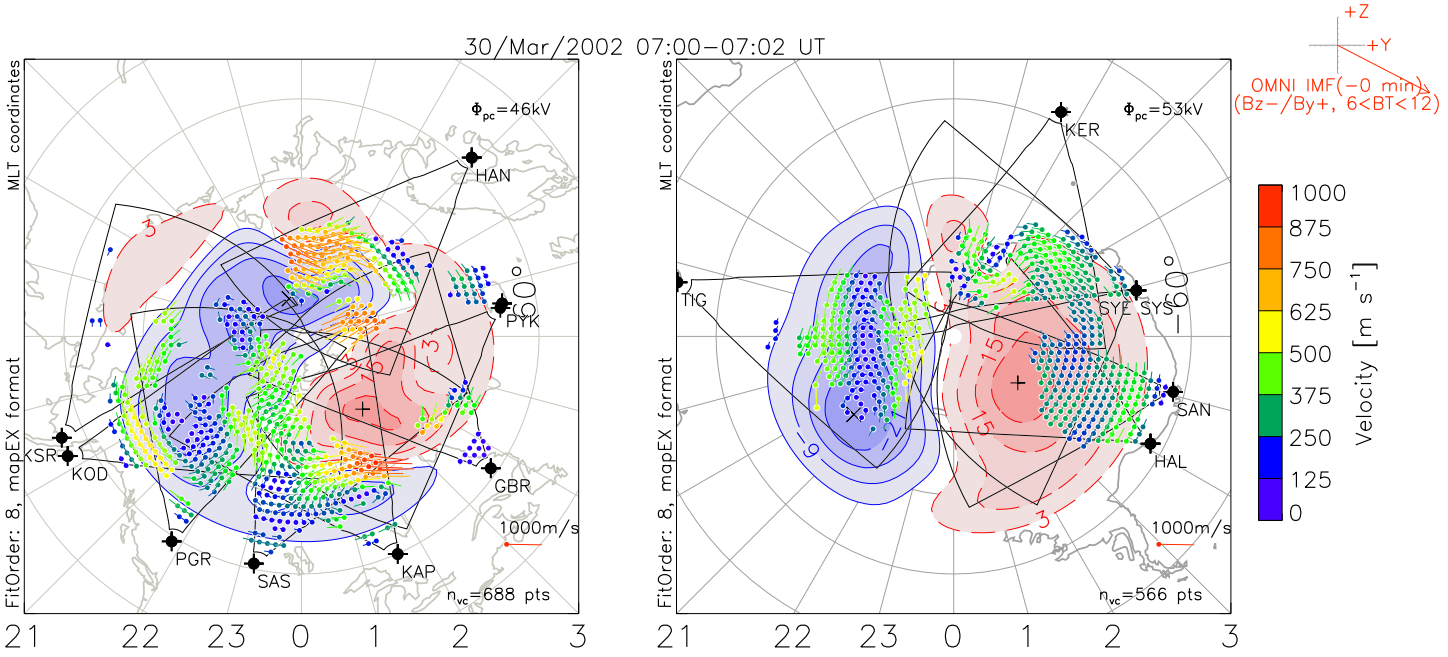

Figure 1.12: SuperDARN convection maps overlayed on Magnetic Latitude - Magnetic Local Time grid. The measurements correspond to a full azimuth scan on March-30-2002, beginning at 0700 UT. The left(right) panel presents measurements in the northern(southern) hemisphere. The dial on the top right corner shows the IMF conditions (taken from the OMNI dataset) during the event. Overlaid on each map are the fields-of-view of each radar contributing to the generation of the map.

1.9 Research Objectives and Dissertation Organization

As discussed in the previous section, SuperDARN has a large dataset comprising of measurements of ionospheric convection in both hemispheres. Furthermore, the recent expansion of SuperDARN into the mid-latitude region provides large scale measurements of plasma flows in this region. Currently, there are eight mid-latitude SuperDARN radars operating and together they have been making observations of plasma convection across the entire North American sector (the mid-latitude radars are marked in orange in Figure 1.11). The broad objective of this dissertation is to utilize this dataset to study the nature of magnetosphere-ionosphere coupling. In particular, the focus will be on investigating the role of interhemispheric magnetic conjugacy in the coupling between these regions and analyzing

the characteristics of this coupling over large spatial scales in the mid-latitude ionosphere.

The research results in this dissertation are divided into three chapters. In chapter 2, the extent of magnetic conjugacy exhibited in the mid-latitude ionosphere is analyzed using interhemispheric observations of a Sub-Auroral Polarization Stream (SAPS) channel [*Foster and Burke*, 2002]. Simultaneous interhemispheric observations of SAPS have historically been limited, owing to the lack of coverage in the southern hemisphere. However, the re-positioning of the Halley radar by British Antarctic Survey to the Falkland Islands for 18 months during the site rebuild created a unique opportunity for conjugate studies with the new mid-latitude radars in eastern North America. Simultaneous observations of a SAPS channel made by mid-latitude SuperDARN radars in both hemispheres (Wallops Island and Blackstone radars in the northern hemisphere and the Falkland Islands radar in the southern hemisphere) were analyzed. It was demonstrated that, even though the channel exhibited substantial interhemispheric differences in certain features such as electric fields and latitudinal widths, it was magnetically conjugate in terms in potential variations. In chapter 3, magnetically conjugate measurements of the dayside ionospheric convection on closed magnetic field lines (during four separate time intervals) were analyzed to investigate the presence of IMF B_Y associated interhemispheric asymmetries in the region. Earlier studies demonstrating the effects of IMF B_Y on closed field lines were limited to measurements from one hemisphere. To investigate the interhemispheric asymmetries associated with IMF B_Y, extensive and simultaneous observations of convection electric fields over conjugate regions are necessary. Such measurements are only available with SuperDARN. The interhemispheric asymmetries observed in this study support the existence of a IMF B_Y associated potential difference and a field-aligned current system between the hemispheres. The strength of the interhemispheric currents during all the four events was estimated and it was demonstrated that the currents exhibited a dependence on IMF B_Y, proximity to open-closed field line

boundary, MLT, and ionospheric conductivity. After a discussion on magnetic conjugacy in the mid-latitude and high-latitude region, large scale observations made by the new mid-latitude chain of SuperDARN radars are analyzed in chapter 4. Previous SAPS studies have been limited to latitudinal cuts by satellites and local observations by single radars. The new mid-latitude chain of SuperDARN radars under the NSF MSI (National Science Foundation Mid-Sized Infrastructure) program provided longitudinally expanded views of the SAPS, as demonstrated by *Clausen et al.* [2012a]. In this study, the important task of characterizing SAPS occurrence and characteristics in the SuperDARN observations as a step towards understanding and modeling their role in M-I coupling is performed. A statistical database of 159 SAPS events observed in the mid-latitude SuperDARN radars between Jan-2011 and Aug-2012 was compiled. The event database was then used to analyze the average spatial variations in the occurrence rate and velocities of the SAPS channel under different geomagnetic conditions. Moreover, an empirical model based on Dst-index is developed to estimate the occurrence rate of SAPS at a given latitude and local time. Finally, conclusions and ideas for future work are discussed in Chapter 5.

Chapter 2

An examination of inter-hemispheric conjugacy in a subauroral polarization stream

B. S. R. Kunduri,[1] J. B. H. Baker,[1] J. M. Ruohoniemi,[1] L. B. N. Clausen,[2] A. Grocott,[3] E. G. Thomas,[1] M. P. Freeman,[4] and E. R. Talaat[5]
Journal of Geophysical Research, Published 2012.

[1] Bradley Department of Electrical and Computer Engineering, Virginia Tech, Blacksburg, Virginia, USA
[2] Institute of Geophysics and Extraterrestrial Physics, Braunchweig, Germany
[3] Department of Physics and Astronomy, University of Leicester, Leicester, UK.
[4] British Antarctic Survey, Cambridge, UK.
[5]The Johns Hopkins University Applied Physics Laboratory, Laurel, Maryland, USA.

Abstract

During geomagnetically disturbed conditions the mid-latitude ionosphere is subject to intense poleward directed electric fields in the dusk-midnight sector. These electric fields lead to the generation of a latitudinally narrow westward directed flow channel in the subauroral region called a subauroral polarization stream (SAPS). If the magnetic field lines are treated as equipotentials, electrodynamic events such as SAPS are expected to occur simultaneously at magnetically conjugate locations with similar features. In this paper we present simultaneous observations of a SAPS event in both hemispheres made by mid-latitude SuperDARN radars with conjugate fields-of-view. We analyze the relation between the geomagnetic conditions and the characteristics of the channels such as latitudinal location, electric field, total potential variations across the channels, and Pedersen current. The results suggest a strong correlation between the strength of the ring current and the latitudinal location of the channel. An inter-hemispheric comparison of the characteristics of the channel indicates that the potential variations across the channels are similar while the electric fields, Pedersen currents and latitudinal widths of the channel exhibit differences that are consistent with

equal potential variations. We attribute these differences to seasonal differences in ionospheric conductivity between the hemispheres and magnetic distortion effects in the inner magnetosphere.

2.1 Introduction

Subauroral polarization streams (SAPS) are latitudinally narrow regions of intense westward flows observed in the mid-latitude ionosphere observed either just equatorward or at the edge of the auroral electron precipitation boundary [*Anderson et al.*, 1993, 2001; *Foster and Burke*, 2002; *Oksavik et al.*, 2006; *Makarevich and Dyson*, 2008; *Grocott et al.*, 2011]. SAPS are considered to be a result of poleward directed subauroral electric fields associated with processes occurring in the inner magnetosphere [*Foster*, 1995; *Foster and Rich*, 1998]. A number of terms have been employed in the literature to describe SAPS, which include polarization jets (PJ) [*Galperin et al.*, 1974], subauroral ion drifts (SAID) [*Spiro et al.*, 1979; *Anderson et al.*, 1993] , subauroral electric fields (SAEF) [*Karlsson et al.*, 1998] and substorm associated radar auroral surges (SARAS) [*Freeman et al.*, 1992]. The term subauroral polarization stream (SAPS) was introduced [*Foster and Burke*, 2002] as a broad description of strong westward flows (generally 200 m/s - 500 m/s) which are not as intense as those associated with SAID. SAID (also referred to as PJ in some literature) is more localized in latitude than SARAS and SAPS and is an intense enhancement embedded within a SAPS channel where the flows may reach 5 km/s in magnitude [*Foster and Burke*, 2002; *Anderson et al.*, 2001]. A similar phenomenon called auroral westward flow channel (AWFC) has been reported in the literature [*Makarevich and Dyson*, 2008; *Koustov et al.*, 2006; *Parkinson et al.*, 2003, 2007]. AWFC's are reported to exhibit characteristics similar to that of relatively weak SAID/PJ and are thought to be their poleward manifestations [*Parkinson et al.*, 2003]. SAPS are typically observed in the pre-midnight ionosphere between 18:00 and 02:00 MLT [*Spiro et al.*, 1979; *Anderson et al.*, 2001].

A mechanism was proposed by *Anderson et al.* [1993] to explain the formation of SAPS. During geomagnetically disturbed conditions the equatorward edge of the ion precipitation boundary moves earthward relative to the equatorward edge of the electron precipitation boundary [*Anderson et al.*, 2001; *Heinemann et al.*, 1989]. This leads to the generation of a radial electric field in the inner magnetosphere which maps into the ionosphere along magnetic field lines in the poleward direction. The resulting poleward directed electric field causes an increased westward $\mathbf{E} \times \mathbf{B}$ drift in the mid-latitude ionosphere which leads to increased collision frequencies and ion recombination resulting in a depletion in ionospheric plasma in the mid-latitude trough [*Anderson et al.*, 2001]. Assuming the main magnetospheric driver supplies the same field-aligned currents, a cumulative effect develops: the depletion of plasma through recombination leads to a decrease in the height integrated conductance and increased electric field and plasma flow velocity [*Anderson et al.*, 2001; *Parkinson et al.*, 2007].

Inter-hemispheric observations of SAPS events provide an opportunity to study conjugate aspects of the dynamics of the Earth's inner magnetosphere during disturbed geomagnetic conditions. SAPS observations at the two ionospheric ends of a closed magnetic field line can be expected to exhibit similarities because large-scale electric fields map with little attenuation along the highly conducting magnetic field lines, any potential difference that arises between the hemispheres should be neutralized by the flow of field-aligned currents [*Maeda*, 1974; *Stening*, 1977]. Previous studies related to inter-hemispheric conjugacy have been limited to the auroral zone [*Fillingim et al.*, 2005; *Sato and Saemundson*, 1987; *Frank and Sigwarth*, 2003; *Østgaard et al.*, 2004]. Very few studies have focused on the inter-hemispheric conjugacy exhibited during SAPS events. *Foster and Rideout* [2007] reported simultaneous observations of SAPS in magnetically conjugate locations while *Parkinson et al.* [2005] used observations from the TIGER and King Salmon (KSR) SuperDARN HF Radars

with magnetically conjugate fields-of-view to study the conjugacy exhibited by an AWFC.

Oksavik et al. [2006] presented the first observations of a SAPS channel in the Wallops Island (WAL) SuperDARN radar and demonstrated the ability of mid-latitude SuperDARN radars to make two-dimensional measurements of SAPS/SAID features with a high temporal resolution. An analysis of a SAPS channel observed by six midlatitude SuperDARN HF radars simultaneously over six hours of magnetic local time is presented in *Clausen et al.* [2012a]. In the current paper we present a detailed analysis of the conjugacy exhibited during a SAPS event that occured on Aug 4, 2010, using observations from mid-latitude SuperDARN radars. This same event was studied by *Grocott et al.* [2011]. The primary focus of *Grocott et al.* [2011] was the influence of magnetospheric dynamics and solar wind-magnetosphere coupling on the characteristics of a SAPS channel (observed by the Falkland Islands (FIR) SuperDARN radar in the Southern hemisphere) such as its location and velocity. In the current paper we focus on the inter-hemispheric aspects of the same event using Northern hemisphere observations from WAL and Blackstone (BKS) SuperDARN radars whose fields-of-view are magnetically conjugate to that of the FIR radar. We present an analysis of the inter-hemispheric differences and similarities observed in the features of the SAPS channels.

2.2 Datasets

2.2.1 SuperDARN HF Radars

The primary data used in this study were measurements of the Doppler velocities associated with ionospheric plasma drift observed by HF radars of the Super Dual Auroral Radar Network (SuperDARN) located at the mid-latitudes in the Northern hemisphere (WAL and BKS) and the Southern hemisphere (FIR). The SuperDARN network is an international chain of radars covering both high and mid-latitudes in both the Northern and Southern

hemispheres. Currently there are 19 radars in the Northern hemisphere and 10 radars operating in the Southern hemisphere with more radar builds underway or planned. SuperDARN radars observe coherent backscatter from decameter-scale irregularities aligned along the magnetic field. The Doppler shift of the backscattered signal is proportional to the line-of-sight component of the $\mathbf{E} \times \mathbf{B}$ plasma drift in the scattering region [*Ruohoniemi et al.*, 1987]. In the standard operating mode the radars use an array of electronically phased antennas that can be steered through 16 beam directions across an azimuth sector of 50°. The radar dwells for 3.5 or 7 seconds on each beam along which line-of-sight measurements of the velocity are obtained. The radar dwell time corresponds to the completion of a full azimuth scan in 1 or 2 minutes.

2.2.2 Other Datasets and Models

The mapping of SuperDARN Doppler measurements between hemispheres was achieved using the IGRF model for internal sources and Tsyganenko models-T96 [*Tsyganenko and Stern*, 1996], T01 [*Tsyganenko*, 2002a] and T04S [*Tsyganenko and Sitnov*, 2005] for external (magnetospheric) current sources. The external contributions to the magnetospheric magnetic field are specified by Tsyganenko models through mathematical formalism and empirical modeling. Certain geomagnetic indices such as the Dst index and interplanetary magnetic field measurements are required as inputs to the Tsyganenko models. The Dst index is indicative of the strength of the ring current and is taken from selected magnetometer stations near the equator [*Sugiura*, 1964]. For the purposes of analyzing the geomagnetic conditions, the Sym-H and Asym-H indices which are indicative of the strengths of the ring-current and the asymmetric ring current respectively [*Iyemori*, 1990] were used instead of the Dst index. The Sym-H and Asym-H indices are preferred because of their higher temporal resolution of 1-minute compared to the 1-hour resolution of the Dst index. These indices

were accessed through the Geomagnetic Data Service - Kyoto, Japan. The IMF and solar wind conditions such as the solar wind dynamic pressure and the IMF-B_Z were accessed from the OMNI 2 data set at the National Space Science Data Center (NSSDC) [*King and Papitashvili*, 2005].

The ion and electron energy flux data measured by the SSJ/4 instrument [*Hardy*, 1984] on-board the Defense Meteorological Satellite Program (DMSP) F18 spacecraft were used along with the Feldstein-Starkov statistical auroral oval models [*Feldsten and Starkov*, 1967] to predict the locations of the ion and electron auroral ovals. The SSJ/4 instrument provides 1-second resolution measurements of ion and electron energy fluxes between 30 eV and 30 KeV [*Hardy*, 1984]. The electron flux data were also employed to estimate the height integrated Pedersen conductivity as described by *Robinson et al.* [1987]. DMSP Special Sensor for Ions, Electron and Scintillation (SSIES) thermal plasma instrument package [*Rich and Hairston*, 1994] includes the Ion Drift Meter (IDM) which measures the thermal ion velocity in the horizontal and vertical directions relative to spacecraft velocity. The data from IDM are used during favorable conjuctions to verify the observations made in SuperDARN radars.

2.3 Observations

On August 4 2010 from 00:30 UT to 04:30 UT a region of high velocity backscatter was observed simultaneously by the WAL and BKS radars in the Northern hemisphere and the FIR radar in the Southern hemisphere. In this section we examine the nature of the backscatter observed by these radars and verify that this backscatter was indeed from SAPS channels. The FIR radar measurements from the same event period were studied independently by *Grocott et al.* [2011].

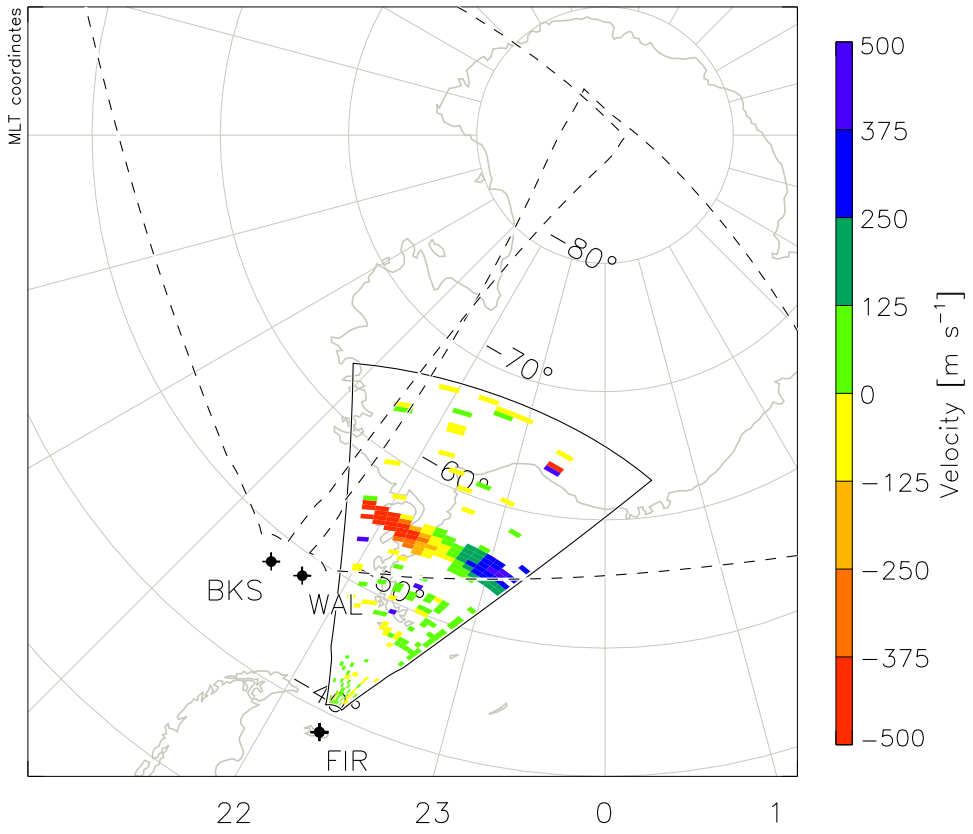

Figure 2.1: FIR radar observations of the line-of-sight Doppler velocities measured during the 1-minute azimuth scan beginning at 02:30 UT on August 4, 2010. The measurements are overlayed on a grid of magnetic latitude - magnetic local time. The velocity is scaled according to the color bar on the right.The solid outline represents the field-of-view of the FIR radar and the dashed outlines represent the fields-of-view of the BKS and WAL radars projected into the Southern hemisphere.

Figure 2.1 shows measurements of line-of-sight Doppler velocity made by the FIR radar plotted in magnetic latitude (MLAT) vs magnetic local time (MLT) coordinates for the scan beginning at 02:30 UT. The velocity is scaled according to the color bar on the right of the figure. The field-of-view of the FIR radar is identified in solid black lines. The dashed black lines mark the fields-of-view of the WAL and BKS radars projected from the Northern hemisphere into the Southern hemisphere. It can be observed that a significant portion of the field-of-view of the WAL radar in the Northern hemisphere is magnetically conjugate to the field-of-view of the FIR radar in the Southern hemisphere, while the field-of-view of the BKS

radar extends the coverage to the west of the conjugate region. In a similar manner Figure 2.2 presents measurements of the line-of-sight Doppler velocities measured by the BKS and WAL radars in the Northern hemisphere at the same time. The dashed black lines mark the field-of-view of the FIR radar projected from the Southern to the Northern hemisphere. The backscatter observed in the BKS and WAL radars appears different because of the different operating frequencies of the radars during the event (BKS $\sim$ 9 MHZ and WAL - varied between 9 and 16 MHz).

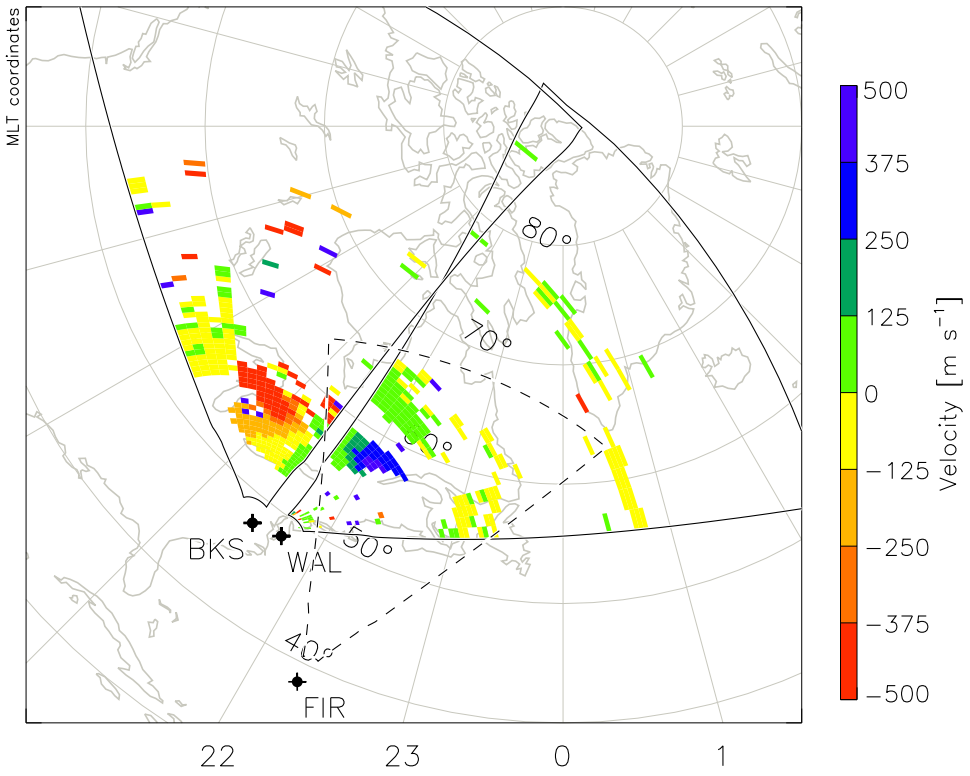

Figure 2.2: WAL and BKS radar observations of the line-of-sight Doppler velocities measured during the azimuth scan at 02:30 UT on August 4, 2010. The measurements are overlayed on a grid of magnetic latitude - magnetic local time. The velocity is scaled according to the color bar on the right.The solid outlines indicate the fields-of-view of the WAL and BKS radars and the dashed outline represents the field-of-view of the FIR radar projected into the Northern hemisphere.

In Figure 2.1 a latitudinally narrow region of backscatter, about 2° in latitudinal width with line-of-sight velocity (V_{LOS}), varying in magnitude from 150 m/s to 500 m/s was ob-

served by the FIR radar centered on -57° magnetic latitude and extending almost across the entire field-of-view. The red colored portion of the backscatter in the figure corresponds to negative V_{LOS} and indicates flow away from the radar. The blue colored backscatter corresponds to positive V_{LOS} and indicates flow towards the radar. A systematic variation in the direction of V_{LOS} across the field-of-view of the FIR radar can be seen. The measured V_{LOS} is directed towards the radar in the eastward-oriented beams (beams 11-16), then gradually passes through zero across the poleward-oriented central beams (beams 8-10) and in the westward-oriented beams (beams 1-7) the direction of V_{LOS} is away from the radar. This indicates that the actual direction of the flow in the ionosphere is predominantly westwards and resembles a SAID channel.

Simultaneously in the Northern hemisphere, the BKS and WAL radars made observations of a similar narrow region of high-velocity backscatter. The feature extended from 55° to 60° in magnetic latitude and was predominantly observed in beams 5-13 of the BKS radar and beams 2-5 of the WAL radar (beams are numbered from west to east). The observations in the Northern hemisphere indicate the presence of a high-velocity narrow channel embedded within a broader channel (about 5° to 6° in latitudinal width) of comparatively lower velocity, similar to the characteristics of SAID and SAPS [*Oksavik et al.*, 2006]. It should be noted that in the Southern hemisphere observations were dominated by a narrow SAID-like feature, without a surrounding SAPS. The V_{LOS} observed in the BKS and WAL radars exhibit an orderly east to west variation similar to the observations in the Southern hemisphere. This indicates the flows in the Northern hemisphere are also predominantly westward.

Other characteristics of this region will be explored further to demonstrate that this backscatter is indeed from a SAPS/SAID channel in both the hemispheres.

2.3.1 Location of the SAPS scatter region

Previous studies [*Anderson et al.*, 1993; *Foster and Vo*, 2002] have identified SAPS as lying either just equatorwards or at the edge of the equatorward boundary of the electron auroral oval. The purpose of this section is to characterize the location of the scatter region and demonstrate that the scatter is subauroral.

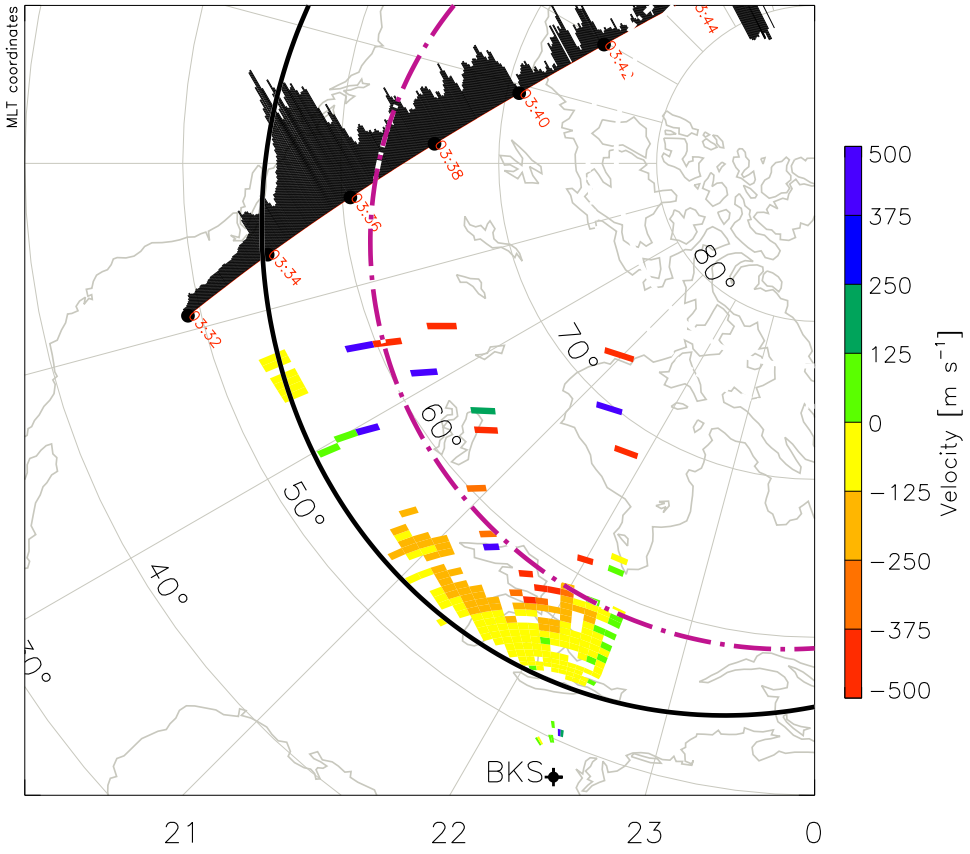

Figure 2.3: Line-of-sight velocity plot for a full scan of BKS radar at 03:32 UT on August 4, 2010, displayed versus magnetic latitude and magnetic local time. The velocity of the scatter is scaled according to the color bar on the right. Overlayed on the map is the DMSP F18 SSIES ion drift meter data at the mentioned instance of time (in UT). The solid black and the dashed purple curves mark the equatorward and poleward boundaries of the backscatter respectively. Further details are discussed in the text.

Figure 2.3 presents V_{LOS} observed during an azimuth scan in the BKS radar beginning at 03:32 UT on August 4, 2010. It is overlayed on a map marked in MLT vs magnetic

latitude. A DMSP F18 satellite pass in the northern hemisphere around the time of the scan is also shown in the figure. The black dots represent the location of the spacecraft at the marked instance of time (in UT). Data from the ion drift meter instrument onboard the satellite is also overlayed on the map.

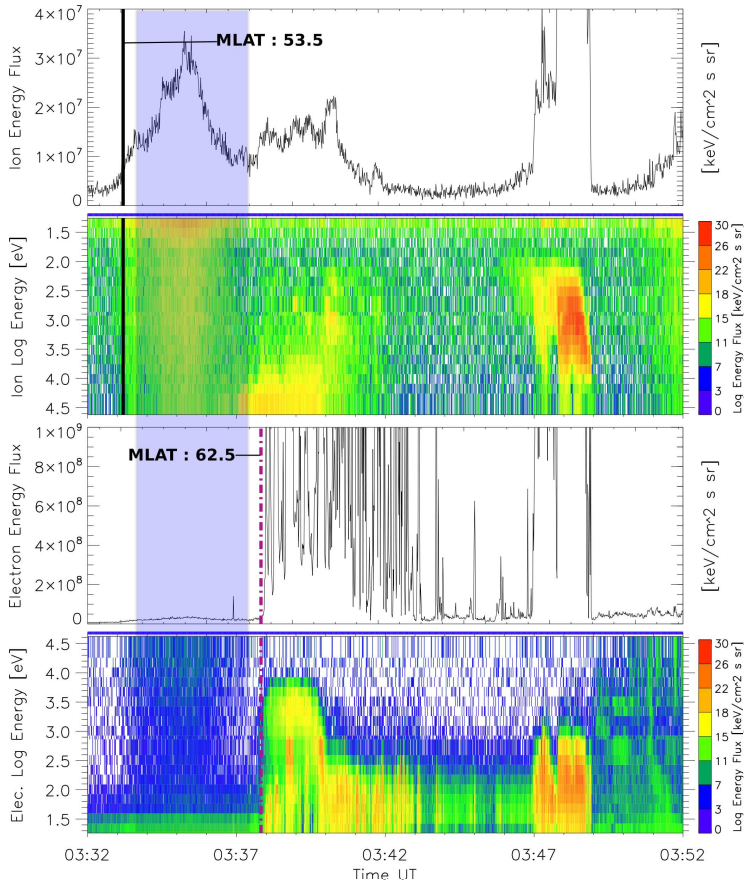

Figure 2.4: Time series data from SSJ/4 instrument onboard DMSP F18 satellite corresponding to the pass presented in Figure 2.3, representing (from top to bottom) : Total ion energy flux across the entire energy spectrum, Ion energy spectrogram, scaled according to the color bar on the right, total electron energy flux across the entire energy spectrum, and electron energy spectrogram in a format similar to the first two panels. The solid black lines and the dotted purple lines overlayed on the panels indicate the time at which the satellite crosses the equatorward boundaries of the ion and electron precipitation respectively. The shaded region in all the panels represents the location of the backscatter region observed in the radar.

We use data from the SSJ/4 instrument [*Hardy*, 1984] on board the DMSP F18 space-

craft to identify the equatorward electron and ion auroral oval boundaries and compare them with the location of the radar backscatter region under study. The first and second panels of Figure 2.4 present the time variations in SSJ/4 total ion energy flux data across the entire energy spectrum and the ion energy spectrograms respectively. The third and fourth panels represent the same for electron energy flux. The solid black line overlayed on the first and second panels of Figure 2.4 and the dotted purple line overlayed on the third and fourth panels mark the times at which the spacecraft crosses the equatorward boundaries of the ion and electron precipitation respectively. The boundaries were identified in a manner similar to the criteria described in *Gussenhoven et al.* [1981] for identifying the equatorward electron auroral boundary, such as a sharp increase in the total number flux (J_{Ntot}) and energy flux (J_{Etot}) of electrons and J_{Ntot} reaching values greater than 10^7 (cm^2 sr s)$^{-1}$ on encountering the boundary. The magnetic latitudes of the equatorward boundaries of ion and electron auroral ovals are indicated in Figure 2.4. The shaded region in the figure represents the location of the backscatter region observed by the BKS radar and clearly lies between the precipitation boundaries.

The backscatter region in Figure 2.3 shows V_{LOS} varying between -200 and -500 m/s between 20:00 and 22:00 MLT. This region was about 6°-7° in latitudinal width and extended between 53° and 59° magnetic latitude. The solid black and the dotted purple curves in Figure 2.3 mark the equatorward and poleward edges of the high velocity backscatter region. These curves are marked by adjusting the Feldstein statistical auroral oval models [*Feldsten and Starkov*, 1967]. This region of backscatter is indicated in Figure 2.4 as the shaded region. From Figures 2.3 and 2.4 it can be observed that the radar backscatter is confined to the area that lies between the ion and electron precipitation boundaries. The association of the SAPS like feature in the radar observations with the particle precipitation boundaries is similar to the results presented in previous studies [*Anderson et al.*, 1993, 2001; *Foster and*

Vo, 2002].

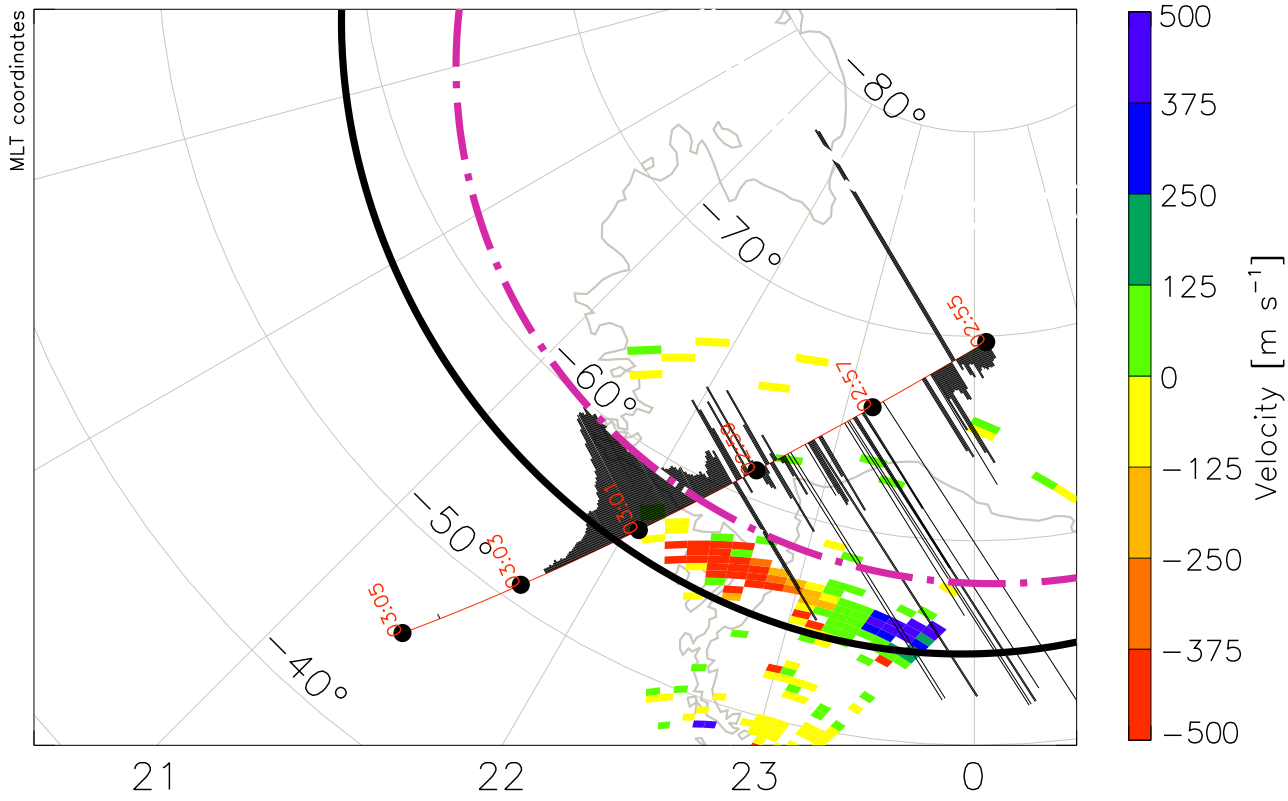

Figure 2.5: Line-of-sight velocity plot for a full scan of FIR radar and a DMSP F18 SSIES ion drift meter overlay at 03:00 UT on August 4, 2010 (in the same format as Figure 2.3).

A similar analysis is done in the Southern hemisphere and the results are presented in Figures 2.5 and 2.6. The V_{LOS} data for an azimuth scan beginning at 03:00 UT in the FIR radar are shown in Figure 2.5. The radar backscatter region was only about 3° in latitudinal width and extended between 55° and 58° magnetic latitude. Figure 2.6 presents the DMSP F18 ion and electron energy flux measurements in the Southern hemisphere near the field-of-view of the FIR radar in the same format as Figure 2.4. The equatorward ion and electron precipitation boundaries were identified in a manner similar to the Northern hemisphere. The shaded region in the figure indicates the location of the backscatter region observed by the FIR radar. The location of this region with respect to the particle precipitation boundaries suggests that the SAPS-like feature was observed equtorward of the electron

auroral oval and poleward of the ion oval.

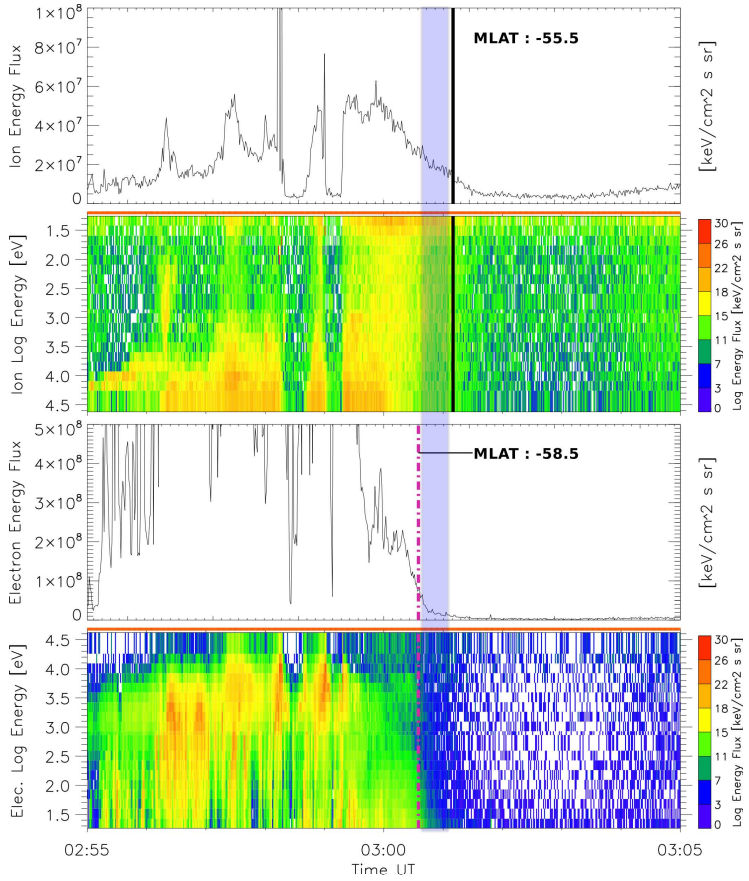

Figure 2.6: Time series data from SSJ/4 instrument onboard DMSP F18 satellite corresponding to the pass shown in Figure 2.5 (in the same format as Figure 2.4).

The data from DMSP ion drift meter (shown in Figures 2.3 and 2.5) also shows the presence of narrow channels of high velocity, latitudinally collocated with the radar observations of similar flow channels in both hemispheres. The DMSP ion drift meter data thus validates the observations made in the BKS and FIR radars. It can be noted from Figure 2.3 that the high-velocity channel observed in the DMSP ion drift meter data is slightly broader than the channel observed in the BKS radar. This can be associated with the tendency of the flow channel to broaden with decreasing MLT from midnight to dusk [*Anderson et al.*, 1991; *Erickson et al.*, 2011]. Major differences were observed between the hemispheres in respect of

the location of the equatorward edges of the ion and electron precipitation boundaries. The equatorward edges of the ion and electron precipitation boundaries near the scatter region were observed to be located near 53° MLAT and 60° MLAT respectively, in the Northern hemisphere. The equatorward edges of the electron and ion precipitation boundaries were located near -58° and -55° MLAT respectively, in the southern hemisphere. This indicates inter-hemispheric differences and will be discussed further in later sections. Although the observations in opposite hemispheres were made at different times (a 30 minute difference), the stability of the SAPS/SAID features (the latitudinal location and width of the channels do not vary significantly as can be seen in the range-time plots shown in Figure 2.10, presented later) through this time period and their obvious association with the precipitation boundaries indicates sufficient permanance to discuss conjugacy. Moreover the location of the equatorward edges of the precipitation boundaries was examined in both hemispheres using other DMSP passes as well (such as the DMSP F18 pass at 01:50 UT in the Northern hemisphere and at 01:15 UT in the Southern hemisphere). It was observed that the seperation between the boundaries was consistently wider in the Northern hemisphere compared to the Southern hemisphere.

In summary, the electron energy flux data shown in Figures 2.4 and 2.6 indicates that the latitudinally narrow regions of high westward velocity backscatter shown in Figures 2.3 and 2.5 are subauroral, satisfying the first requirement for the east-west elongated channels of radar backscatter to be associated with SAPS.

2.3.2 Direction and magnitude of flows in the channel

In this section we present an analysis of the flow velocity within the SAPS channels in both hemispheres.

Figure 2.7 presents the V_{LOS} measured in each beam plotted as a function of the beam

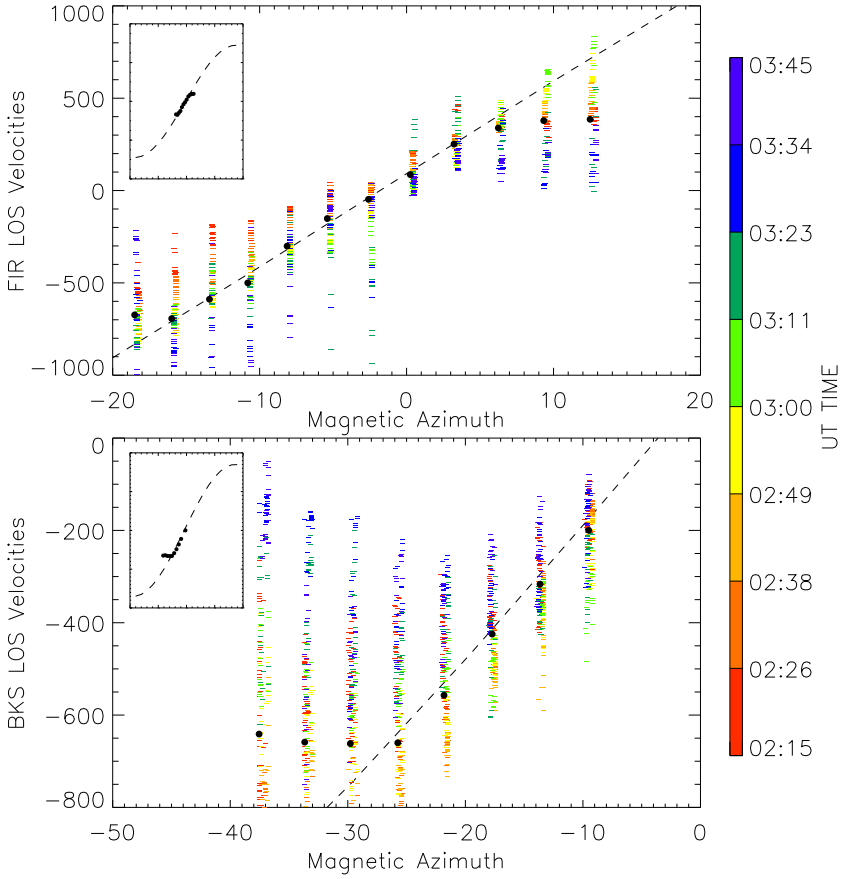

Figure 2.7: Variations in the line-of-sight velocities with time plotted against magnetic azimuth for the FIR (top) and BKS radars (bottom). The small colored dots are color coded according to the time scale indicated on the right. The thicker black dots indicate the median values of V_{LOS} at every magnetic azimuth. The dotted lines represent a sine curve fit to the median V_{LOS}. The same sine curves for the range -90° to 90° are shown in the insets.

azimuth and time for both the FIR (top panel) and BKS (bottom panel) radars. The magnetic azimuth of the beams varied from -20° to 16° for the FIR radar and from -40° to -9.5° for the BKS radar. In the figure each colored dot corresponds to a V_{LOS} measured at that magnetic azimuth. The color of the dots indicates the time of measurement, scaled according the color bar on the right with red (blue) indicating earlier (later) occurrence. From the figure it can be observed that the V_{LOS} in the FIR radar were negative in the westward direction (magnetic azimuth < 0), positive in the eastward direction (magnetic azimuth > 0) and that V_{LOS} passed through zero near the poleward direction. A similar

dependence of V_{LOS} on the magnetic azimuth of the beam was observed in the BKS radar, but the observations were limited to westward direction due to the orientation of the beams. This dependence of V_{LOS} on magnetic azimuth also conforms to the predominantly westward nature of flow across the field-of-view of the radars and indicates an approximately sinusoidal dependence of V_{LOS} on magnetic azimuth. These observations are consistent with the results presented in *Grocott et al.* [2011].

To demonstrate the sinusoidal variation exhibited by the V_{LOS} with magnetic azimuth, the median values of V_{LOS} (represented by the thick black dots) were calculated over the time interval 02:15 UT to 03:45 UT (interval with good conjugate observations) at every magnetic azimuth. Sine curves (indicated by the dotted lines in Figure 2.7) were then fit to these median V_{LOS}. The insets in both the panels present the same curves along with the median V_{LOS} (black dots) for an extended magnetic azimuth range of -90° to 90°. From the figure it can be observed that the median V_{LOS} exhibit a good adherence to the sine curves, except for some deviation at higher magnetic azimuths (which correspond to beams at the edges of the field-of-view). This could be due to the lack of data at certain range gates in these beams as seen in the azimuth scan plots presented in Figures 2.1 and 2.2. Another possibility is that over the larger longitudinal scales there is significant curvature in the convection such that the flow cannot be considered strictly uniform [*Freeman et al.*, 1991].

From a sine curve fitting of median V_{LOS}, the bearing (from median V_{LOS}) of the flows was determined to be $\sim$ -92° for the Southern hemisphere. Figure 2.8 shows the direction and magnitude of the SAPS flows (at the location in the flow channel where V_{LOS} was highest) estimated by projecting the V_{LOS} along the median direction of flow in each beam of the FIR radar. These correspond to an azimuth scan beginning at 02:46 UT. The velocities across the beams were found to vary between 2.7 km/s and 3 km/s. This variability could

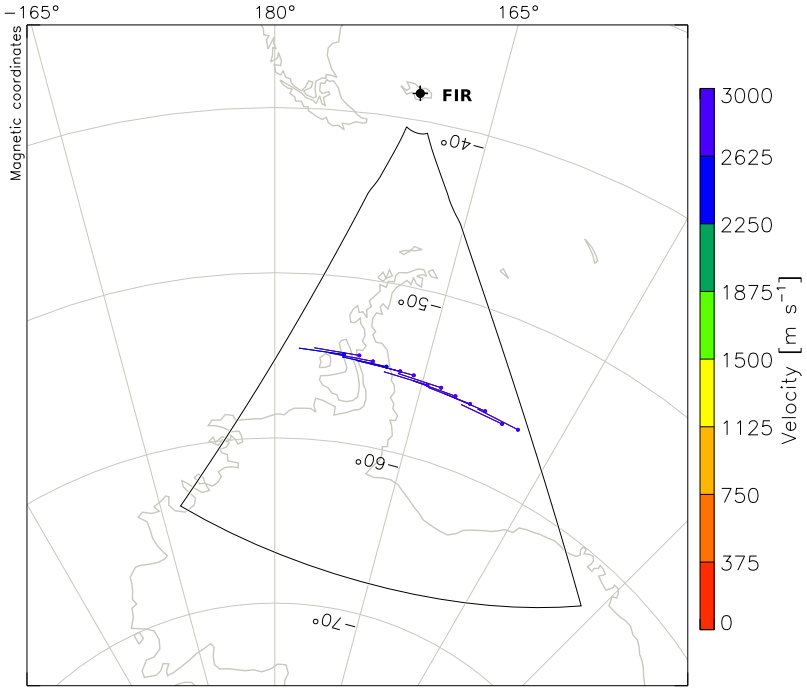

Figure 2.8: Direction and magnitude of the SAPS flows in each beam of the FIR radar, determined as described in the text. These correspond to the azimuth scan beginning at 02:46 UT on August 4, 2010 and are overlayed on a map marked in magnetic coordinates. The velocity is scaled according to the color bar on the right.

be due to the MLT difference (about 1 hour) across the field-of-view of FIR radar [*Foster and Vo*, 2002] or any variations in ionospheric conductivity. Since the variability is small compared to the magnitude, a median value of the velocity magnitude across the beams was calculated which came out to be $\sim$ 2.8 km/s. The median velocity across the beams would provide a means to make inter-hemispheric comparisons. A similar analysis in the Northern hemisphere showed that the bearing of the flows was $\sim$ -94° and the median value of velocity magnitude was about 1.7 km/s. The sine curve fitting showed that the flow direction in both the hemispheres was practically westwards and that the velocities reached magnitudes greater than 2 km/s.

The large scale fitting to obtain an overall SAPS velocity will lead to missing finer variations in the flow. However, the main goal of this paper is to provide an overview of

inter-hemispheric differences in the SAPS channels and this will not considerably affect our results. The SAPS velocity magnitude calculated this way will be referred to as 'estimated zonal' velocity from now on. From this analysis it is clear that the SAPS velocity is very nearly zonal with a considerable difference in magnitude between the hemispheres. A detailed inter-hemispheric comparison of the estimated zonal velocities is presented in the next section alongside other characteristics of the SAPS channel.

2.3.3 Geomagnetic conditions and their influence on the channel

A SAPS event is generally associated with disturbed geomagnetic conditions [*Foster and Burke*, 2002; *Anderson et al.*, 2001, 1993]. It is therefore important to analyze the solar wind and magnetospheric conditions prevalent during this event to investigate their effects on the flows.

Measurements of the latitudinally narrow region of high velocity backscatter were made during the course of a moderate geomagnetic storm that occurred between 3-5 August 2010. On August 3 2010 at around 19:00 UT the Dst index showed a sudden increase to 22 nT indicating storm sudden commencement and marking the beginning of the storm. Figure 2.9 presents the observations of the solar wind and IMF conditions from 00:00 UT to 06:00 UT on August 4 2010 during the time of the observations. During this event the IMF-B_Z varied between -12 nT and 12 nT and exhibited gradual south-north transition with short northward excursions. The B_Y component of the IMF stayed predominantly negative with a gradual strengthening in magnitude with short excursions to positive values, reaching a peak value of -15 nT. The IMF-B_X varied between -10 and 8 nT. The solar wind speed was relatively stable at around 600 km/s and the solar wind dynamic pressure varied between 6-10 nPa.

The top three panels of Figure 2.10 present the geomagnetic conditions. The first panel

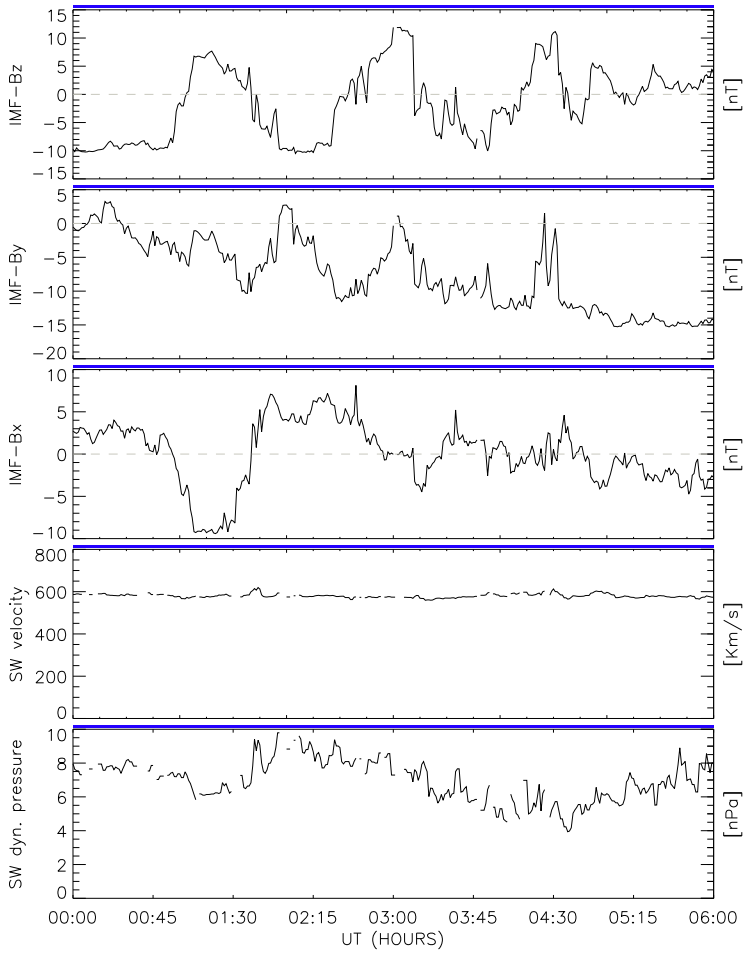

Figure 2.9: Time variations of solar wind and IMF data on August 4, 2010 from 00:00 UT to 06:00 UT, representing (from top to bottom) : 'Z', 'Y' and 'X' components of interplanetary magnetic field, solar wind velocity, and solar wind dynamic pressure, taken from the OMNI 2 dataset.

presents the Kp index which varied between 4-6 during the interval. The second and third panels present the Sym-H and the Asym-H index. These are indicative of the strength of the symmetric ring current and the partial ring current respectively [*Iyemori*, 1990]. It can be observed that the Sym-H index reached a peak value of about -80 nT around 01:30 UT and varied between -50 and -70 nT from then on. The Asym-H index reached a peak value of 120 nT and its variations were roughly correlated with Sym-H index for a major period during the interval. The Asym-H and Sym-H indices showed a large degree of variability

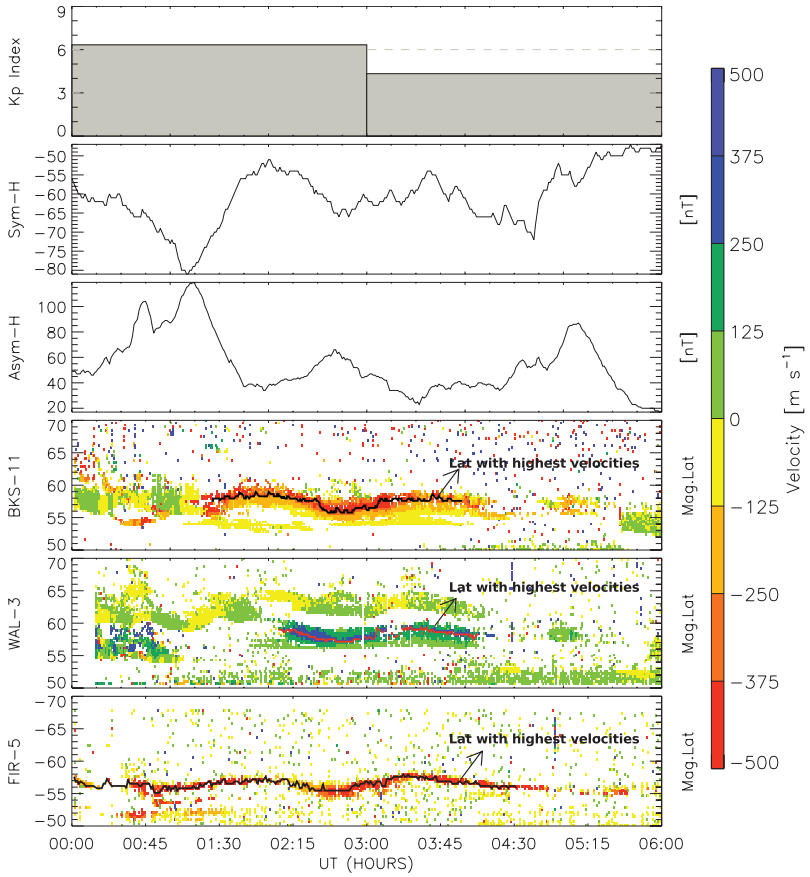

Figure 2.10: Time variations of data on August 4, 2010 from 00:00 UT to 06:00 UT, representing (from top to bottom) : Kp Index, Sym-H index, Asym-H index, radar V_{LOS} observed by BKS (beam-11, magnetic azimuth:-18.5°), WAL (beam-3, magnetic azimuth:8.3°) and FIR (beam-5, magnetic azimuth:-6.3°) radars versus magnetic latitude. The black line in the BKS beam-11 (V_{LOS}) plot, the red line in the WAL beam-3 plot and the black line in the FIR beam-5 plot indicate the latitudes where the V_{LOS} were highest.

suggesting alternating periods of intensification and weakening of the ring current.

The AE index reached a peak value of 1200 nT at $\sim$ 0100 UT and varied between 250 nT and 800 nT during the rest of the interval. An examination of the auroral indices (AE, AL, AU and AO) and ground based magnetometer data from the THEMIS magnetometer chain (data not presented here) suggest that the observations in this study occurred during an interval of sporadic substorm activity. The presence of substorms during the interval and the location of the SAPS/SAID channel between the equatorward edges of the ion and electron

precipitation boundaries, support the concept that the earthward boundaries of ion and electron precipitation separate following substorm onset, thereby leading to the generation of SAPS [*Anderson et al.*, 1993, 2001]. A detailed analysis of the influence of substorm activity on the SAPS channel during this event is presented in *Grocott et al.* [2011].

The fourth, fifth and sixth panels of Figure 2.10 present the V_{LOS} observed in beam 11 of the BKS radar, beam 3 of the WAL radar and beam 5 of the FIR radar respectively, plotted versus magnetic latitude and time. These plots present the temporal variability in latitudinal position, width and velocities exhibited by the channel in both hemispheres. The SAPS/SAID channel can be observed predominantly between 01:00 UT and 04:30 UT in all three radars. The observations clearly indicate that the width and the latitudinal location of the channel varied with time and in general the channel was consistently narrower in the Southern hemisphere. The solid lines inside the SAPS channel (black - BKS beam 11, red-WAL beam 3 and black - FIR beam 5) mark the latitudes at which the observed V_{LOS} were maximum. These latitudes will be referred to as Lat_{MAX} from here on. A preliminary look at Lat_{MAX} in each radar and the Asym-H index shows that Lat_{MAX} moves equatorward as Asym-H increases and poleward when Asym-H decreases.

A correlation analysis was performed to understand the influence of geo-magnetic conditions such as the Asym-H index (partial ring current) on latitudinal and estimated zonal velocity variations in the SAPS channel in both hemispheres. The top-left and the top-right panels of Figure 2.11 present scatter plots of the variations in Lat_{MAX} and estimated zonal velocities within the SAPS channel observed in the BKS radar as a function of Asym-H index. The correlation coefficients were found to be 0.65 and 0.57 respectively. The bottom-left and the bottom-right panels present scatter plots of Lat_{MAX} and estimated zonal velocity variations observed in the FIR and BKS radars. The correlation coefficients were calculated to be -0.83 and 0.66 respectively. The correlation coefficients presented in this study were

verified to be statistically significant using the student's t-test (with probability of unlikely occurrence, P << 0.01).

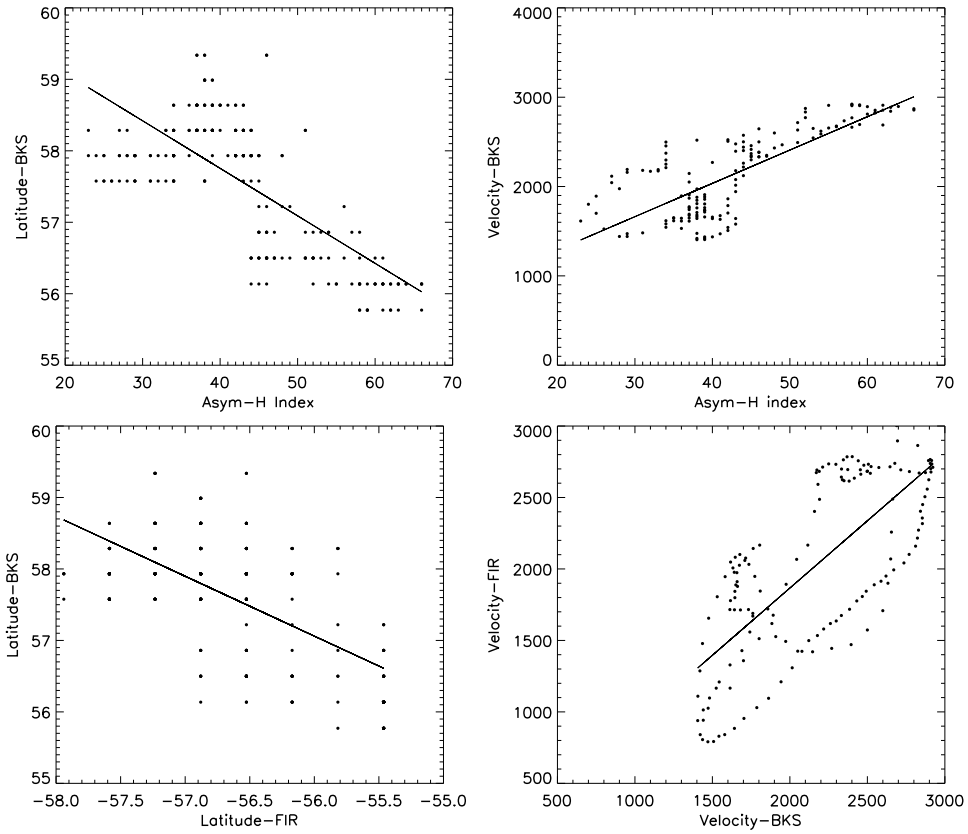

Figure 2.11: Scatter plots of (Clockwise from top-left) : BKS Lat_{MAX} vs Asym-H index, BKS estimated zonal velocity vs Asym-H index, FIR estimated zonal velocity vs BKS estimated zonal velocity, FIR Lat_{MAX} vs BKS Lat_{MAX}.

Results presented in Figure 2.11 suggest that there exists a good correlation between latitudinal variations in the channel and the strength of the asymmetric ring current. However the estimated zonal velocities exhibit a comparatively weaker correlation between the hemispheres and with the asymmetric ring current. The results of the correlation analysis are summarized in Table 2.1.

Table 2.1: Results of correlation analysis. FIR_{lat}, BKS_{lat} and WAL_{lat} refer to the latitudes at which V_{LOS} were highest(explained in section 3.3, Figure 2.10). BKS_{vel} and FIR_{vel} refer to the estimated zonal velocities in the channel where V_{LOS} were highest (explained in section 3.2, Figure 2.12). BKS_{POT} and FIR_{POT} refer to the cross-SAPS potentials estimated in BKS and FIR radars (explained in section 4, Figure 2.12)

Parameter-1	Parameter-2	Corr. coeff.
FIR_{lat}	IMF-B_Z	-0.53
BKS_{lat}	IMF-B_Z	0.56
FIR_{lat}	Asym-H	-0.58
BKS_{lat}	Asym-H	0.65
WAL_{lat}	Asym-H	0.69
FIR_{vel}	Asym-H	0.54
BKS_{vel}	Asym-H	0.57
WAL_{lat}	FIR_{lat}	-0.79
BKS_{lat}	FIR_{lat}	-0.73
BKS_{vel}	FIR_{vel}	0.62
BKS_{POT}	FIR_{POT}	0.81

2.4 Discussion

In the previous section observations of a SAPS channel made simultaneously by the BKS and WAL radars in the Northern hemisphere and the FIR radar in the Southern hemisphere were reported. A correlation analysis (Table 2.1) revealed that the solar wind and geomagnetic conditions had considerable influence on the channel morphology in both hemispheres. In this section we discuss these observations in more detail and compare them with results from previous studies.

As mentioned in the previous section Lat_{MAX} in each radar exhibits a dependence on Asym-H index. The results from correlation analysis also show that Lat_{MAX} variations in the SAPS channel in both the hemispheres exhibit a good correlation between the hemispheres and with the Asym-H index. Moreover if the Lat_{MAX} variations are passed through a moving-average filter they exhibit a significant improvement in the correlation coefficient. These results are in agreement with previous studies [*Grocott et al.*, 2011; *Erickson et al.*,

2011; *Huang and Foster*, 2007] and can be attributed to the dependence of the latitudinal position of the SAPS channel on the location of the ring current (the strength of the ring current is indicative of its location, the stronger the ring current the more closer it is to the Earth). Lat_{MAX} in each radar also shows a good correlation with IMF-B_Z which can be attributed to the dependence of the ring current on IMF-B_Z. As shown in Figure 2.9, B_Z during the interval of observations exhibits frequent northward and southward turnings. A southward directed IMF results in the intensification and earthward movement of the ring current thereby causing the SAPS channel in the ionosphere to move equatorwards; when the IMF is northward directed, the SAPS channel moves poleward due to the weakening of the ring current. Similar dependence of the latitudinal position of SAPS on IMF-Bz has been reported in a statistical study by *Erickson et al.* [2011].

We now calculate and estimate some other features of the channel. Figure 2.12 presents the variations in estimated zonal velocities in the SAPS channel (where the V_{LOS} were highest), Pedersen current densities, latitudinal widths of the channel and the cross-SAPS potentials in both hemispheres vs time. The Pedersen current densities (second panel) are determined using the relation $\mathbf{J_P} = \Sigma_P \mathbf{E}$. Here $\mathbf{J_P}$ is the Pedersen current density, $\mathbf{E}$ is the electric field across the channel and Σ_P is the height integrated Pedersen conductivity. The electric field across the channel is calculated assuming $\mathbf{E} \times \mathbf{B}$ drift. The magnitude of the Earth's magnetic field near the SAPS scatter region in the Northern hemisphere was estimated to be 56000 nT and 48200 nT in the Southern hemisphere using the IGRF-11 [*Finlay et al.*, 2010] coefficients. The relatively large difference between the field strengths in the Northern and Southern hemispheres is because of the proximity of the FIR radar to the south atlantic anomaly (SAA). The value of height integrated Pedersen conductivity due to electron precipitation was calculated using the empirical formula from *Robinson et al.* [1987], given below.

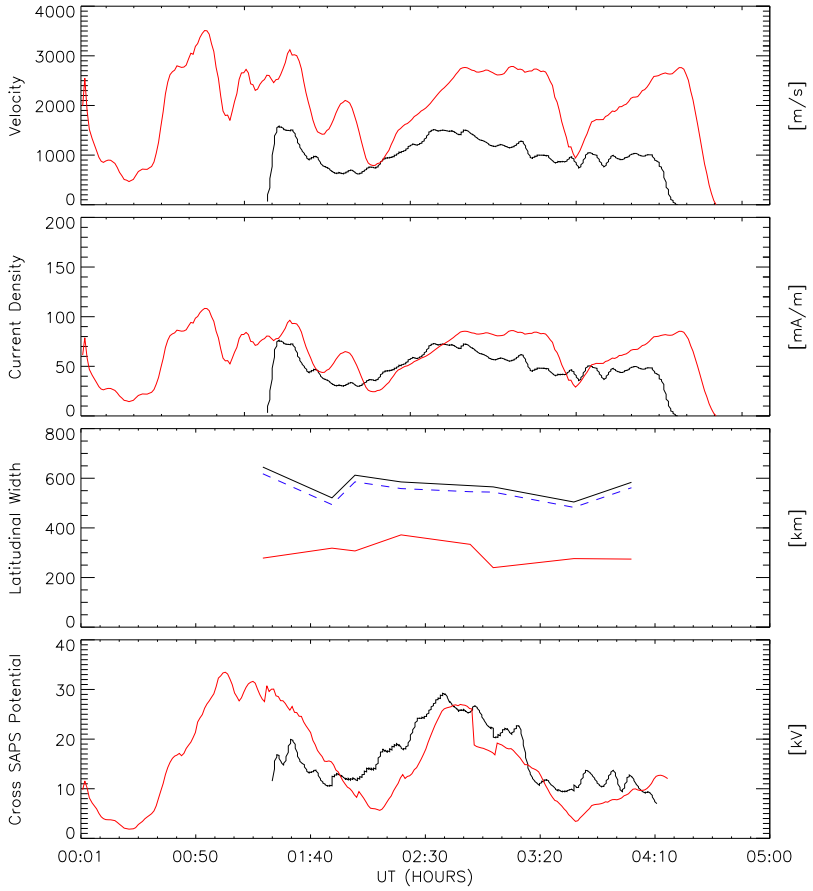

Figure 2.12: Time series data representing (from top to bottom): Magnitudes of the estimated zonal velocities, current densities in the SAPS channel, latitudinal width of the SAPS channel and the Potentials across the SAPS channel, observed by the BKS radar (solid black line) and the FIR radar (solid red line). The dotted blue line in the third panel represents the projection of the latitudinal width of the channel in the Northern hemisphere along the magnetic field lines into the Southern hemisphere using the Tsyganenko T01 model.

$$\Sigma_P = \frac{40 E_{avg} \phi_E^{1/2}}{16 + E_{avg}^2} \tag{2.1}$$

Here E_{avg} is the average energy of the precipitating electrons in KeV and ϕ_E is the electron energy flux in $ergs/cm^2s$. The values of E_{avg} and ϕ_E can be computed from the electron flux data of the SSJ/4 instrument [*Hardy*, 1984] aboard the DMSP F18 spacecraft. The height integrated Pedersen conductivity was found to be 0.65 mhos in the Northern

hemisphere at 01:50 UT and 0.54 mhos in the Southern hemisphere at 01:15 UT. An average background Pedersen conductivity of 0.21 mhos in the Northern hemisphere and 0.09 mhos in the Southern hemisphere was added to the conductivity due to electron precipitation. The background conductivity values were estimated using the IRI-2007 model ionosphere [*Bilitza and Reinisch*, 2008]. The height-integrated Pedersen conductivity was assumed to be constant throughout the event due to the lack of high time resolution measurements. This might miss any finer variations but will provide us with a overview of the inter-hemispheric differences in Pedersen currents.

The cross-SAPS potential (V_{SAPS}) shown in the bottom panel, denotes the potential difference across the SAPS channel. It has been estimated using the relation between potential difference and the electric fields given by $V_{SAPS} = \int_{X_E}^{X_P} E \, \mathrm{d}x$. Here $\mathrm{d}x$ represents the latitudinal width of the SAPS channel and X_E, X_P represent the equatorward and poleward edges of the SAPS channel respectively. It is seen that the SAPS potentials track one another to the first order and that the SAPS potentials can reach several tens of kv.

The variations in estimated zonal velocities (at the location where V_{LOS} were maximum) observed in the BKS and FIR radars are presented in the top panel of Figure 2.12. It can be noted from the figure that the velocities are in general higher in the Southern hemisphere and they differ not only in magnitudes, but also in their temporal variations. The results from correlation analysis also show that the velocities exhibit moderate correlation between the hemispheres and with the Asym-H index. These inter-hemispheric differences suggest that although the velocities in the SAPS channel are influenced by the strength of the asymmetric ring current, there are other local factors such as the height integrated Pedersen conductivity which have a strong influence on the electric fields in the ionosphere. Some inter-hemispheric differences in the magnitude of the flows (up to 15%) can be expected because of the SAA. However, the differences observed here are much stronger (reaching up to 90%) than those

expected due to the anomaly.

From the second panel of Figure 2.12 it can be observed that the estimated Pedersen current densities are generally higher in the Southern hemisphere compared to the Northern hemisphere. This is consistent with results presented in previous studies such as [*Ohtani et al.*, 2005; *Fujii and Iijima*, 1987] which demonstrated through statistical analyses that the Region-2 field aligned currents are more intense in the winter hemisphere (Southern hemisphere in this study) compared to the summer hemisphere on the nightside. The most likely causes for these differences were suggested to be asymmetric driving in the magnetosphere and the effects of seasonal differences in ionospheric conductivity [*Ohtani et al.*, 2005; *Fedder and Lyon*, 1987; *Ridley*, 2007; *Ridley et al.*, 2004].

Another important feature of a SAPS channel is its latitudinal width (third panel of Figure 2.12). It can be observed from the figure that the latitudinal width of the channel is different in both the hemispheres. A similar inter-hemispheric difference in the separation between electron and ion precipitation boundaries and the observations made in DMSP ion drift meter were noted Section-3.1, which corroborates the difference observed by the radars. The boundaries of the SAPS channel in both hemispheres map along the magnetic field lines into the inner magnetosphere at $\sim 4\ R_E$, where the Earth's magnetic field is generally expected to be very close to dipolar. A quasi-dipolar field suggests that the latitudinal width of the channel should be similar in both the hemispheres, unlike the observations presented here. Magnetic mapping of the SAPS channel showed that the Tsyganenko - 'T96', 'T01' and 'T04S' models [*Tsyganenko and Stern*, 1996; *Tsyganenko*, 2002a; *Tsyganenko and Sitnov*, 2005] do not predict the inter-hemispheric differences in latitudinal width observed here, for the geomagnetic conditions during the event. The results presented in *Tsyganenko et al.* [2003] and *Tsyganenko and Sitnov* [2005], showed that during severe geomagnetic storms (Dst index $\leq$ -250 nT) the quasi-dipolar approximation of the geomagnetic field breaks down at

distances as small as $\sim$ 4-5 R_E and the field starts exhibiting a tail like deformation. However during the event presented in the current paper, the Dst index reached a peak value of -65 nT. This suggests the possibility of a tail like distortion in the Earth's magnetic field at mid-latitudes even during moderate geomagnetic storms.

The final and most interesting feature of SAPS we examine is the potential across the channel, presented in the last panel of Figure 2.12. Unlike the other features, the cross-SAPS potentials exhibited a lot of similarity in both magnitudes and temporal variations between the hemispheres. The high-degree of similarity in cross-SAPS potentials estimated in both hemispheres was further verified by a strong correlation coefficient of 0.81 between BKS_{POT} and FIR_{POT} (Table 2.1). It is important to note here that the latitudinal width has a significant influence on the cross-SAPS potentials. The electric fields were in general higher in the Southern hemisphere, whereas the latitudinal width of the channel was greater in the Northern hemisphere. These influences seem to counterbalance each other, reconciling the differences in velocity and latitudinal width with similar cross-SAPS potentials in the two hemispheres. This suggests that, in spite of the presence of asymmetries between the hemispheres, there is overall consistency in terms of the conjugate mapping of potential variations between the hemispheres. The similar potential differences across the Northern and Southern hemisphere channels likely implies the absence of any field-aligned potential drops.

2.5 Conclusions

In this paper, simultaneous observations of latitudinally narrow high velocity flow channels made by SuperDARN radars in both hemispheres with magnetically conjugate fields-of-view were presented. Examination of the geomagnetic conditions and the features of the channel such as its subauroral location indicated that these were SAPS channels. The line-

of-sight velocities observed by the radars were seen to exhibit a nearly sinusoidal dependence on the magnetic azimuth. A sine curve fitting showed that the direction of flow was nearly westwards in both the hemispheres. A correlation analysis revealed that the latitudinal location of the SAPS channel in both hemispheres was related to the strength of the asymmetric ring current, showing that the location of SAPS channel is influenced by the asymmetric ring current . However, the variations in the velocity of the channel exhibited a moderate correlation with the Asym-H index indicating that local ionospheric conditions such as the height integrated Pedersen conductivity have an important influence on the channel.

An inter-hemispheric comparison of electric fields, Pedersen currents and cross-SAPS potentials showed that the Pedersen currents and electric fields exhibited substantial differences between the hemispheres. This can be attributed to seasonal differences in ionospheric conductivity between hemispheres, inner magnetospheric magnetic distortion or asymmetric driving of field-aligned currents in the magnetosphere. However, it was seen that the cross-SAPS potentials in both the hemispheres were similar not only in magnitudes but also in temporal variations. The greater consistency in terms of cross-SAPS potentials was due to compensating differences in SAPS velocities and channel widths between the hemispheres. Thus we can conclude that the SAPS phenomenon is consistent with conjugacy in terms of potential variations while exhibiting significant differences in latitudinal extent and convection velocities.

Acknowledgments

The authors thank the National Science Foundation for support under grants ATM-0849031, ATM-0946900 and AGS-1150789. The Blackstone SuperDARN radar was built with funds provided by NSF and with contributions from University of Leicester (UK) and Virginia Tech. The Falkland Islands SuperDARN radar was supported by the UK Natural

Environment Research Council grants NE/G019665/1 and NE/G018707/1. The DMSP particle detectors were designed by Dave Hardy of AFRL and data obtained from JHU/APL. DMSP SSIES ion drift meter data is collected by the US Airforce weather agency and processed by NOAA's National Geophysical Data Center. Kp, Sym-H and Asym-H indices were obtained from the World Data Center in Kyoto. The OMNI data were obtained from the GSFC/SPDF OMNIWeb interface at http://omniweb.gsfc.nasa.gov.

Chapter 3

IMF B_Y associated inter-hemispheric asymmetries in dayside auroral zone ionospheric convection on closed magnetic field lines

B. S. R. Kunduri,[1] J. B. H. Baker,[1] J. M. Ruohoniemi,[1] L. B. N. Clausen,[2] A. J. Ribeiro,[1] A. Marchaudon,[3,4] and M. Lester[5]
Journal of Geophysical Research, Under Review.

[1] Bradley Department of Electrical and Computer Engineering, Virginia Tech, Blacksburg, Virginia, USA
[2] Department of Physics, University of Oslo, Postboks 1048 Blindern, 0316 OSLO, Norway.
[3] Universitė de Toulouse; UPS-OMP; IRAP, Toulouse, France.
[4] CNRS; IRAP; 9 Av. colonel Roche, BP 44346, F-31028 Toulouse cedex 4, France.
[5] Department of Physics, University of Leicester, Leicester LE1 7RH, United Kingdom.

Abstract

It is widely known that the B_Y component of the interplanetary magnetic field (IMF) generates interhemispheric asymmetries in polar cap ionospheric convection on open magnetic field lines. Some studies suggest an IMF B_Y generated electric field can also penetrate into the closed field line region producing an interhemispheric potential drop, thereby differences in dayside auroral zone ionospheric convection. However this has not been verified directly using conjugate measurements. In this paper we use interhemispheric SuperDARN observations of high latitude ionospheric convection in the noon-dusk sector to show that the sunward convection is stronger in the northern (southern) hemisphere when IMF B_Y is positive (negative), irrespective of the season. The observations support the existence of an IMF B_Y associated interhemispheric potential difference and the resultant flow of field

aligned currents between the hemispheres. Four events (3 IMF B_Y negative and 1 IMF B_Y positive) are analyzed and the strength of the interhemispheric currents are estimated. The strength of the interhemispheric currents are found to depend on the magnitude of IMF B_Y, proximity of the currents to open-closed field line boundary, ionospheric conductivity, and magnetic local time.

3.1 Introduction

The influence of the interplanetary magnetic field (IMF) on high-latitude ionospheric convection has been a subject of extensive study since the earliest days of the space age [*Dungey*, 1961; *Mansurov*, 1970; *Svalgaard*, 1973; *Crooker*, 1979; *Reiff and Burch*, 1985; *Heppner and Maynard*, 1987; *Ruohoniemi and Greenwald*, 1996]. The role of IMF B_Y in producing dawn-dusk asymmetry in the convection pattern was discussed by *Crooker* [1979] and later extended by *Reiff and Burch* [1985]; *Cowley et al.* [1991]. It was suggested that a potential difference between the northern and southern hemisphere polar caps was generated due to IMF B_Y, leading to the flow of field aligned currents (FACs) along open magnetic field lines between the solar wind and polar caps [*Leontyev and Lyatsky*, 1974; *Burch et al.*, 1985; *Reiff and Burch*, 1985].

Some studies have suggested that IMF B_Y can also penetrate the closed field line region and produce interhemispheric asymmetries in convection on closed flux tubes [*Banks et al.*, 1984; *Clauer et al.*, 1984]. *Kozlovsky et al.* [2002, 2003] (referred to as the Kozlovsky model from here on) proposed a scenario to explain the influence of strong IMF B_Y on sunward dayside convection on closed field lines. Figure 3.1 presents a schematic explaining the Kozlovsky model when IMF B_Y is negative. The North-to-South directed electric field associated with IMF B_Y generates a potential difference between the northern and southern polar caps (part-A). The interhemispheric potential difference drives field-aligned currents, which enter the northern polar cap from the solar wind. The conducting ionosphere connects

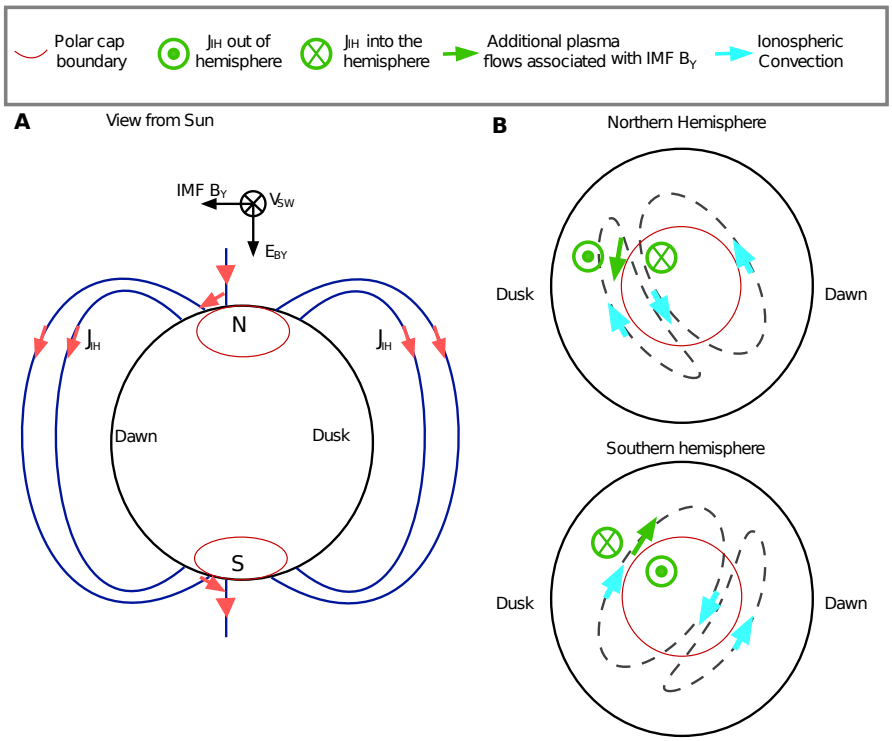

Figure 3.1: Diagram showing the influence of IMF B_Y in the closed magnetosphere according to the Kozlovsky model. The IMF B_Y negative scenario is presented. A) The interplanetary electric field ($\mathbf{E_{BY}}$) generated due to IMF B_Y and solar wind velocity ($\mathbf{V_{SW}}$) drives field aligned currents (FACs) into (out of) the northern (southern) polar cap. These polar cap FACs are connected via Pedersen currents to an interhemispheric FAC (j_{IH}) which flows north to south. B) Additional plasma flows ($\mathbf{E}\times\mathbf{B}$ drifts) in northern (upper panel) and southern (lower panel) hemispheres generated due to the j_{IH}. In the northern hemisphere these flows are directed opposite to the background ionospheric convection (blue arrows) but reinforce the direction of ionospheric convection in the southern hemisphere.

the footprints of the closed and open magnetic field lines and, thus, provides a path for the currents to penetrate the closed field line region. The IMF B_Y driven currents then flow to the other (southern) hemisphere along magnetic field lines and exit through the southern polar cap thus closing the circuit. The situation is reversed for the IMF B_Y positive case. A detailed explanation of the model is presented in *Kozlovsky et al.* [2003]. One major effect of these interhemispheric field aligned currents (referred to as J_{IH} from here on) is the generation of eastward (westward) ionospheric plasma flow immediately equatorward of the

polar-cap boundary in the northern (southern) hemisphere, as shown in part-B. For the IMF B_Y negative condition shown here, the eastward (westward) drift due to J_{IH} subtracts from (adds to) the westward plasma drift that is characteristic of the post-noon sector below the polar cap boundary [*Grocott et al.*, 2011; *Kunduri et al.*, 2012]. Consequently J_{IH} gives rise to an asymmetry between the hemispheres with weaker sunward flows expected in the post noon sector when IMF B_Y is negative and stronger sunward flows when B_Y is positive for the Northern hemisphere, the effect being reversed in the Southern hemisphere.

To date, this picture of IMF B_Y penetration into the closed field line region of the magnetosphere and its effects on magnetosphere-ionosphere coupling has not been verified with direct measurements because of the scarcity of simultaneous conjugate observations of ionospheric convection. The SuperDARN radars provide excellent opportunities to make simultaneous observations of ionospheric convection in magnetically connected regions. In the current paper we use interhemispheric SuperDARN measurements of ionospheric convection near the dayside open-closed field line boundary (OCB) to test the Kozlovsky model. We primarily examine observations made by the King Salmon and Hankasalmi (HAN) radars in the northern hemisphere and the Tiger , Unwin and Kerguelen (KER) radars in the southern hemisphere. Four events with strong IMF B_Y during different seasons are analyzed and the observed inter-hemispheric asymmetries are used to parameterize the strength of the inter-hemispheric field aligned currents by IMF B_Y magnitude, proximity to the OCB, ionospheric conductance and magnetic local time.

In the following sections we begin with a review of the datasets and models used in the study. We then discuss the interhemispheric differences in the observations made by SuperDARN radars in the post-noon closed field line region and present an analysis of the influence of different factors on the observed differences.

3.2 Datasets

3.2.1 SuperDARN HF Radars

The primary data used in this study are measurements of ionospheric plasma drift observed by SuperDARN HF radars [*Greenwald et al.*, 1985; *Chisham et al.*, 2007]. SuperDARN radars observe coherent backscatter from decameter-scale irregularities in the F region ionosphere that are aligned with the magnetic field. The Doppler shift of the backscattered signal is proportional to the line-of-sight component of the $\mathbf{E} \times \mathbf{B}$ plasma drift in the scattering region [*Ruohoniemi et al.*, 1987]. In the standard operating mode the radars scan through 16 beam directions covering an azimuth sector of about 50°. The radar scan time is typically 1-2 minutes corresponding to a dwell time of 3.5 or 7 seconds per beam. The line-of-sight Doppler velocities measured by all the SuperDARN radars are used to generate global convection maps at 1-2 minute cadence [*Ruohoniemi and Baker*, 1998].

3.2.2 Other datasets and models

The primary motivation of this paper is to test the predictions of the Kozlovsky model by comparing ionospheric convection velocities in the northern and the southern hemispheres on magnetically conjugate locations during sustained conditions of IMF B_Y positive or negative. A reliable magnetic field model is required to make the interhemispheric comparisons. This is achieved by using the IGRF model for internal sources and the Tsyganenko model T01 [*Tsyganenko*, 2002a] for external (magnetospheric) current sources. The external contributions to the magnetospheric magnetic field are specified by Tsyganenko models through mathematical formalism and empirical modeling. The Tsyganenko T01 model requires the Dst index, solar wind dynamic pressure, IMF B_Y and IMF B_Z as inputs. The Dst index and Kp index were accessed through the World Data Center for Geomagnetism - Kyoto, Japan.

Table 3.1: Summary of parameters for all events (Event-1 : Feb 16, 2005, Event-2 : May 29, 2005, Event-3 : June 4, 2010 and Event-4 : March 17, 2010). j_{IH}^{MEAN} refers to the mean values of inter-hemispheric current density shown in Figure 3.6. ΔLAT_{jIH} refers to the latitudinal width of the inter-hemispheric currents. $\Sigma_N^{P,FUV}$, $\Sigma_S^{P,FUV}$ are the height integrated Pedersen conductivities from IRI in the northern and southern hemispheres respectively. $\Sigma^{P,AUR}$ represents height integrated Pedersen conductivity from *Hardy et al.* [1987] auroral conductance model.

Events	IMF-B_Y	IMF-B_X	IMF-B_Z	$j_{IH}^{MEAN}(\mu A/m^2)$	ΔLAT_{jIH}	$\Sigma_N^{P,FUV}$(mhos)	$\Sigma_S^{P,FUV}$(mhos)	Σ
Event-1	-9 nT	8 nT	-4 nT	-0.28	2°	2.1	1.7	
Event-2	-7.5 nT	5 nT	2 nT	-0.37	4°	5.1	2.8	
Event-3	-5 nT	3 nT	-6 nT	-0.59	6°	5.3	2.6	
Event-4	+7 nT	-3.5 nT	-2 nT	0.37	1.5°	3.1	2.2	

The IMF data such as IMF-B_Z and IMF-B_Y were accessed from the OMNI 2 data set at the National Space Science Data Center (NSSDC) [*King and Papitashvili*, 2005].

3.3 Observations

In this section we analyze four events : Feb 16, 2005 (Event-1), May 29, 2005 (Event-2), June 4, 2010 (Event-3) and March 17, 2010 (Event-4). These events are selected because IMF B_Y remained consistently positive/negative for a considerable interval of time (more than 1 hour) and conjugate SuperDARN measurements of dayside ionospheric convection on closed field lines were available simultaneously in both hemispheres. Tables 3.2 and 3.1 show the solar wind and geomagnetic conditions during the events. We present the line-of-sight Doppler velocity (V_{LOS}) measurements made by the SuperDARN radars, the two-dimensional velocity vectors obtained by fitting the velocity data according to the standard technique of *Ruohoniemi and Baker* [1998] and the IMF conditions during the events. We use the interhemispheric SuperDARN measurements to derive J_{IH} generated due to IMF B_Y on closed field lines. The first three events occurred when IMF B_Y was negative and Event-4 when IMF B_Y was positive.

Table 3.2: Summary of parameters used as inputs for Tsyganenko 'T01' model during each of the events (Event-1 : Feb 16, 2005, Event-2 : May 29, 2005, Event-3 : June 4, 2010 and Event-4 : March 17, 2010) presented in the study. Solar wind dynamic pressure (pdyn), Dst-index, IMF B_Y, B_Z are shown in the table.

Events	pdyn	Dst	IMF-B_Y	IMF-B_Z
Event-1	2.0	0.0	-9 nT	-4 nT
Event-2	3.0	-10.0	-7.5 nT	2 nT
Event-3	2.0	-37.0	-5 nT	-6 nT
Event-4	1.5	3.0	7 nT	-2 nT

3.3.1 Events 1 and 2 : Feb 16, 2005 and May 29, 2005

Figure 3.2 presents time series of IMF conditions and V_{LOS} measured during Event-1 between 1200 and 1500 UT. IMF B_X (top panel) stayed positive during the entire interval. The IMF B_Y component (second panel) was predominantly negative reaching a peak value of -10 nT. IMF B_Z (third panel) was predominantly negative except for short intervals towards the end of this period. The last two panels show the V_{LOS} measurements from Hankasalmi (HAN) beam-13 and Kerguelen (KER) beam-10. Both radars observed ionospheric convection between 65° and 75° MLAT. The vertical dashed line in the figure marks the time instance presented in Figure 3.3. Of particular note is the fact that the line-of-sight velocities measured in the southern hemisphere by the KER radar were significantly stronger than those measured by the HAN radar in the northern hemisphere. On the basis of conjugacy we would expect these line-of-sight velocities to be similar (or infact greater in HAN due to its more zonal orientation) because of the similarity in the observation of these beams (marked in Figure 3.3). However, the impression is that much stronger and more organized flows were observed by the radar in the southern hemisphere. Moreover, a region of positively directed line-of-sight velocities (indicated by green color) is observed in beam-13 of the HAN radar. These velocities are oppositely directed to the background ionospheric convection measured by the radars (indicated by negative line-of-sight velocities) and their existence

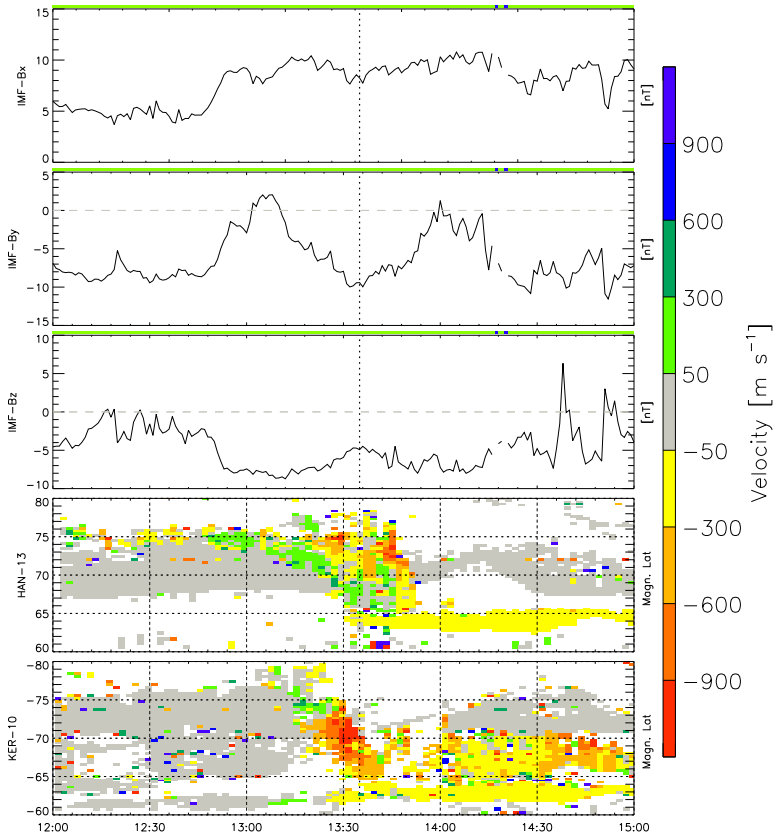

Figure 3.2: Time series of IMF and SuperDARN data on Feb 16 2005 (Event-1). Upper three panels show IMF B_X, B_Y and B_Z. The lower three panels show V_{LOS} observed by HAN (beam 13) and KER (beam 10) radars versus magnetic latitude (vertical) and universal time (horizontal). Doppler velocities are colored according to the scale at the right (see Figure 3.3 for orientation of these beams). The dashed vertical line indicates the time at which measurements shown in Figure 3.3 were made. Backscatter due to reflection from the ground after reflection from the ionosphere is colored grey.

adds support to the presence of negative IMF B_Y associated flows suppressing background ionospheric convection in the northern hemisphere, as shown in Figure 3.1.

Figure 3.3 shows the overall patterns of ionospheric convection in the northern hemisphere (left panel) and the southern hemisphere (right panel), during Event-1. The fitted ionospheric ($\mathbf{E} \times \mathbf{B}$) convection velocities are displayed on a map marked in Magnetic Latitude-Magnetic Local Time (MLAT-MLT) coordinates with contours of ionospheric electric potential superposed. Fitted velocity vectors are plotted where velocity data was

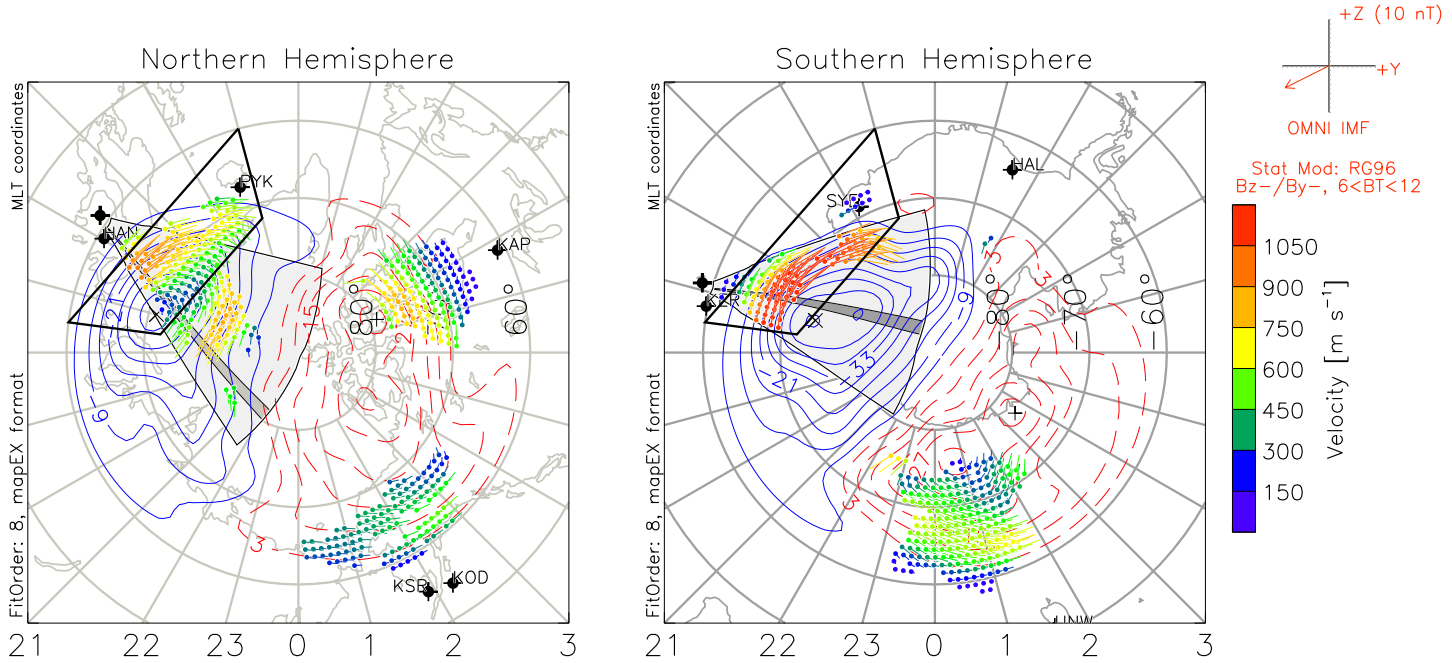

Figure 3.3: Ionospheric electric potential contours and vectors of convection flow derived from SuperDARN measurements overlayed on a map marked in MLT-MLAT grid. The measurements were made on Feb 16, 2005 during the scan at 1334-1336 UT (northern winter). The left panel shows the northern hemisphere and the right panel shows the southern hemisphere. The IMF dial at the top right shows the IMF conditions (from OMNI dataset). The boxed area marks the region of interest where interhemispheric observations are made. Fields of view of HAN (beam-13 highlighted) and KER (beam-10 highlighted) are overlayed for reference.

measured directly by at least one of the radars in the given hemisphere. A background statistical model [*Ruohoniemi and Greenwald*, 1996] is used to constraint the fitting at locations where direct measurements are not available. The dial in the upper right corner indicates the IMF clock angle provided by the OMNI dataset. The boxed area marks the region of interest where measurements of ionospheric convection were made simultaneously in both hemispheres on closed field lines. Although we do not have simultaneous determination by measurements of the OCB, we can infer that the higher velocity fitted vectors in the boxed areas are associated with closed field lines due to their equatorward positioning relative to the convection reversal boundary [*Newell et al.*, 2004]. Moreover, estimates from the Tsyganenko

model also indicate the measurements are on closed field lines during this interval for the prevailing solar wind and magnetic conditions. A majority of the observations were obtained by the HAN radar in the northern hemisphere and KER radar in the southern hemisphere (fields-of-view overlayed in respective panels). Over the boxed areas the flows are clearly associated with the return flow within the dusk convection cell. Consistent with Figure 3.2, the ionospheric convection velocity in the southern hemisphere is much higher (peak value of 1200 m/s) compared to the northern hemisphere (peak value of 750 m/s). Moreover, the difference in velocities cannot be considered as an effect of the model because significant interhemispheric differences in V_{LOS} are observed in KER and HAN radars as well (shown in Figure 3.2). The difference is qualitatively consistent with the predictions of the Kozlovsky model, whereby stronger flows are expected in the post-noon closed field line region in the Southern hemisphere for IMF B_Y negative conditions. However, difference in ionospheric conductivity might be expected to play a role in producing the observed interhemispheric differences. Event-1 occurred during northern winter when the northern hemisphere ionospheric conductivity is lower and the convection might therefore be expected to be higher as higher conductivity tends to suppress the electric fields. This is not the case.

To further examine the possible role of ionospheric conductivity we present a second event for which a similar asymmetry was observed during strong negative IMF B_Y but at a different time of year. Figure 3.4 is plotted in the same format as Figure 3.3 but for Event-2 (May 29, 2005 at 0240 UT). The boxed area marks the region of interest showing measurements of ionospheric convection. Again, the flows in this region belong to the post-noon closed field line region. Figure 3.4 demonstrates that convection velocities in the region of interest reach a peak value of about 1000 m/s in the southern hemisphere and about 600 m/s in the northern hemisphere, similar to the observations during Event-1. This is again consistent with the Kozlovsky model.

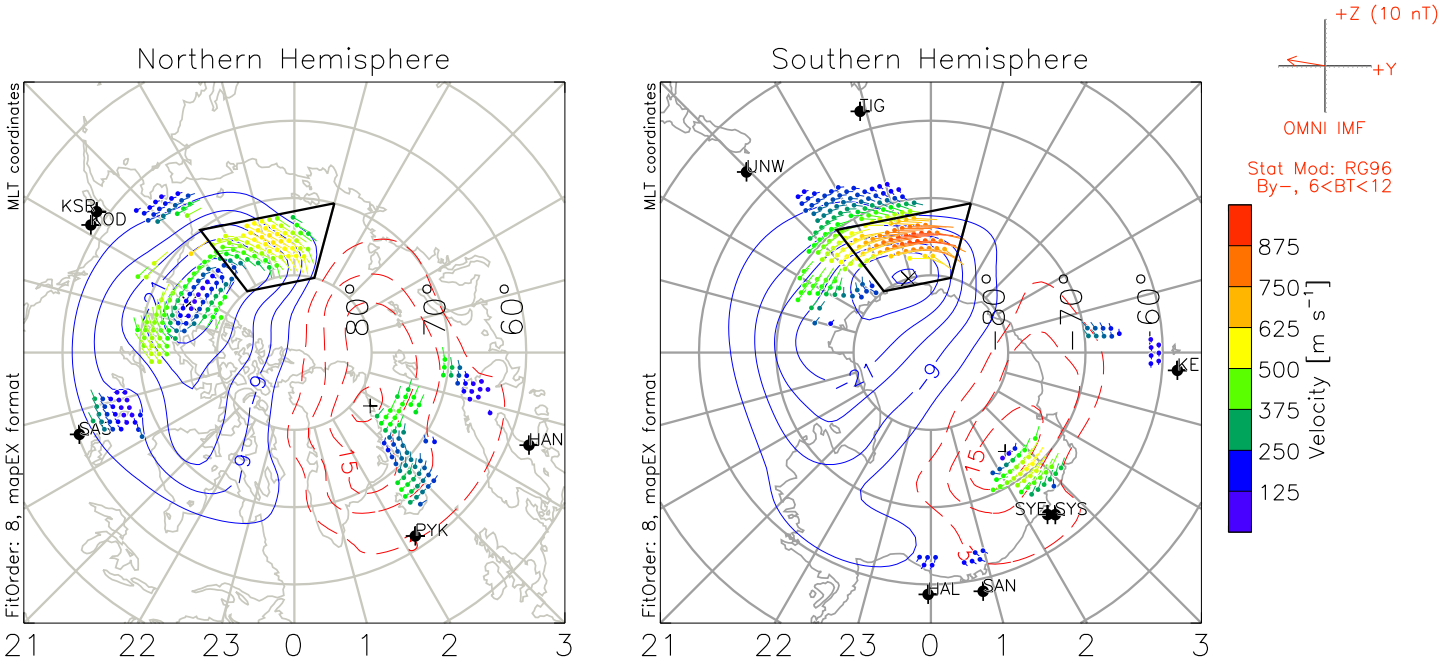

Figure 3.4: Same format as Figure 3.3 but for the event on May 29, 2005 during the scan at 0238-0240 UT (northern summer). The boxed area marks the region of interest.

In summary, Figures 3.3 and 3.4 clearly show that ionospheric convection is stronger in the southern hemisphere when IMF B_Y is negative during both events, irrespective of the season, over the region of closed field lines that lies equatorward of the OCB in the post noon sector.

3.3.2 Interhemispheric mapping of ionospheric convection

In the previous subsection we demonstrated that sunward ionospheric convection on closed magnetic field lines is stronger in the southern hemisphere during strong negative IMF B_Y, irrespective of season. This rules out the possibility that ionospheric conductivity is the dominant influence for these two events. However, other factors such as the difference in magnetic field strength between the hemispheres, dipole offset and the asymmetric deformation of magnetic field lines during disturbed geomagnetic conditions [*Tsyganenko*, 2002a; *Tsyganenko et al.*, 2003; *Tsyganenko and Sitnov*, 2005] could also be responsible for

producing interhemispheric differences in ionospheric convection. For example, even if the same electric field is observed in both the hemispheres, one reason the convection velocity ($\mathbf{E} \times \mathbf{B}$ drift) can be different is due to a difference in the magnetic field strength in magnetically conjugate locations. In this subsection, we analyze the influence of these factors and present a quantitative interhemispheric comparison of ionospheric convection velocities on closed magnetic field lines for these two events and two additional ones.

In order to quantitatively test the interhemispheric conjugacy of SuperDARN measurements on closed field lines, convection velocities in the southern hemisphere were mapped into the northern hemisphere along magnetic field lines and compared with the corresponding measurements in the northern hemisphere. The interhemispheric mapping was implemented using a procedure similar to that described in *Baker et al.* [2004] using the Tsyganenko 'T01' model [*Tsyganenko*, 2002a]. From here onward the southern hemisphere convection velocities mapped into the northern hemisphere will be referred to as "estimated northern velocities" and the velocities derived from the actual measurements in the northern hemisphere will be referred to as "northern velocities". The mapping procedure is now described :

The magnitude of ionospheric convection velocity ($\mathbf{E} \times \mathbf{B}$ drift) within a flux tube can be represented as

$$V = E/B = \Delta\Phi/(Bd) \tag{3.1}$$

Where V represents velocity magnitude, B the magnetic field strength, d the flux tube thickness, and $\Delta\Phi$ the potential difference across the flux tube. If we assume equal potential drop across the northern and the southern ionospheric ends of a flux tube we can estimate the velocity magnitude in the northern hemisphere using measurements from the southern hemisphere, as :

$$V_N^E = V_S(\frac{B_S d_S}{B_N d_N}) \tag{3.2}$$

Where the subscripts 'S'('N') represent quantities in the southern(northern) hemisphere and the superscript 'E' represents an estimate in one hemisphere based on measurements in the other. The direction of the estimated velocity is found by mapping two separate magnetic field lines aligned along the direction of the measured velocity. In Figure 3.5 we present an overview of the ionospheric convection velocity maps for all four events analyzed in this study. The left side panels show southern velocities, the middle panels show estimated northern velocities (obtained from Equation 3.2) and the right side panels show the northern velocities. The concentric circles indicate the open field line region predicted by the Tsyganenko 'T01' model for the geomagnetic conditions during the event. The inputs used for the Tsyganenko model for each event are shown in Table 3.2. Time-coincident and magnetically conjugate measurements are indicated by black markings. The Tsyganenko model as well as the direction of convection indicate that the measurements lie on closed field lines. Figure 3.5 shows that estimated northern velocities are higher compared to northern velocities during the first three events (IMF $B_Y < 0$ intervals). For the last event (IMF $B_Y > 0$ interval) northern velocities were higher compared to estimated northern velocities, consistent with the IMF B_Y component being the dominant influence.

In summary, we have demonstrated that, after accounting for interhemispheric differences in magnetic field strength and field line distortion, ionospheric convection is still observed to be stronger on closed field lines in the southern (northern) hemisphere when IMF B_Y is negative (positive). The interhemispheric asymmetries thus appear to be consistent with the flow of j_{IH} and indicate the penetration of IMF B_Y into the closed magnetosphere as suggested by *Kozlovsky et al.* [2003].

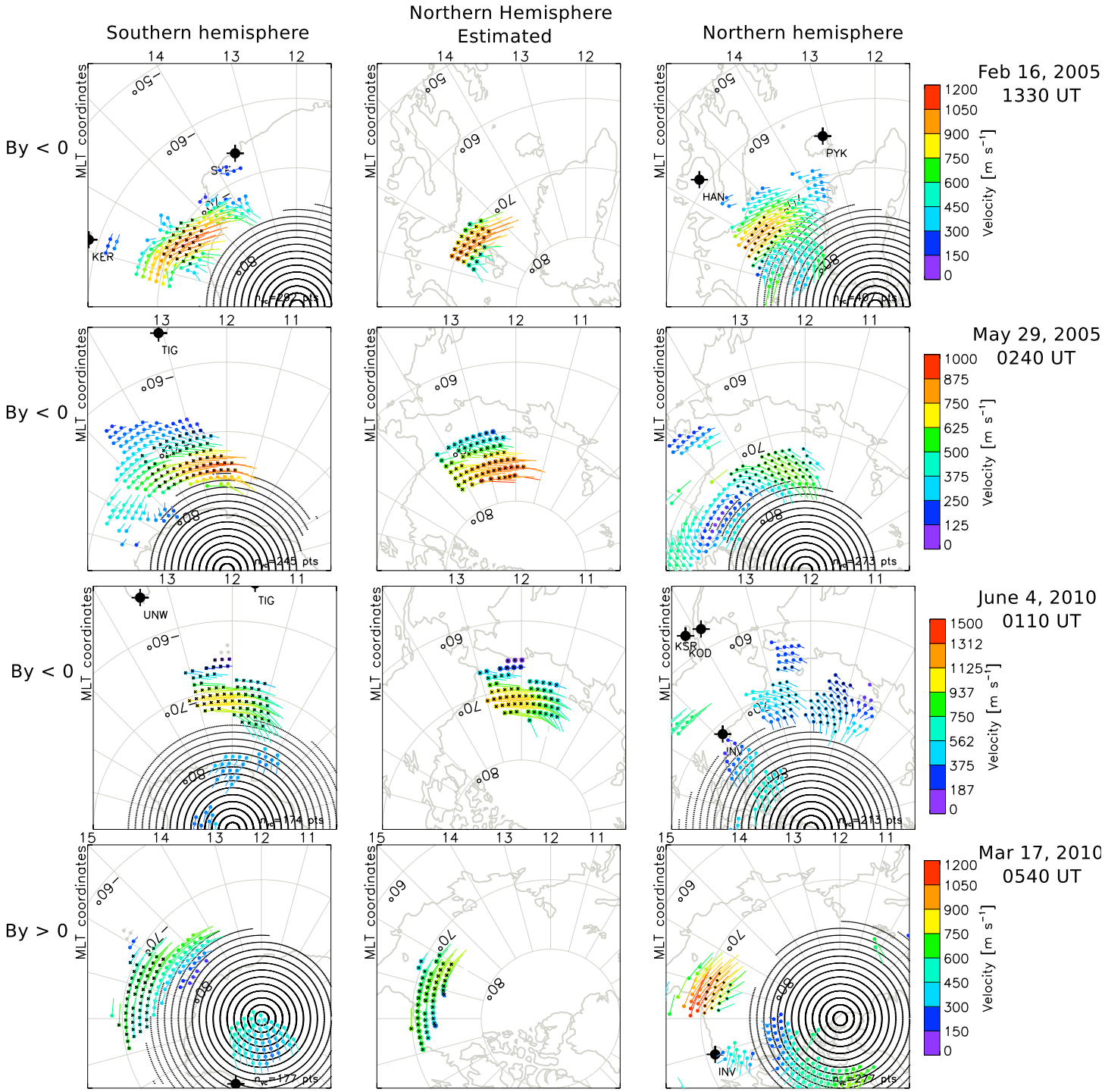

Figure 3.5: Interhemispheric comparison of convection velocities on closed field lines for all four events. The left panel shows convection velocities observed in the southern hemisphere, the middle panel shows the southern convection velocities mapped into the northern hemisphere and the right panel shows convection velocities observed in the northern hemisphere. The concentric circles indicate the open field line region predicted by the Tsyganenko T01 magnetic field model using geomagnetic conditions during the event.

3.3.3 Interhemispheric field-aligned currents

In this subsection, we estimate the strength of the interhemispheric field aligned currents (j_{IH}) from the differences in north-south convection and compare with the results of previous studies [*Kozlovsky et al.*, 2002, 2003; *Lukianova et al.*, 2010; *Lukianova and Kozlovsky*, 2011; *Guo and Wang*, 2010].

The horizontal current density ($\mathbf{J}_\perp$) in the ionosphere can be estimated using ohm's law, as :

$$\mathbf{J}_\perp = \Sigma^P \mathbf{E} - \Sigma^H (\mathbf{E} \times \mathbf{B})/B \tag{3.3}$$

Where $\mathbf{E}$, $\mathbf{B}$, Σ^P, Σ^H represent electric field, magnetic field, and height integrated Pedersen and Hall conductivities respectively.

Field aligned current density ($j_\parallel$) can be estimated as the divergence of horizontal current density, that is $j_\parallel = \nabla_\perp \cdot \mathbf{J}_\perp$. Since the events presented in the paper are on the dayside and not close to the terminator, it is a reasonable first order assumption to neglect the gradients associated with conductivity. The field aligned current density can then be estimated as $j_\parallel = \Sigma^P \nabla_\perp \cdot \mathbf{E}_\perp$. Under this assumption any observed differences in ionospheric convection between the hemispheres can thus be considered a consequence of an interhemispheric FAC given by :

$$j_{IH} = \Sigma^P_S \nabla_\perp \cdot \mathbf{E}_S - \Sigma^P_N \nabla_\perp \cdot \mathbf{E}_N \tag{3.4}$$

Where subscripts N, S refer to the conjugate northern and southern hemisphere quantities. Since the spatial extent of the measurements is small and the geometry of the field-

aligned currents and ionospheric flows is relatively simple, we reduce the problem to a local Cartesian coordinate system in calculating the divergence, similar to the derivations presented in *Lyons* [1980]; *Weimer et al.* [1985]. The electric fields (and thereby the ionospheric currents associated with them) in this study are estimated from auroral zone return $\mathbf{E} \times \mathbf{B}$ convection flows which are predominantly westwards and vary more rapidly with latitude than longitude. Thus the contribution from the azimuthal component of the electric fields is small compared to the meridional component and we simplify our equations accordingly. Moreover, the interhemispheric currents associated with IMF B_Y as discussed in the Kozlovsky model are generated by the divergence of meridional currents and the contribution from Hall currents is negligible. Under this assumption, the divergence in the azimuthal direction can be neglected and the equation can then be simplified to :

$$j_{IH} = \Sigma_S^P \frac{\partial E_S}{\partial \lambda} - \Sigma_N^P \frac{\partial E_N}{\partial \lambda} \tag{3.5}$$

Where λ now represents the meridional direction. SuperDARN measurements provide E_N and E_S while the solar FUV ($\Sigma^{P,FUV}$) and auroral components ($\Sigma^{P,AUR}$) of Pedersen conductance can be estimated from IRI-2007 model [*Bilitza and Reinisch*, 2008] and *Hardy et al.* [1987] respectively.

Figure 3.6 shows j_{IH} estimated using Equation 3.5 for all four events, overlayed on maps marked in MLAT-MLT coordinates. The conjugate coverage is limited to a narrow longitudinal sector in each of the events. The open field line region (predicted from Tsyganenko T01 model) is also overlayed. The current density for each event is scaled according to the color bar on the right. A negative value of current density indicates current flowing out of the ionosphere and a positive value indicates current flowing into the ionosphere. Of particular note is the fact that, j_{IH} is flowing out of (into) the northern hemisphere when

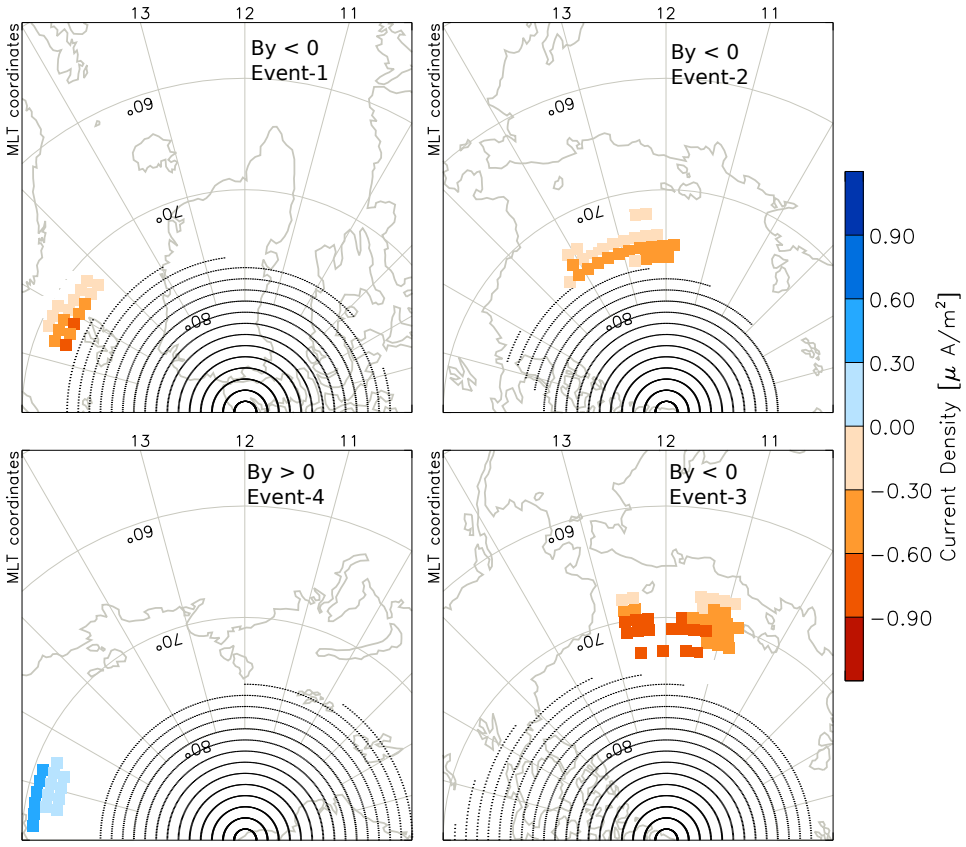

Figure 3.6: Magnitude of inter-hemispheric FACs (j_{IH}) on closed field lines over areas of conjugate SuperDARN velocity observations. Negative (red) indicate FACs out of the northern hemisphere and positive (blue) into the northern hemisphere. The concentric circles indicate the open field line region predicted by the Tsyganenko T01 magnetic field model using prevailing geomagnetic and solar wind conditions during the event.

IMF B_Y is negative (positive) irrespective of season as suggested by the Kozlovsky model. However, it is important to emphasize that we use different conductivity values for both hemispheres in Equation 3.5. That is, j_{IH} is made up of two components: one associated with conductivity differences between the two hemispheres (j_{IH}^{COND}), such as those discussed in *Benkevich et al.* [2000] and the other associated with differences in electric fields between the hemispheres (j_{IH}^{EFLD}). We attribute the differences observed in electric fields between the hemispheres predominantly to IMF B_Y. A crude separation between the two components can be achieved by considering what happens when a common conductance value is used in

both hemispheres. We thus estimate the electric field and conductivity components as:

$$j_{IH}^{EFLD} = \Sigma^P(\frac{\partial E_S}{\partial \lambda} - \frac{\partial E_N}{\partial \lambda}) \tag{3.6}$$

$$j_{IH}^{COND} = j_{IH} - j_{IH}^{EFLD} \tag{3.7}$$

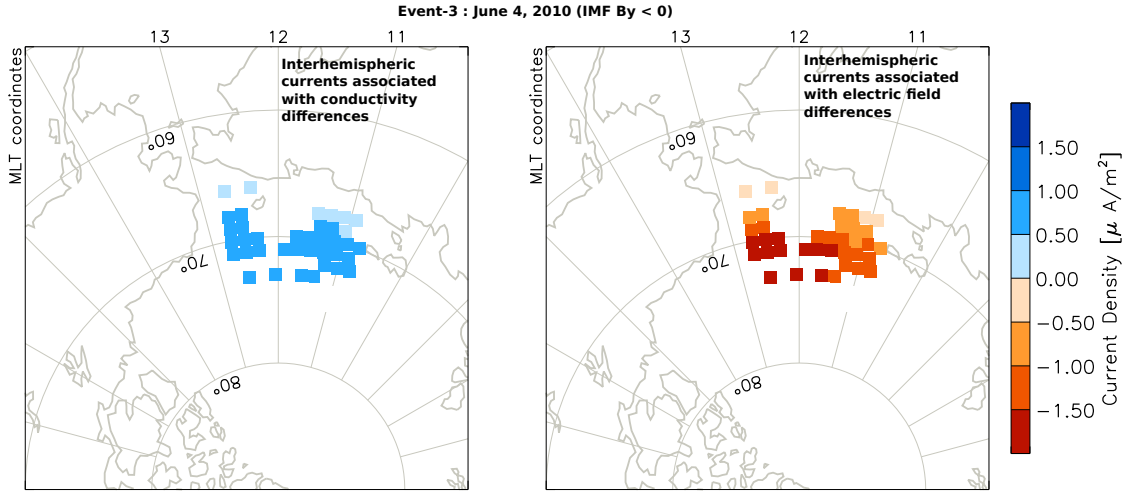

Figure 3.7: Estimates of the "conductance" and "E-field" components of j_{IH} for Event-3. Negative (red) indicate FACs out of the northern hemisphere and positive (blue) into the northern hemisphere. The left panel presents the component of j_{IH} attributed to conductivity differences and the right panel presents the component of j_{IH} attributed to differences in electric fields between the hemispheres.

Figure 3.7 presents these two components during Event-3 with j_{IH}^{COND} on the left and j_{IH}^{EFLD} on the right (note : since j_{IH}^{EFLD} is flowing out of the northern hemisphere we use northern hemisphere value for Σ^P). The peak magnitudes are $\sim$1 $\mu A/m^2$ for j_{IH}^{COND} and $\sim$2 $\mu A/m^2$ for j_{IH}^{EFLD}. In the next section, the spatial variability in the magnitude of j_{IH} will be explored further.

3.4 Spatial distribution of interhemispheric FACs

In the previous section, observations of ionospheric convection from SuperDARN radars in both hemispheres were used to demonstrate that strong IMF B_Y can produce interhemispheric asymmetries in ionospheric convection on closed field lines as suggested by *Kozlovsky et al.* [2003]. In this section, we further analyze the differences between the velocities and j_{IH} and examine their dependence on latitudinal location and magnetic local time.

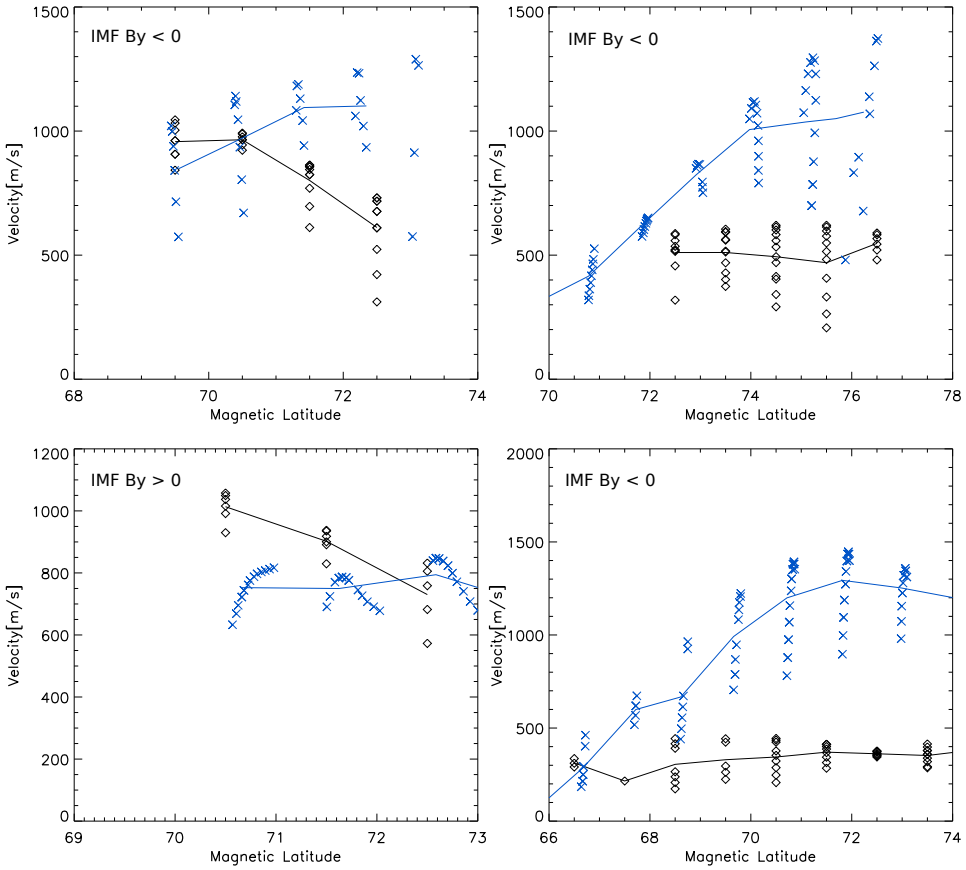

Figure 3.8: Latitudinal dependence of interhemispheric differences in fitted ionospheric convection velocities. Clockwise from top-left : Event-1, Event-2, Event-3 and Event-4. Blue - estimated northern velocities, black- northern velocities (described in text). The solid blue and black lines indicate the mean values of estimated northern velocities and northern velocities respectively, at each latitude.

In Figure 3.8, we present a comparison of the magnitudes of estimated northern velocities

and northern velocities as a function of latitude. It should be noted that during each of the events the measurements are limited to a region ∼2 hours in MLT in the noon-dusk sector on closed field lines. The flows in this region are predominantly sunwards and zonal (for example see the boxed regions in Figure 3), suggesting we are comparing plasma flows having similar direction. All four events are presented in the figure, clockwise from top-left : Event-1, Event-2, Event-3 and Event-4. The blue crosses indicate the estimated northern velocities and the black diamonds indicate northern velocities. Blue and black solid lines indicate the mean values of estimated northern velocities and northern velocities at each latitude respectively. All measurements shown in the plot fall in the closed field line region as shown in Figure 3.5. An important trait emphasized in the figure is that the interhemispheric difference in velocities is higher at higher latitudes and decreases in a systematic manner further equatorward. Table 3.1 presents a summary of various parameters for all four events such as the mean j_{IH} intensity (j_{IH}^{MEAN}) and latitudinal width of j_{IH} (ΔLAT_{jIH}) along with the IMF conditions and estimated Pedersen conductivities. ΔLAT_{jIH} is estimated manually from Figures 3.6 and 3.8. It should be noted that there is a possibility the radars were not making measurements of the complete channel so ΔLAT_{jIH} presented here could be the lower limit for some of the events. An important feature to be noted from the table is that ΔLAT_{jIH} increases with an increase in j_{IH}^{MEAN}. This could be attributed to the fact that stronger magnitude j_{IH} can reach farther (equatorward) from the polar cap boundary. The values of ΔLAT_{jIH} (1.5° to 6°) are in agreement with the MHD simulation results presented in *Guo and Wang* [2010] who predict the latitudinal width of the FACs to vary between 1° and 5°. The table also emphasizes certain other features such as the differences observed in j_{IH}^{MEAN} and ΔLAT_{jIH} even during similar geomagnetic conditions or seasons. For example, j_{IH} is higher during Event-3 compared to Event-2 even though both these events occur during northern summer and similar IMF B_Y values. The collective observations thus suggest a possible dependence of j_{IH} on latitude and MLT, which needs further investigation.

A strong latitudinal dependence, whereby interhemispheric differences in velocities (presented in Figure 3.8) are observed to be strongest just equatorward of the OCB and decrease with latitude from thereon is not unexpected. Since IMF B_Y associated interhemispheric currents are transferred from the polar cap region into the closed field line region through the conducting ionosphere (as shown in Figure 3.1), their effect should be most intense close to the OCB. To further investigate the variations in IMF B_Y associated currents with latitude and MLT, we fit the estimated values of j_{IH}^{EFLD} during all four events as a linear function of MLT and magnetic latitude (MLAT) using the Levenburg-Marquardt gradient method to minimize the least squares error during the fit. The results of the fitting are given by :

$$j_{IH}^{EFLD} = (-0.04 \times MLT + 0.01 \times MLAT) \times B_Y \tag{3.8}$$

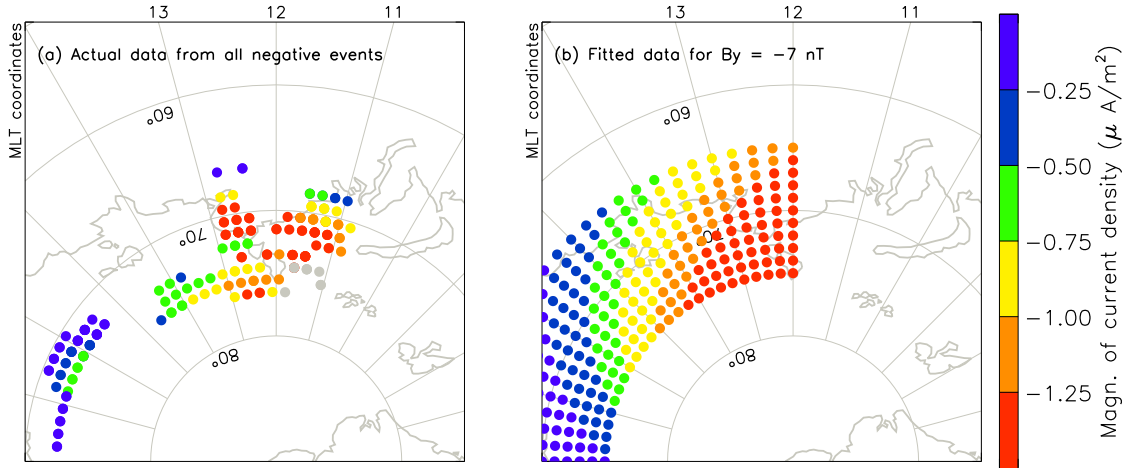

Figure 3.9: Magnitude of j_{IH}^{EFLD}, estimated from interhemispheric differences in convection for all the negative events (panel-a) and estimated from the fitting procedure (panel-b).

As expected, the equation shows that for a given value of IMF B_Y the current density decreases as we move duskwards from Noon or equatorwards from the polar cap boundary. The standard deviations of the coefficients of MLT and MLAT were calculated to be 0.0012 and 0.00028 respectively. It is important to note here that the main purpose of this fitting

is to demonstrate the MLT and MLAT variability in j_{IH}^{EFLD}. Figure 3.9 shows the fitting results during all negative IMF B_Y events. Panel (a) shows the magnitude of j_{IH}^{EFLD} observed and panel (b) shows the estimated values of j_{IH}^{EFLD} from Equation 3.8 when B_Y = -7 nT. Both panels (a) and (b) show that j_{IH}^{EFLD} exhibits a strong dependence on MLT and MLAT such that its magnitude decreases as we move towards dusk or lower latitudes. This MLT dependence is similar to the observations made in *Lukianova and Kozlovsky* [2011] where it was noted that the IMF B_Y related azimuthal flows were stronger near the noon-midnight meridian compared to the dawn-dusk meridian. This was attributed to a shift of the polar cap boundary of several degrees on the dawn-dusk side [*Cowley et al.*, 1991], resulting in the suppression of IMF B_Y related azimuthal flows by the oppositely directed DP2 transpolar flow. However, there are other important factors such as IMF B_Z [*Lukianova et al.*, 2010; *Lukianova and Kozlovsky*, 2011], IMF B_X [*Chisham et al.*, 2000; *Peng et al.*, 2010; *Lukianova and Kozlovsky*, 2011] and distance of the currents from the polar cleft [*Banks et al.*, 1984] which can also play an important role in producing the changes in interhemispheric currents with MLT. The anomalies observed during Event-4 in Figure 3.8 could be attributed to the above mentioned factors. However quantifying the nature and extent of the influence of all the factors requires a much larger database and is beyond the scope of the current paper.

In summary, the observations presented in this study support the existence of an interhemispheric field aligned current system generated due the penetration of IMF B_Y into the closed magnetosphere [*Kozlovsky et al.*, 2003]. Here, we demonstrate for the first time directly using interhemispheric measurements of ionospheric convection from SuperDARN radars that the strength and latitudinal width of the interhemispheric currents exhibit dependence on latitudinal location with respect to the OCB, magnetic local time, strength and orientation of IMF and ionospheric conductivity as predicted by the Kozlovsky model.

3.5 Conclusions

In this paper, simultaneous measurements of high latitude ionospheric convection on closed magnetic field lines derived from SuperDARN HF radars in both hemispheres were presented. Substantial interhemispheric differences in convection velocities were observed in magnetically conjugate regions. When IMF B_Y was positive (negative) the convection velocities were higher in the northern (southern) hemisphere, irrespective of the season. These differences strongly suggest the presence of an interhemispheric asymmetry in ionospheric convection on closed magnetic field lines that can be attributed to the existence of IMF B_Y dependent interhemispheric currents (j_{IH}). The mean values of j_{IH} varied between 0.28 and 0.59 $\mu A/m^2$ in magnitude; j_{IH} was found to vary between 1.5° and 6° in latitudinal width; and stronger j_{IH} were associated with larger latitudinal widths. j_{IH} were found to be strongest just equatorward of the polar cap boundary and at noon MLT and decreased equatorwards of the open-closed field line boundary or towards later MLTs. These characteristics are attributed to the dependence of j_{IH}^{EFLD} on conductivity and variations in polar cap boundary with MLT.

Acknowledgments

The authors thank the National Science Foundation for support under grants ATM-0946900 and AGS-1150789. Mark Lester acknowledges support from the STFC grant ST/K001000/1. The SuperDARN Kerguelen radar is a franco-italian project currently funded by INSU/CNRS and IPEV (France). Kp, Sym-H and Asym-H indices were obtained from the World Data Center in Kyoto. The OMNI data were obtained from the GSFC/SPDF OMNIWeb interface at http://omniweb.gsfc.nasa.gov.

Chapter 4

Statistical characterization of the large-scale structure of the sub-auroral polarization stream

B. S. R. Kunduri,[1] J. B. H. Baker,[1] J. M. Ruohoniemi,[1] E. G. Thomas,[1] S. G. Shepherd,[2] and K. T. Sterne[1]
Journal of Geophysical Research, Under Review.

[1] Bradley Department of Electrical and Computer Engineering, Virginia Tech, Blacksburg, Virginia, USA.

[2] Thayer School of Engineering, Dartmouth College, Hanover, New Hampshire, USA.

Abstract

The Sub-Auroral Polarization Stream (SAPS) is a latitudinally narrow region of westward-directed flows observed equatorward of the auroral oval. Previous studies have shown SAPS generally occur during geomagnetically disturbed conditions and the location and velocities within the SAPS channel exhibit a strong dependence on geomagnetic activity. In this paper, we present the first comprehensive statistical study of SAPS using measurements obtained by the North American chain of mid-latitude SuperDARN radars. The study period spans January 2011 to August 2012 and the results show that SuperDARN radars observe SAPS channels over a broad range of activity levels specified by the Dst geomagnetic index. During relatively quiet conditions (Dst > -10nT) SAPS were observed 9% of the time and tend to be localized to the midnight sector and centered at 62° magnetic latitude. As the activity level increases, and Dst decreases, the SAPS channel shifts equatorwards and rotates duskwards. During moderate storm conditions (-75 nT < Dst < -50 nT) SAPS are observed 95% of the time, and tend to be centered at 20 magnetic local time and 57° magnetic latitude. The speed of the flows in the SAPS channel is also examined. During quiet-to-moderate

conditions (Dst > -50 nT) SAPS flows exhibits a quasi-exponential dependence on local time, with flows being strongest near dusk. However, this dependence tends to break down at higher activity levels and this could be attributed to the increase in conductivity as the channel crosses the day-night terminator on the duskside.

4.1 Introduction

Sub-auroral polarization stream (SAPS) is a term introduced by *Foster and Burke* [2002] to describe strong westward plasma flows in the mid-latitude ionosphere equatorward of the auroral convection zone. SAPS flows tend to be latitudinally narrow and are predominantly observed in the dusk-midnight sector, either just equatorward or at the edge of the auroral oval [*Anderson et al.*, 1993, 2001; *Parkinson et al.*, 2005; *Koustov et al.*, 2006; *Oksavik et al.*, 2006; *Makarevich and Dyson*, 2008; *Grocott et al.*, 2011; *Kunduri et al.*, 2012]. SAPS is an important feature of magnetosphere-ionosphere-thermosphere coupling that controls the evolution of large-scale features in the mid-latitude ionosphere such as the formation of density troughs [*Spiro et al.*, 1978] and storm enhanced density/plasmaspheric plumes [*Foster et al.*, 2002; *Goldstein et al.*, 2004; *Thomas et al.*, 2013].

Some of the earliest observations of strong westward flows in the sub-auroral ionosphere were reported by *Galperin et al.* [1974], these flows were typically associated with substorm activity [*Southwood and Wolf*, 1978; *Spiro et al.*, 1979]. More recent studies on SAPS [*Anderson et al.*, 1993, 2001; *Huang and Foster*, 2007; *Erickson et al.*, 2011] indicate that they are predominantly associated with disturbed geomagnetic conditions during which the equatorward edge of the ion precipitation boundary moves equatorward of the electron precipitation boundary [*Gussenhoven et al.*, 1987; *Heinemann et al.*, 1989]. This misalignment in the boundaries is thought to produce a polarization electric field.

Another consideration is that, Region-2 field aligned currents (FACs) flow into the

region collocated with the ion precipitation boundary in the pre-midnight sector of the ionosphere [*Klumpar*, 1979; *Anderson et al.*, 1993] and close with Region-1 FACs via the poleward-directed Pedersen currents. However, this current closure is hindered by the low conductivity of the sub-auroral ionosphere, resulting in large poleward-directed electric fields leading to the westward-directed $\mathbf{E} \times \mathbf{B}$ drifts observed in SAPS [*Anderson et al.*, 1993]. The Region-2 FACs are driven by pressure gradients inside the ring current [*Toffoletto et al.*, 2003] and these variations can have an influence on the electric fields in the SAPS channel [*Clausen et al.*, 2012a]. Additionally, *Anderson et al.* [1993, 2001] suggested that the strong electric fields result in a decrease in the conductivity of the region [*Schunk et al.*, 1976; *Banks and Yasuhara*, 1978] producing a positive feedback effect that allows the electric fields to grow even more. *Zheng et al.* [2008] used models of the mid-latitude trough and ring current to demonstrate that the low conductance in the sub-auroral region is critical to the large amplitudes observed in SAPS.

Statistical characterization of SAPS in the literature has primarily been based on measurements from either the ion drift meter (IDM) instrument onboard Defense Meteorological Satellite Program (DMSP) satellites [*Wang et al.*, 2008] or the Millstone Hill incoherent scatter radar [*Foster and Vo*, 2002; *Erickson et al.*, 2011]. *Wang et al.* [2008] investigated the effects of cross polar cap potential, conductivity integrated over sub-auroral flux tubes, and Dst on SAPS and found an exponential relationship between SAPS latitude and Dst. *Foster and Vo* [2002] analyzed two decades of Millstone Hill incoherent scatter radar (ISR) data and characterized the average magnetic latitude (MLAT)-magnetic local time (MLT) location of SAPS for different Kp index levels. A subsequent study by *Erickson et al.* [2011] found that the latitude of SAPS peak velocity decreases as a function of Dst and MLT.

The ability of the mid-latitude SuperDARN radars to make observations of SAPS was demonstrated for the first time by *Oksavik et al.* [2006], using measurements from the Wal-

lops Island (WAL) SuperDARN radar. A detailed analysis of the influence of magnetospheric dynamics and solar wind - magnetosphere coupling on a SAPS channel was presented by *Grocott et al.* [2011] using measurements from the Falkland Islands (FIR) SuperDARN radar in the southern hemisphere. *Kunduri et al.* [2012] used simultaneous measurements from the Blackstone (BKS) and WAL SuperDARN radars in the northern hemisphere and FIR radar in the southern hemisphere to analyze the degree of interhemispheric magnetic conjugacy observed in a SAPS channel. Finally, *Clausen et al.* [2012a] demonstrated the capability of the new mid-latitude SuperDARN radar chain to make simultaneous observations of velocities in a SAPS channel spanning more than six hours in MLT. In all cases, these studies demonstrated the utility of the SuperDARN radars for making large-scale continuous measurements of SAPS over extended time intervals and thereby provide an expanded picture of its spatiotemporal dynamics. However, all of these SuperDARN-based studies were focused on individual event periods. In this paper we present the first large-scale statistical study of SAPS using measurements from the mid-latitude SuperDARN radar chain, that span many hours of MLT in the North American sector. In particular, we characterize the variability observed in the occurrence, location, and intensity of SAPS flows with Dst.

4.2 Datasets

4.2.1 SuperDARN HF Radars

The primary dataset used in this study is measurements of ionospheric plasma drift observed by the mid-latitude SuperDARN HF radars [*Greenwald et al.*, 1985; *Chisham et al.*, 2007; *de Larquier et al.*, 2011; *Ribeiro et al.*, 2012]. SuperDARN radars observe coherent backscatter from decameter-scale irregularities aligned along the magnetic field. The Doppler shift of the backscattered signal is proportional to the line-of-sight component of the $\mathbf{E} \times \mathbf{B}$

plasma drift in the scattering region [*Ruohoniemi et al.*, 1987]. In standard operating mode, the radars scan through 16-24 beam directions covering an azimuth sector of at least 50°. The radar scan time is typically 1-2 minutes corresponding to a dwell time of 3.5 or 7 seconds per beam. The line-of-sight Doppler velocities measured by all SuperDARN radars during a full azimuth scan are routinely used to generate global ionospheric convection maps [*Ruohoniemi and Baker*, 1998]. The first mid-latitude radar at Wallops Island came into operation in 2005 and five other radars became operational by the end of 2010. Together, the six radars are capable of making measurements in the mid-latitude ionosphere across the entire North American sector [*de Larquier et al.*, 2011; *Ribeiro et al.*, 2012]. Figure 4.1 shows the fields-of-view (FoVs) of SuperDARN radars in the northern hemisphere (as of Jan-2012), overlayed on a map marked in magnetic coordinates. FoVs of the six mid-latitude radars making measurments over the North American sector are filled with orange color.

4.2.2 Polar Operational Environmental Satellites

To identify SAPS events accurately it is necessary to confirm that the flows are equatorward of the auroral oval. In this study, particle precipitation data from the Total Energy Detector (TED) instrument in the Space Environment Monitor (SEM) package onboard the National Oceanic and Atmospheric Administration (NOAA) POES satellites [*Evans and Greer*, 2000] were the primary source of information on the equatorward auroral oval boundary. Currently, there are 5 POES satellites (15, 16, 17, 18 and 19) operating in sun-synchronous orbit at an altitude of ∼800 km, with an orbital period of 101 min. The lack of frequent nightside passes and lesser number of satellites make the boundary determination difficult using the Defense Meteorological Satellite Program (DMSP) satellites. The TED instrument measures the energy flux carried into the Earth's atmosphere by precipitating particles with energy ranges between 50 eV and 20 KeV at a 16 sec time resolution. Note

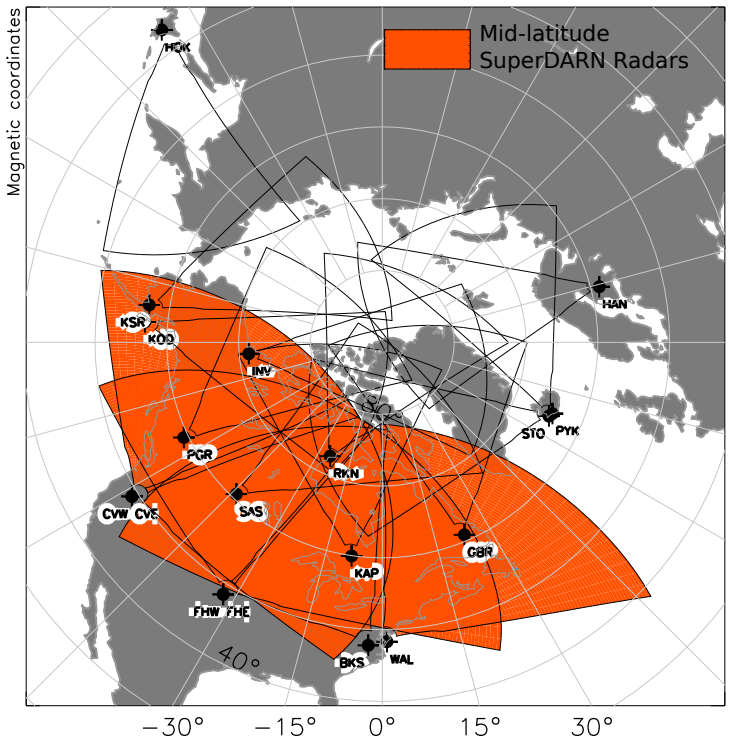

Figure 4.1: Fields-of-view of the SuperDARN radars located in the northern hemisphere (as of Jan-2012), overlayed on map marked in magnetic coordinates. The fields-of-view of the six North American mid-latitude radars are filled with orange color.

that the measured energy flux integrates over both ion and electron fluxes. To determine the equatorward edge of the auroral boundary, data from all the satellites (in the northern hemisphere) within +/- 40 minutes of the given time is considered. The MLT and magnetic latitude of the equatorward precipitation boundary is identified (when possible) at each available satellite orbit. A circular fitting function similar to the one described in *Clausen et al.* [2012b] is then applied to determine the boundary. Such a circular fit has been shown to be a good approximation of the equatorward precipitation boundary by *Gussenhoven et al.* [1983]. The SAPS features in this work were determined to lie equatorward of the location of equatorward auroral oval boundary as determined by this fitting.

4.2.3 Other Datasets

The ion and electron energy flux data measured by the SSJ/4 instrument [*Hardy*, 1984] on-board the DMSP spacecraft were used in some cases to determine the location of the equatorward boundary of the auroral oval determined from electron energy flux. The SSJ/4 instrument provides 1-second resolution measurements of ion and electron energy fluxes between 30 eV and 30 KeV [*Hardy*, 1984]. DMSP Special Sensor for Ions, Electron and Scintillation (SSIES) thermal plasma instrument package [*Rich and Hairston*, 1994] includes the IDM which measures the thermal ion velocity in the horizontal and vertical directions relative to spacecraft velocity. The data from IDM are used in some cases to verify the presence of a SAPS channel. Finally, SAPS events in the current study are characterized as a function of Dst, which is indicative of the strength of the ring current and is taken from selected magnetometer stations near the equator [*Sugiura*, 1964].

4.2.4 Example of a SAPS channel observed by SuperDARN radars

Figure 4.2 presents an example SAPS event (extending ∼6 hours in MLT) observed by North American mid-latitude SuperDARN radars on 18-June-2012 at 0245 UT. The fitted ionospheric ($\mathbf{E} \times \mathbf{B}$) convection velocities [*Ruohoniemi and Baker*, 1998] derived from mid-latitude SuperDARN radars are overlayed on a MLAT-MLT grid. Others overlaid are data from the TED instrument onboard the Polar Operational Environmental Satellites (POES) and the dashed black circle identifies the equatorward edge of the auroral oval boundary determined from TED data using the procedure described in Section 4.2.2. The boundary is seen to correspond to a steep decrease in energetic particle precipitation with decreasing latitude. Also overlaid on the plot is the ion drift meter data from DMSP F18 satellite between 0252 and 0300 UT along the satellite track. The DMSP IDM data shows two regions of westward-directed flows collocated with SuperDARN measurements. We now

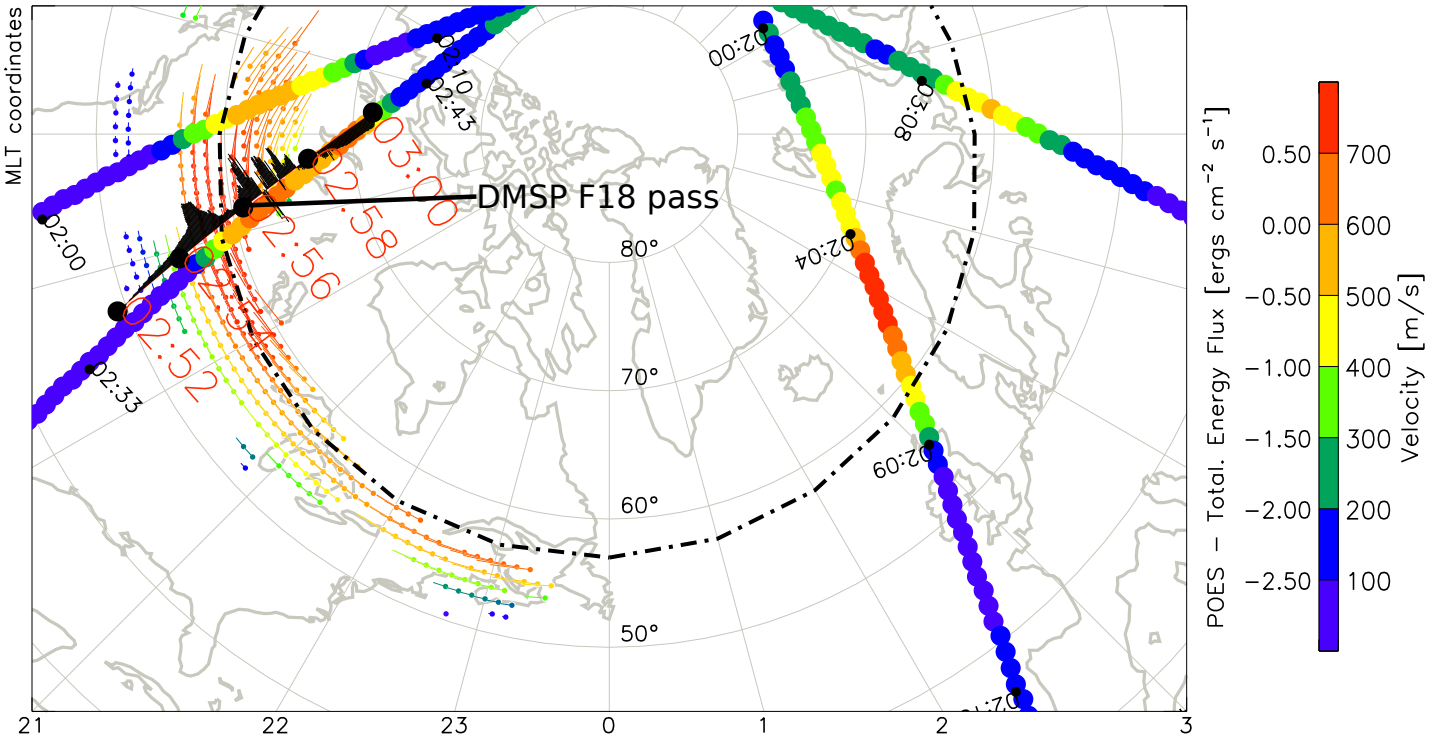

Figure 4.2: Large scale observations of SAPS in mid-latitude SuperDARN radars on June-18-2012 at 0245 UT. Vectors of convection flow derived from mid-latitude SuperDARN measurements are overlaid on a map marked in MLT-MLAT grid along with particle precipitation data from total energy detector (TED) instrument of POES satellites. The dashed black circle represents the equatorward edge of the auroral oval boundary determined by fitting a circle to the POES TED data. Also overlaid on the plot is ion drift meter data onboard DMSP F18 satellite (along the satellite track) between 0252 and 0300 UT on the same day.

compare the location of the equatorward auroral oval boundary determined from POES, SAPS observations in mid-latitude SuperDARN radars (located below POES boundary) with the data from the SSJ/4 instrument on board the DMSP F18 satellite. Figure 4.3 presents (from top to bottom) the time variations in SSJ/4 total electron energy flux data across the entire energy spectrum and the electron energy spectrograms respectively. The dashed black line marks the POES boundary (dashed black circle shown in Figure 4.2) at the location of the DMSP pass. It can be clearly noted that the POES boundary coincides with the DMSP F18 determination of the electron precipitation boundary and that the SuperDARN velocities and DMSP IDM measurements show strong SAPS-type westward

flows below this boundary.

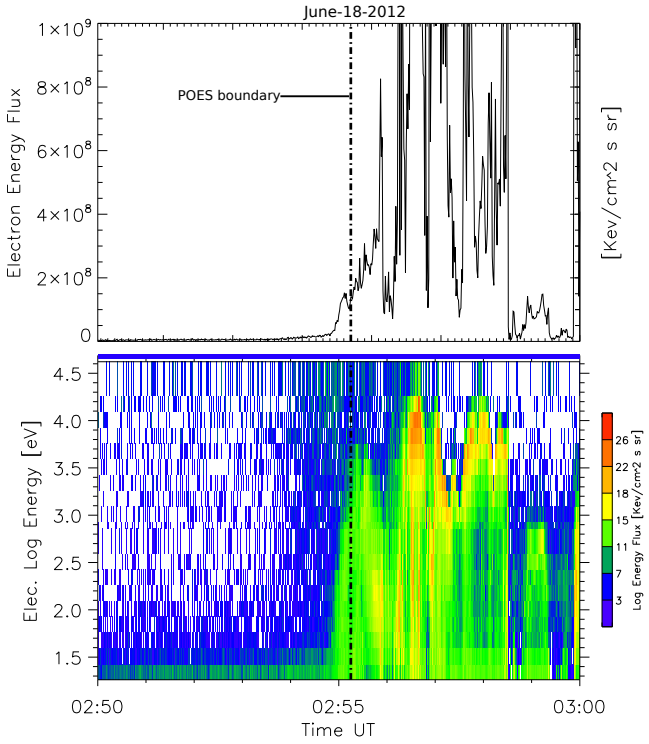

Figure 4.3: Time series data from SSJ/4 instrument onboard DMSP F18 satellite corresponding to the pass presented in Figure 4.2. Top panel shows total electron energy flux across the entire energy spectrum and the bottom panel shows electron energy spectrogram scaled according to the colorbar on the right. The dashed black line in the plot indicates the location of the equatorward auroral oval boundary determined from POES satellites (marked by dashed black circle in Figure 4.2) at the location of the satellite pass.

4.3 Observations

The primary focus of this paper is to analyze data from the mid-latitude SuperDARN radars to develop a statistical characterization of large-scale SAPS events. In this section, we present a statistical overview of the SAPS events observed between 01-Jan-2011 and 31-Aug-2012, a period of about 1.5 years.

4.3.1 Statistics of SAPS

To get an overview of the geomagnetic conditions during the study period, the minimum value reached by Dst between 0 and 12 UT on each day was noted. We limit ourselves to this UT interval because this is when mid-latitude SuperDARN radars in the North American sector are primarily in the dusk/midnight sector and likely to observe SAPS. 'True' vectors (derived from SuperDARN convection maps) were used to identify and characterize SAPS activity. True vectors are obtained by combining the line-of-sight velocity measurements within grid cells with the transverse (to the line-of-sight direction) component of the fitted vectors derived from the SuperDARN global convection maps [*Ruohoniemi and Baker*, 1998]. True vectors thereby provide a solution which is more consistent with the actual line-of-sight velocity measured within the cell than that provided by the global fitting routine. The velocities were classified as belonging to a SAPS channel when they were : (1) measured by at least one mid-latitude SuperDARN radar, (2) located below the equatorward boundary of the auroral oval (determined using data from POES satellites as described in Section 4.2.2), and (3) observed to have a predominantly westward direction (magnetic azimuth of -90° ± 15°) and a magnitude of at least 100 m/s. Additionally, to filter for long-lived and large-scale SAPS events, the number of data points below the estimated auroral oval boundary were checked. If the number of data points during the given day exceeded a threshold of 250 (determined by trial and error) then it was considered to be a large-scale "SAPS day".

Figure 4.4 shows a histogram of the percentage occurrence of these large-scale SAPS days observed between Jan-2011 and Aug-2012 at different Dst values. The numbers on the top of each bar show the number of days with SAPS observations during the given Dst range (left) and the number of days Dst reached that level (right). For example, Dst was observed to reach the range between -50 and -75 nT during 19 days and large-scale SAPS events were observed in mid-latitude SuperDARN radars during 18 of those days. It can be clearly seen

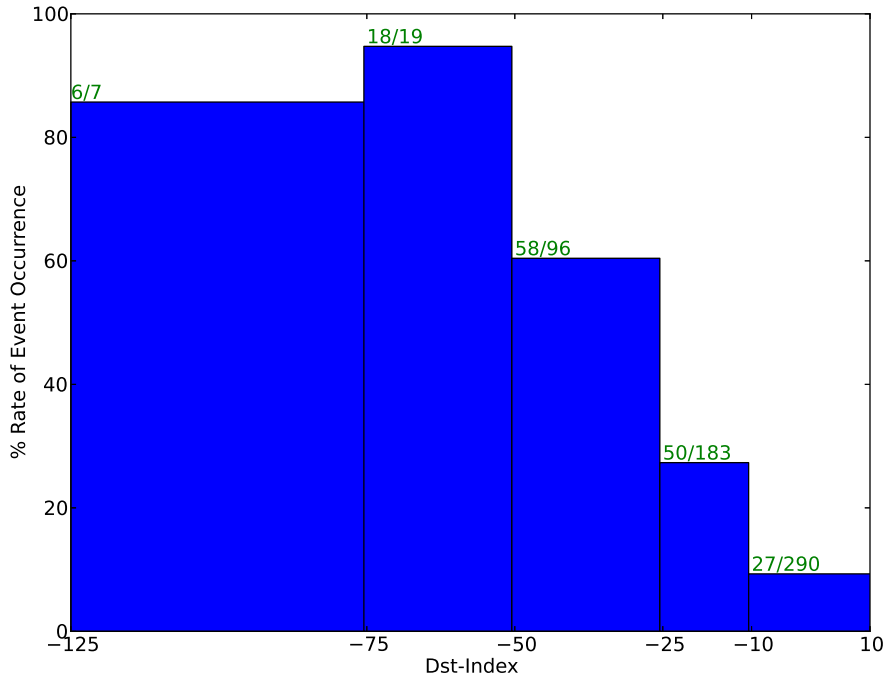

Figure 4.4: Probability occurrence rate of SAPS events seen by mid-latitude SuperDARN radars at different Dst ranges between Jan-2011 and Aug-2012. Numbers on the top of each bar indicate the number of days with SAPS observations during the Dst interval (left) and the number of days Dst was observed to reach that level (right).

that when Dst was less than -50 nT a SAPS event was almost certain to be observed by the mid-latitude SuperDARN radars ($> 80\%$ probability). For lesser Dst disturbance levels the probability of observing a SAPS event decreases but is still significant even at the lowest level ($\sim 10\%$) when Dst is between -10 and 10 nT. In total, 159 SAPS days were observed between Jan-2011 and Aug-2012 under widely varying geomagnetic conditions. Events were observed when Dst was greater than -10 nT and also when Dst was lower than -100 nT. In the next sections, we analyze and discuss the average location and velocity magnitude characteristics of the sub-auroral flows observed on these 159 SAPS days as a function of geomagnetic activity specified by Dst.

4.3.2 Average occurrence and velocity statistics of SAPS

A database consisting of the MLAT and MLT location, and true vectors (derived from fitted ionospheric $\mathbf{E} \times \mathbf{B}$ convection velocities) was built from the enumerated SAPS events. The data were grouped into the following Dst bins : 1) Dst > -10 nT, 2) -25 nT < Dst ≤ -10 nT, 3) -50 nT < Dst ≤ -25 nT, 4) -75 nT < Dst ≤ -50 nT 5) Dst ≤ - 75 nT. To produce a map of the average location of SAPS, the number of SAPS data points at each MLAT and MLT location for all the Dst bins were normalized on a scale between 0 and 1. Hereinafter, this "normalized count" of data points will be referred to as P_{SAPS} and is calculated as:

$$P_{SAPS} = N(MLAT, MLT, Dst)/Max[N(MLAT, MLT, Dst)] \tag{4.1}$$

where N(MLAT, MLT, Dst) represents the number of SAPS data points at a given MLAT and MLT location in a particular Dst bin and Max[N(MLAT, MLT, Dst)] represents the maximum number of data points at any location for that same Dst bin. Statistically, P_{SAPS} thus represents the likelihood of observing SAPS at a specific location and a given Dst value *when a SAPS event is underway* (The probability of occurrence of a SAPS event per se is given by Figure 4.4). Figure 4.5 shows the spatial distribution of P_{SAPS} for the five different Dst bins. All values of P_{SAPS} less than 0.25 have been discarded. Clearly, there is a strong dependence of SAPS location on Dst such that SAPS rotates from midnight to dusk as Dst decreases. For example, the most likely location to observe SAPS when Dst is between -10 and 10 nT is around 59° - 63° MLAT and 23 - 1 MLT; whereas the most likely location moves to 54° - 58° MLAT and 18 - 20 MLT when Dst drops below -75 nT. To simplify the comparison between Dst bins, Figure 4.6 presents the most likely latitudinal location (highest P_{SAPS}) of the channel at different MLTs and Dst levels. Similar to the trend observed in Figure 4.5, two important features can be observed. First, the equatorward and

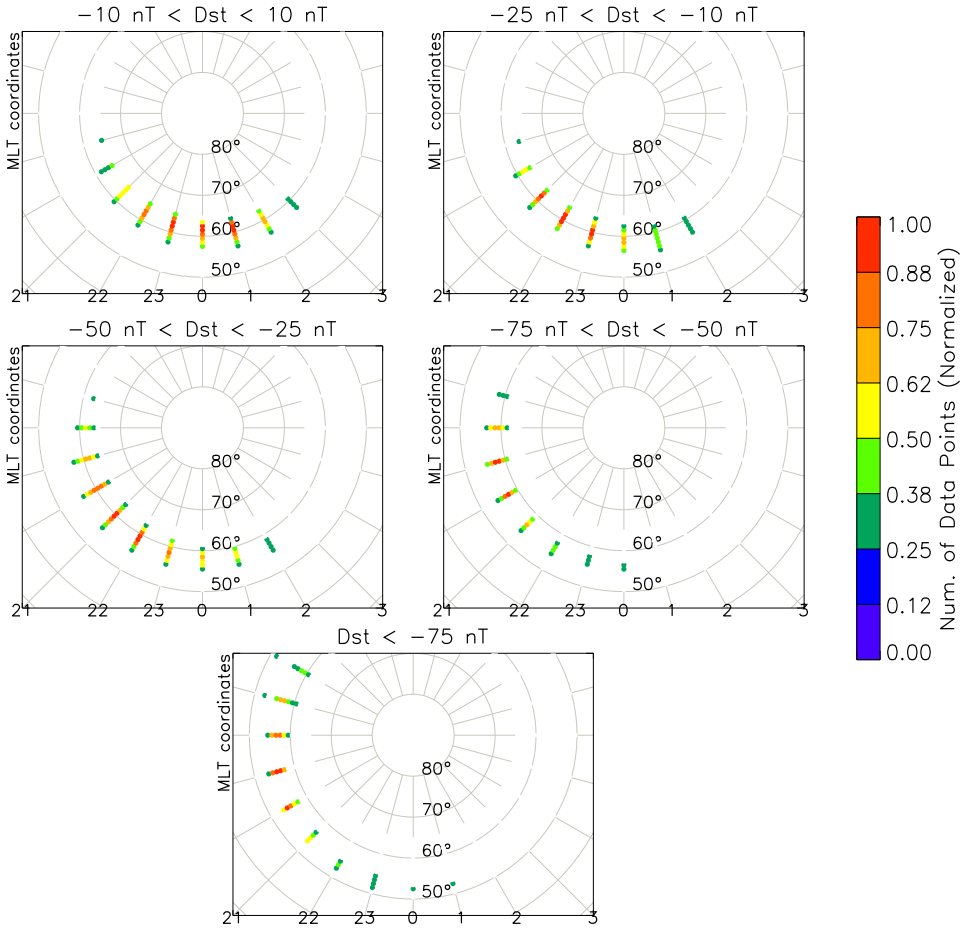

Figure 4.5: Spatial maps of the normalized number of data points (P_{SAPS}, refer text for details) at different Dst ranges scaled according to the colorbar at right. The Dst interval corresponding to each map is indicated on top of each panel.

duskward motion of the SAPS channel with decreasing Dst levels; second, for a given Dst level bin, the decrease in SAPS channel latitude with MLT. These features will be analyzed and discussed further in subsequent sections.

It is also interesting to examine the variations in velocity magnitude observed in the SAPS channel at the different Dst levels. Average velocity magnitudes calculated at the locations where P_{SAPS} is greater than 0.25 are shown in Figure 4.7 in a format similar to Figure 4.5. These velocity magnitudes have been calculated by taking the mean of the true velocities from all events in the database at a given MLAT/MLT location (for each

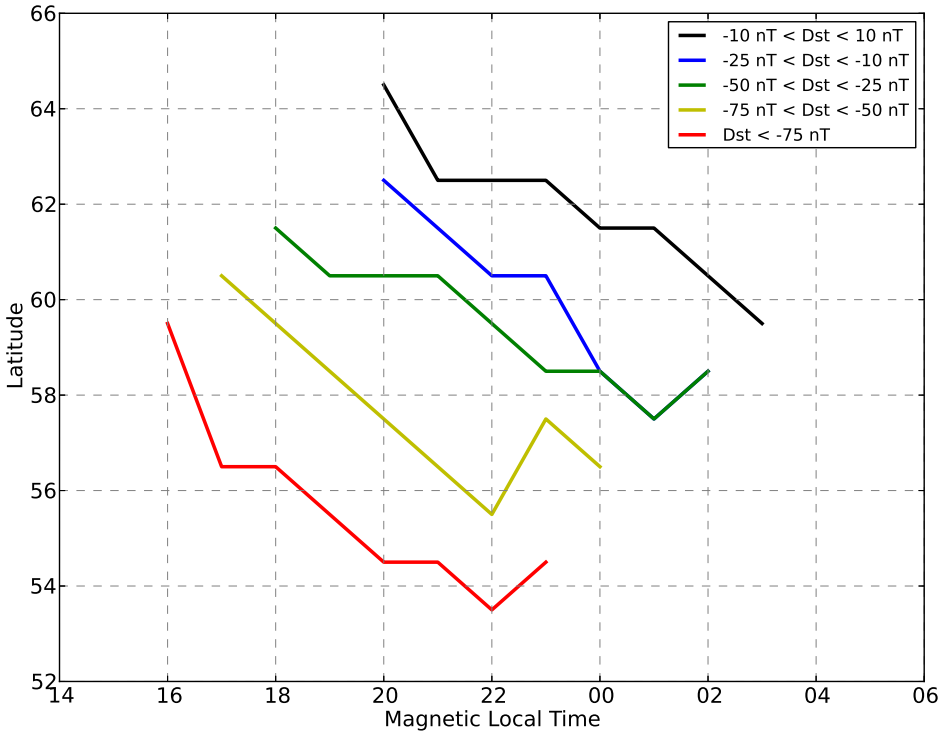

Figure 4.6: The most likely MLAT (vertical) vs MLT (horizontal) location of a SAPS channel at different Dst ranges (indicated by different colors).

Dst bin). It should be noted here that due to the spatial and temporal averaging used in deriving the convection maps [*Ruohoniemi and Baker*, 1998], some finer velocity features in the SAPS channel will be filtered out and velocity magnitudes underestimated. However, the main purpose of the current analysis is to get an overview of the velocities in the channel at different Dst bins and not a detailed examination of the finer features in the channel. A clear dependence of the velocity magnitude on Dst is observed such that the velocities increase in magnitude with decrease in Dst and the most intense velocities are observed more equatorward and duskward as Dst decreases.

Similar to what was done in Figure 4.6, Figure 4.8 presents the mean speeds in the

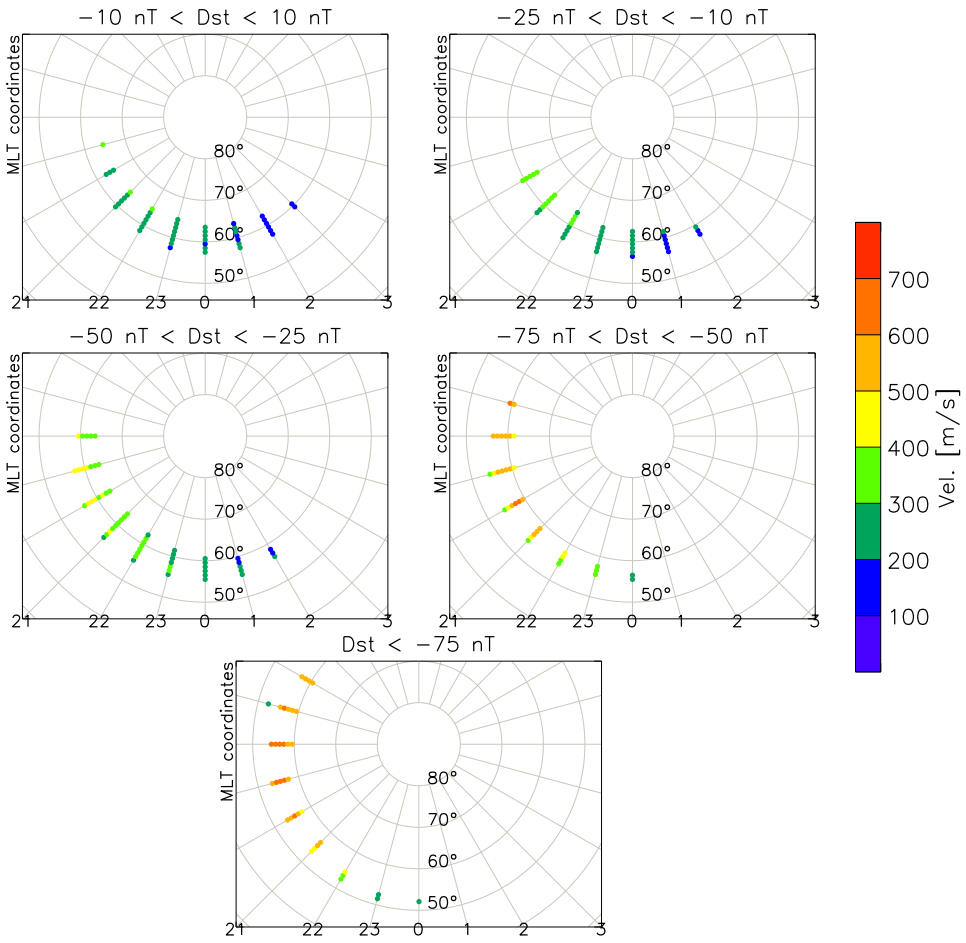

Figure 4.7: Spatial maps of the average velocity magnitude of SAPS at different Dst ranges. The figure is in the same format as Figure 4.5.

SAPS channel as a function of MLT at different Dst bins. Each circle identifies the average SAPS speed at a particular MLT location and Dst value, with the error bar indicating the standard deviation. As noted previously, several studies have found an exponential dependence of SAPS speed with MLT. With this in mind, the peak speeds have been fitted as an exponential function of MLT and are overlaid as solid lines on Figure 2.7, for the 3 Dst bins with higher values (Dst $>$ -10 nT, -25 nT $<$ Dst $\leq$ -10 nT, -50 nT $<$ Dst $\leq$ -25 nT). No good fit was observed for the two remaining Dst bins. Similar to the trend observed in Figure 4.7, the peak velocity magnitudes are higher for lower Dst bins (increasing geomagnetic activity) and duskward locations. These features will be discussed in detail and

compared with results from previous studies in the discussion section.

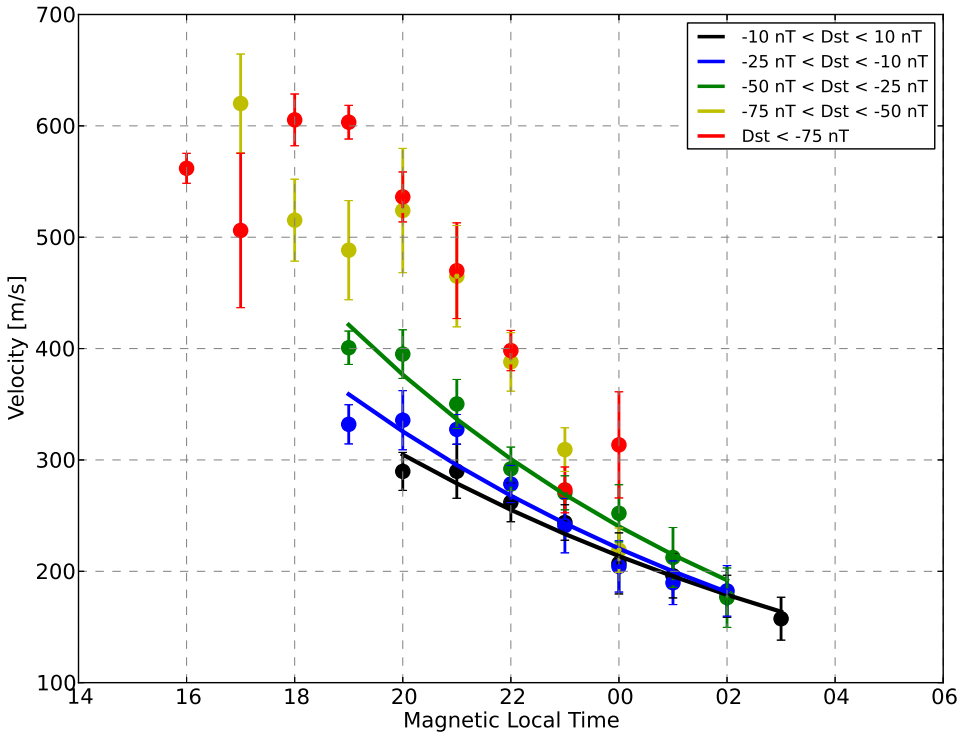

Figure 4.8: Variations in SAPS velocity magnitude as a function of MLT and Dst. The overplotted lines represent an exponential function derived from fitting the velocities within a particular Dst bin as a function of MLT. This has only been done for the 3 Dst bins which show a relatively clear exponential dependence. Each circle identifies the average SAPS speed at a particular MLT location (horizontal axis) corresponding to a particular Dst value (color). The error bars indicate the standard deviation in the speeds.

4.3.3 SAPS model

In the previous subsection, the dependence of the SAPS channel location on Dst was examined. In this section, we analyze the spatial variations observed in P_{SAPS} as a function of Dst and use a multivariate Gaussian function to develop an empirical model for the data to provide a concise summary of SAPS occurrence as a function of Dst. Among other

applications, such an empirical model could be useful in testing mechanisms of the formation and evolution of SAPS using MHD simulations.

Figure 4.5 shows the most likely location of the SAPS channel (where P_{SAPS} is > 0.75) is about 3° - 4° wide in latitude and 1 - 2 hours in MLT. An examination of the equatorward and duskward motion of this region with decreasing Dst indicates a Gaussian dependence. To this end, we fit the spatial variations in P_{SAPS} as a two dimensional (in MLAT and MLT) Gaussian function of Dst given by:

$$P_{SAPS} = Ae^{-(a(x-x_0)^2+2b(x-x_0)(y-y_0)+c(y-y_0)^2)} \tag{4.2}$$

Where, x = MLAT-57.5 and y = MLT - 24 (if MLT > 12) or MLT (otherwise) are the inputs and the coefficients are:

$$a = \frac{cos^2\theta}{2\sigma_x^2} + \frac{sin^2\theta}{2\sigma_y^2}$$
$$b = \frac{-sin2\theta}{4\sigma_x^2} + \frac{sin2\theta}{4\sigma_y^2}$$
$$c = \frac{sin^2\theta}{2\sigma_x^2} + \frac{cos^2\theta}{2\sigma_y^2}$$

These coefficients are then fit to the data as a linear function of Dst using the Levenburg-Marquardt algorithm to minimize the least squares error. The results of the fitting are found to be:

$$\theta = 0.633\, radians$$

$$\sigma_x = 2.93 + 2.67 \times 10^{-3} \times Dst$$

$$\sigma_y = 2.21 + 3 \times 10^{-3} \times Dst$$

$$x_0 = 3.86 + 6.03 \times 10^{-2} \times Dst$$

$$y_0 = -0.51 + 5.57 \times 10^{-2} \times Dst$$

$$A = 0.985 + 0.93 \times 10^{-3} \times Dst$$

The fitting results show that the peak location of SAPS channel moves more equatorwards (indicated by a decrease in 'x' direction) and duskwards (indicated by a decrease in 'y' direction) as the value of Dst becomes more negative (geomagnetic activity increases). Furthermore, the spread in P_{SAPS} (indicated by σ_x, σ_y) also decreases with Dst, suggesting the peak location of the SAPS channel becomes more narrow and focused as Dst decreases. Similar effects were observed in Figures 4.5 and 4.6.

Figure 4.9 shows the values of P_{SAPS} estimated using the Gaussian model (top panel), for the case when Dst lies between -25 and -50 nT compared with the actual values of P_{SAPS} (middle panel) shown in the corresponding panel of Figure 4.5. The bottom panel shows the difference between the model estimates and actual values (i.e, upper panel - lower panel). All values of P_{SAPS} are scaled according to the color bars on the right and the size of the dots such that higher values of P_{SAPS} are represented by more reddish colors and larger dots. It can be observed that the model reproduces the measured values reasonably well. The maximum error in probabilities estimated by the model at all the Dst bins was found to be less than 20%.

In summary, the values of P_{SAPS} were observed to conform to a Gaussian profiles in latitude and MLT and were successfully modeled as a multivariate Gaussian function of Dst.

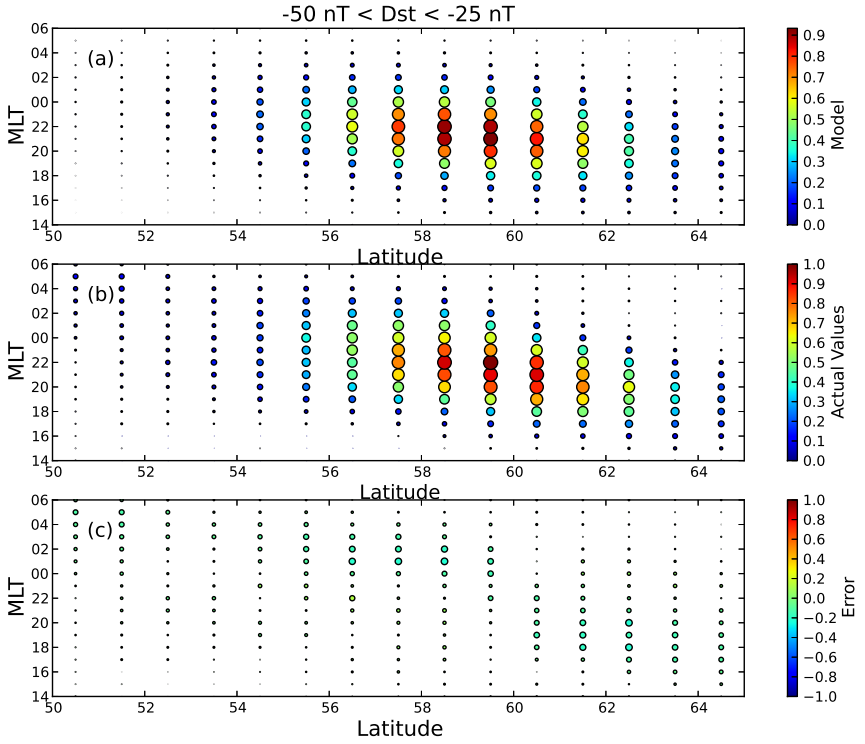

Figure 4.9: Empirical model of P_{SAPS} compared with data for the -50 < Dst < -25 bin (from top to bottom) : (a) Gaussian model, (b) Actual measurements of P_{SAPS} (Figure 4.5). All P_{SAPS} values are scaled according to the colorbar on the right and also with the size of the circle.

4.3.4 Model-Data Comparisons

In this section, we further test the SAPS model using three test cases where actual measurements from the mid-latitude SuperDARN radars or DMSP ion drift meter are compared with the location of SAPS predicted by the model. Of particular note is the fact that the test cases used here were observed after the date interval used to build the SAPS database for modeling (Jan-2011 to Aug-2012). Figure 4.10 presents a comparison between the actual measurements made during the 3 SAPS test events and model predictions. The top-left panel shows an event that occurred on Feb 14, 2013 at 5 UT when Dst was observed

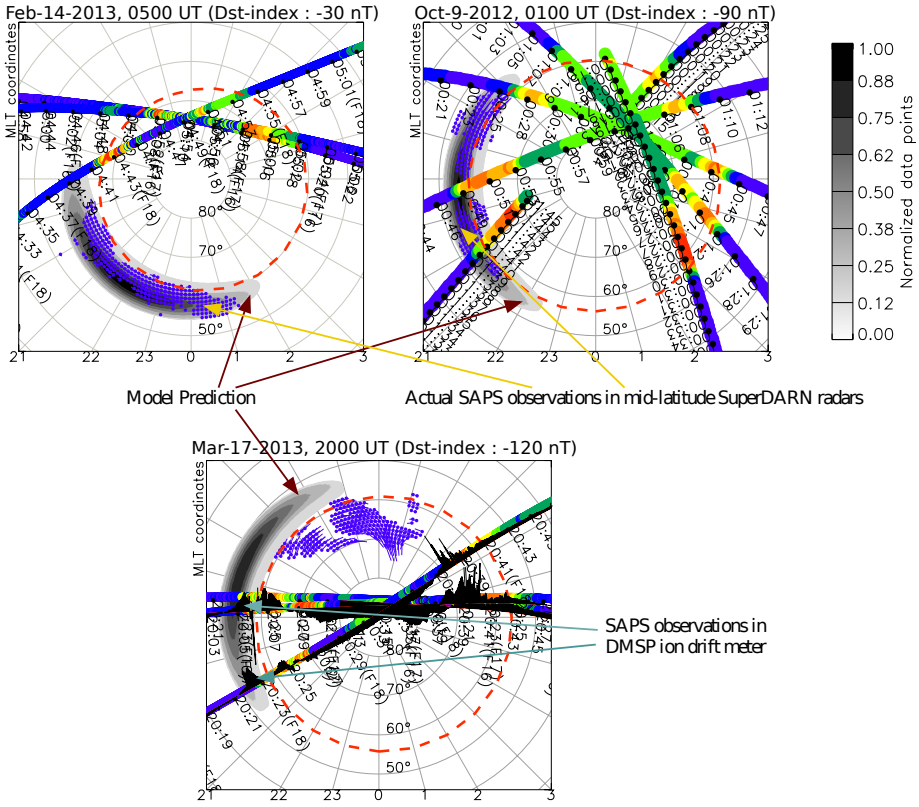

Figure 4.10: Model-Data comparisons for three SAPS events observed by mid-latitude SuperDARN radars during different Dst values. In each panel P_{SAPS} as predicted by the model is overlaid on a MLAT-MLT grid and compared with the data. Model P_{SAPS} values are scaled according to the color bar on the right. The violet colored vectors represent actual mid-latitude SuperDARN observations.The dotted red circle represents the equatorward edge of the auroral oval estimated using measurements from DMSP SSJ/4 instrument (first and last panels) or by POES TED instrument (middle panel).

to be about -30 nT. P_{SAPS} predicted by the model and the measurements made by mid-latitude SuperDARN radars are overlaid on a MLAT-MLT grid. P_{SAPS} values predicted by the model are represented in gray scale according to the colorbar on the right. The violet colored vectors represent the measurements made by the mid-latitude SuperDARN radars. Also overlaid are DMSP SSJ/4 particle precipitation data along the satellite tracks. The dashed red circle represents the equatorward auroral oval boundary estimated from DMSP data. The auroral oval boundary is estimated by manually overlaying a circle which best fits the locations where the DMSP satellites are observed to cross the electron precipitation

boundary. All mid-latitude SuperDARN measurements are observed below the estimated auroral oval boundary confirming the measurements are from a SAPS channel and agree well with the location predicted by the model. The top-right panel is plotted in the same format but for the event on Oct 9, 2012 at 01 UT. Dst exceeded -90 nT during this event. Instead of DMSP SSJ/4 data, POES data were used to estimate the equatorward auroral oval boundary during this event. Again, the model predictions agree well with the observations made by the radars. The bottom panel is for the event on Mar 17, 2013 at 20 UT when Dst reached -120 nT. In this case, the auroral oval reached latitudes so low that the mid-latitude radars were making measurements of auroral zone flows on the day-side rather than a SAPS channel. However, overlaid data from DMSP IDM clearly indicates a SAPS channel at a location in the dusk sector which agrees well with the model predictions based on SuperDARN data.

In summary, the SAPS model shows good agreement with actual observations made during three test cases representing a wide range of Dst values. Comparisons with DMSP observations provide independent confirmation of the nature of SAPS flows observed by the mid-latitude SuperDARN radars.

4.4 Discussion

In this paper we have examined the average location and speeds of SAPS channels observed by midlatitude SuperDARN radars during different Dst conditions. The peak location and speeds in the SAPS channel were shown to exhibit a strong dependence on Dst. In this section we analyze the trends observed in the location and speeds of the SAPS channel and compare them with the results presented in previous studies.

We begin with the variations observed in the location of the channel. Figures 4.5 and

4.6 clearly show two important trends in the SAPS location. First, for a given Dst bin, the SAPS channel is located at higher latitudes for more duskward MLTs. Second, the channel moves more equatorward and duskward as Dst decreases (increasing geomagnetic activity). *Erickson et al.* [2011] observed similar behavior in SAPS location using the Millstone Hill ISR dataset. They demonstrated that the location of the peak speed of the channel moves equatorwards with decreasing Dst as well as with MLT. *Foster and Vo* [2002] classified the Millstone Hill ISR SAPS dataset into different bins based on Kp index and presented similar results. Figure 3 of *Foster and Vo* [2002] clearly shows that the average latitude of the SAPS channel moves equatorward with increasing Kp index and that the channel is at higher latitudes for duskward MLTs. Similarly, a statistical study of SAPS using DMSP IDM data [*Wang et al.*, 2008] also showed that the SAPS channel moves equatorward with decreasing Dst. Using single events from SuperDARN radars, similar relations were noted between the latitudinal location of the SAPS channel and MLT [*Clausen et al.*, 2012a] and Sym-H and Asym-H indices [*Kunduri et al.*, 2012]. The partial ring current plays an important role in controlling the dynamics of the SAPS channel, especially during geomagnetic storms when the partial ring current is more pronounced [*Yeh et al.*, 1991; *Erickson et al.*, 2011]. The equatorward and duskward motion of the SAPS channel with increasing geomagnetic activity can be attributed to related displacements of the partial ring current as demonstrated in empirical models *Tsyganenko* [2002a, b] and particle simulations [*Liemohn et al.*, 2001]

Turning now from SAPS location to SAPS speeds, Figures 4.7 and 4.8 show that SAPS speed increases with decreasing Dst and is higher on the duskside, especially when Dst drops below -50 nT. Again, these observations are similar to the results presented in previous studies [*Foster and Vo*, 2002; *Erickson et al.*, 2011; *Clausen et al.*, 2012a]. *Clausen et al.* [2012a] attributed the MLT variations in SAPS channel flows to pressure gradients in the ring-current [*Toffoletto et al.*, 2003] which drive the field-aligned currents (which in turn

influence/drive the SAPS channel flows). Another important feature is that variability in peak speeds across MLTs increases with decreasing Dst. For example, when Dst is between -10 and -25 nT the speed drops by about 150 m/s between 20 and 2 MLT, whereas when Dst is between -50 and -75 nT the speed drops by about 400 m/s between 17 and 0 MLT. Furthermore, as shown in Figure 4.8, when Dst $<$ -50 nT SAPS speeds do not exhibit a simple exponential/quasi-linear behavior across MLTs. These factors suggest the possibility that increased thermosphere-ionosphere feedback in generation of electric fields in the SAPS channel may be distorting the functional dependence. One such factor may be the location of the day-night terminator in the ionosphere. Namely, as the activity level rises and the SAPS flow channel rotates further duskward the SAPS flows are more likely to cross the terminator where the increased ionospheric conductance would allow Region-2 current closure with reduced electric field magnitudes.

4.5 Summary and Conclusions

This paper has presented the first statistical analysis of SAPS based on midlatitude SuperDARN measurements. A statistical database of 159 SAPS days was compiled using data from mid-latitude SuperDARN radars. These SAPS events were then divided into different bins based on Dst. It was noted that large-scale SAPS was almost always observed by the mid-latitude SuperDARN radars during highly disturbed geomagnetic conditions and also observed for undisturbed conditions albeit at lower occurrence rates. The spatial occurrence statistics of the SAPS were examined and modeled as a function of Dst using a multivariate Gaussian function. It was noted that the average speed of the SAPS channel increased with decreasing Dst. The speeds were higher on the duskside and decreased toward midnight, especially during disturbed geomagnetic conditions. The average characteristics of the SAPS channel such as the equatorward motion of the channel with increasing geomagnetic activity

and higher speeds towards dusk are in general agreement with the results of previous studies. We have synthesized our observations into a functional empirical model of SAPS occurrence.

We note that the statistics and empirical model derived here can be applied to predict SAPS activity with a two-step procedure. First, the probability of a SAPS event for a given Dst level can be gauged from Figure 4.4. Next, the location of SAPS can be predicted using the P_{SAPS} occurrence statistics/empirical model represented in Figures 4.5 and 4.9. The prediction capability was demonstrated by application to events with DMSP coverage that occurred after the collection period of the statistical database. The empirical model provides a useful summary of SAPS occurrence which can be used to test MHD event simulations and different theories of SAPS formation.

Acknowledgments

The authors thank the National Science Foundation for support under grants ATM-0946900 and AGS-1150789. Dst index was obtained from the World Data Center in Kyoto. POES satellite data were accessed through the National Geophysical Data Center (NGDC) of the National Oceanic and Atmospheric Administration (NOAA), Boulder. The DMSP particle detectors were designed by Dave Hardy of AFRL and data obtained from JHU/APL. DMSP SSIES ion drift meter data is collected by the US Airforce weather agency and processed by NGDC of NOAA.

Chapter 5

Conclusions and Future Work

The motivation for this research was to gain better understanding of the role of interhemispheric magnetic conjugacy in magnetosphere-ionosphere coupling and to analyze the interaction between magnetosphere and ionosphere over large spatial scales. Interhemispheric measurements of ionospheric convection and large scale observations plasma flows in the mid-latitude ionosphere provided by SuperDARN radars were analyzed in this study.

In chapter 2, measurements of high velocity flows belonging to a subauroral polarization stream (SAPS) channel made by mid-latitude SuperDARN radars in both hemispheres with magnetically conjugate fields-of-view were presented. Previous studies demonstrate a strong relation between a SAPS channel and asymmetric ring current. Analysis of the flows showed that the latitudinal location of the channel in both the hemispheres exhibited a high degree of correlation with Asym-H index (indicative of the strength of the asymmetric ring current). However, a moderate degree of the correlation between the velocities in the channel (in both hemispheres) and the Asym-H index demonstrated the influence of local ionospheric conditions such as the Pedersen conductivity on the channel. However, an examination of the cross-SAPS potentials revealed that they were similar in both hemispheres. This indicates that interhemispheric conjugacy during this event was consistent in terms of potential variations while exhibiting significant differences in latitudinal extent and convection velocities. Future work on this topic may involve compiling a statistical database of magnetically

conjugate SAPS events not only from SuperDARN radars but from other instruments such as Ion Drift Meter (IDM) on board DMSP satellites and examining the variations observed between hemispheres as a function of season.

In the next chapter, an analysis of the degree of interhemispheric conjugacy in high latitude ionospheric convection on closed magnetic field lines was discussed. Of particular interest was the influence of IMF B_Y associated interhemispheric asymmetries on closed field lines. It was clearly demonstrated that when IMF B_Y was positive (negative) the convection velocities were higher in the northern (southern) hemisphere, irrespective of the season. These differences strongly suggest the presence of an interhemispheric asymmetry in ionospheric convection on closed magnetic field lines that can be attributed to the existence of IMF B_Y dependent interhemispheric currents. Future work on this topic may include a statistical study to characterize and quantify the nature of IMF B_Y associated interhemispheric asymmetries on ionospheric convection.

Finally, in chapter 4, a statistical database of 159 SAPS days binned by Dst was compiled using data from the mid-latitude SuperDARN radars. The statistics showed that a SAPS event was almost certainly observed in mid-latitude SuperDARN radars during disturbed geomagnetic conditions (Dst $<$ -50 nT). Furthermore, the spatial occurrence statistics of the SAPS were examined and modeled as a function of Dst using a multivariate Gaussian function. An analysis of the velocity magnitudes in the channel showed that the magnitudes increased with decreasing Dst. The speeds of SAPS flows were clearly higher on the duskside and decreased systematically towards mid-night. Future work on this topic may involve empirical modeling of SAPS velocities.

References

Anderson, P., R. Heelis, and W. Hanson (1991), The ionospheric signatures of rapid subauroral ion drifts, *J. Geophys. Res*, *96*(A4), 5785–5792.

Anderson, P., W. Hanson, R. Heelis, J. Craven, D. Baker, and L. Frank (1993), A proposed production model of rapid subauroral ion drifts and their relationship to substorm evolution, *J. Geophys. Res*, *98*(A4), 6069–6078.

Anderson, P., D. Carpenter, K. Tsuruda, T. Mukai, and F. Rich (2001), Multisatellite observations of rapid subauroral ion drifts (SAID), *J. Geophys. Res*, *106*(29,585).

Baker, D., S. Kanekal, V. Hoxie, M. Henderson, X. Li, H. Spence, S. Elkington, R. Friedel, J. Goldstein, M. Hudson, et al. (2013), A Long-Lived Relativistic Electron Storage Ring Embedded in Earth's Outer Van Allen Belt, *Science*, *340*(6129), 186–190.

Baker, J., R. Greenwald, J. Ruohoniemi, M. Förster, G. Paschmann, E. Donovan, N. Tsyganenko, J. Quinn, and A. Balogh (2004), Conjugate comparison of Super Dual Auroral Radar Network and Cluster electron drift instrument measurements of E× B plasma drift, *J. Geophys. Res*, *109*(A1), A01,209.

Banks, P., T. Araki, C. Clauer, J. Maurice, and J. Foster (1984), The interplanetary electric field, cleft currents and plasma convection in the polar caps, *Planet. space sci.*, *32*(12), 1551–1557.

Banks, P. M., and F. Yasuhara (1978), Electric fields and conductivity in the nighttime E-region: A new magnetosphere-ionosphere-atmosphere coupling effect, *Geophys. Res. Lett.*, *5*(12), 1047–1050.

Benkevich, L., W. Lyatsky, and L. Cogger (2000), Field-aligned currents between conjugate hemispheres, *J. Geophys. Res*, *105*(A12), 27,727–27.

Bilitza, D., and B. Reinisch (2008), International reference ionosphere 2007: improvements and new parameters, *Advances in Space Research*, *42*(4), 599–609.

Brandt, J. (1973), Introduction to the solar wind., *Introduction to the solar wind., by Brandt, J.. Translated from the English edition. Moskva: Mir, 207 p., 1.*

Burch, J., P. Reiff, J. Menietti, R. Heelis, W. Hanson, S. Shawhan, E. Shelley, M. Sugiura, D. Weimer, and J. Winningham (1985), IMF By-Dependent Plasma Flow and Birkeland

Currents in the Dayside Magnetosphere, 1. Dynamics Explorer Observations, *J. Geophys. Res*, *90*(A2), 1577–1593.

Chapman, S., and V. C. Ferraro (1930), A new theory of magnetic storms, *Nature*, *126*(3169), 129–130.

Chisham, G., M. Pinnock, A. Rodger, and J. Villain (2000), High-time resolution conjugate SuperDARN radar observations of the dayside convection response to changes in IMF B y, in *Ann. Geophys*, vol. 18, pp. 191–201, Springer.

Chisham, G., M. Lester, S. E. Milan, M. Freeman, W. Bristow, A. Grocott, K. McWilliams, J. Ruohoniemi, T. K. Yeoman, P. L. Dyson, et al. (2007), A decade of the Super Dual Auroral Radar Network (SuperDARN): Scientific achievements, new techniques and future directions, *Surveys in Geophysics*, *28*(1), 33–109.

Clauer, C., P. Banks, A. Smith, T. Jorgensen, E. Friis-Christensen, S. Vennerstrom, V. Wickwar, J. Kelly, J. Doupnik, and C. Stanford Univ. (1984), Observation of interplanetary magnetic field and of ionospheric plasma convection in the vicinity of the dayside polar cleft, *Geophys. Res. Lett*, *11*, 891–894.

Clausen, L., J. Baker, J. Ruohoniemi, R. Greenwald, E. Thomas, S. Shepherd, E. Talaat, W. Bristow, Y. Zheng, A. Coster, et al. (2012a), Large-scale observations of a subauroral polarization stream by midlatitude SuperDARN radars: Instantaneous longitudinal velocity variations, *Journal of Geophysical Research*, *117*(A5), A05,306.

Clausen, L., J. Baker, J. Ruohoniemi, S. Milan, and B. Anderson (2012b), Dynamics of the region 1 Birkeland current oval derived from the Active Magnetosphere and Planetary Electrodynamics Response Experiment (AMPERE), *J. Geophys. Res.*, *117*(A6).

Cowley, S., J. Morelli, and M. Lockwood (1991), Dependence of convective flows and particle precipitation in the high-latitude dayside ionosphere on the x and y components of the interplanetary magnetic field, *J. Geophys. Res.*, *96*(A4), 5557–5564.

Crooker, N. (1979), Dayside merging and cusp geometry, *J. Geophys. Res*, *84*(A3), 951–959.

de Larquier, S., J. Ruohoniemi, J. Baker, N. R. Varrier, and M. Lester (2011), First observations of the midlatitude evening anomaly using Super Dual Auroral Radar Network (SuperDARN) radars, *Journal of Geophysical Research*, *116*(A10), A10,321.

DeWitt, R. (1962), The occurrence of aurora in geomagnetically conjugate areas, *Journal of Geophysical Research*, *67*(4), 1347–1352.

Dungey, J. (1961), Interplanetary magnetic field and the auroral zones, *Physical Review Letters*, *6*(2), 47–48.

Erickson, P., F. Beroz, and M. Miskin (2011), Statistical characterization of the American sector subauroral polarization stream using incoherent scatter radar, *J. Geophys. Res*, *116*(null), A00J21.

Evans, D. S., and M. S. Greer (2000), *Polar Orbiting Environmental Satellite Space Environment Monitor-2: Instrument Description and Archive Data Documentation*, US Department of Commerce, National Oceanic and Atmospheric Administration, Oceanic and Atmospheric Research Laboratories, Space Environment Center.

Fedder, J., and J. Lyon (1987), The solar wind-magnetosphere-ionosphere current-voltage relationship, *Geophys. Res. Lett*, *14*(8), 880–883.

Feldsten, Y., and G. Starkov (1967), Dynamics of auroral belt and polar geomagnetic disturbances, *Planetary and Space Science*, *15*(2), 209–229.

Fillingim, M., G. Parks, H. Frey, T. Immel, and S. Mende (2005), Hemispheric asymmetry of the afternoon electron aurora, *Geophys. Res. Lett*, *32*(3), L03,113.

Finlay, C., S. Maus, C. Beggan, T. Bondar, A. Chambodut, T. Chernova, A. Chulliat, V. Golovkov, B. Hamilton, M. Hamoudi, et al. (2010), International geomagnetic reference field: the eleventh generation, *Geophysical Journal International*.

Foster, J. (1995), Radar observations of magnetosphere-ionosphere coupling at mid and high latitudes, *J. Geomag. and Geoelectr.*, *47*(8), 801–812.

Foster, J., and W. Burke (2002), SAPS: A new characterization for sub-auroral electric fields, *Eos Trans. AGU*, *83*(36), 393.

Foster, J., and F. Rich (1998), Prompt midlatitude electric field effects during severe geomagnetic storms, *J. Geophys. Res.*, *103*, 26.

Foster, J., and W. Rideout (2007), Storm enhanced density: magnetic conjugacy effects, in *Ann. Geophys*, vol. 25, pp. 1791–1799.

Foster, J., and H. Vo (2002), Average characteristics and activity dependence of the subauroral polarization stream, *J. Geophys. Res*, *107*, 1475.

Foster, J., P. Erickson, A. Coster, J. Goldstein, and F. Rich (2002), Ionospheric signatures of plasmaspheric tails, *Geophys. Res. Letters*, *29*(13), 1–1.

Frank, L., and J. Sigwarth (2003), Simultaneous images of the northern and southern auroras from the Polar spacecraft: An auroral substorm, *J. Geophys. Res*, *108*(A4), 8015.

Freeman, M., J. Ruohoniemi, and R. Greenwald (1991), The determination of time-stationary two-dimensional convection patterns with single-station radars, *J. Geophys. Res.*, *96*(A9), 15,735–15.

Freeman, M., D. Southwood, M. Lester, T. Yeoman, and G. Reeves (1992), Substorm-associated radar auroral surges, *J. Geophys. Res*, *97*(A8), 12,173–12.

Fujii, R., and T. Iijima (1987), Control of the ionospheric conductivities on large-scale Birkeland current intensities under geomagnetic quiet conditions, *J. Geophys. Res*, *92*(A5), 4505–4513.

Galperin, Y., V. Ponomarev, and A. Zosimova (1974), Direct measurements of ion drift velocity in the upper ionosphere during a magnetic storm. Part 2: Results of measurements during the November 3, 1967 magnetic storm, *Unknown*, *1*.

Goldstein, J., B. Sandel, M. Thomsen, M. Spasojević, and P. Reiff (2004), Simultaneous remote sensing and in situ observations of plasmaspheric drainage plumes, *Journal of geophysical research*, *109*(A3), A03,202.

Greenwald, R., K. Baker, R. Hutchins, and C. Hanuise (1985), An HF phased-array radar for studying small-scale structure in the high-latitude ionosphere, *Radio Science*, *20*(1), 63–79.

Grocott, A., S. Milan, J. Baker, M. Freeman, M. Lester, and T. Yeoman (2011), Dynamic sub-auroral ionospheric electric fields observed by the Falkland Islands radar during the course of a geomagnetic storm, *J. Geophys. Res*, *116*(A11), A11,202, doi: 10.1029/2011JA016763.

Guo, X., and C. Wang (2010), Effect of the dawn-dusk interplanetary magnetic field By on the field-aligned current system, *J. Geophys. Res*, *115*, A01,206.

Gussenhoven, M., D. Hardy, and W. Burke (1981), DMSP/F2 electron observations of equatorward auroral boundaries and their relationship to magnetospheric electric fields, *J. Geophys. Res*, *86*(A2), 768–778.

Gussenhoven, M., D. Hardy, and N. Heinemann (1983), Systematics of the equatorward diffuse auroral boundary, *Journal of Geophysical Research: Space Physics (1978–2012)*, *88*(A7), 5692–5708.

Gussenhoven, M., D. Hardy, and N. Heinemann (1987), The equatorward boundary of auroral ion precipitation, *Journal of Geophysical Research: Space Physics (1978–2012)*, *92*(A4), 3273–3283.

Hardy, D. (1984), Precipitating Electron and Ion Detectors (SSJ/4) for the Block 5D/flights 6-10 DMSP (Defense Meteorological Satellite Program) Satellites: Calibration and Data Presentation, *Tech. rep.*, DTIC Document.

Hardy, D., M. Gussenhoven, R. Raistrick, and W. McNeil (1987), Statistical and functional representations of the pattern of auroral energy flux, number flux, and conductivity, *J. Geophys. Res.*, *92*(A11), 12,275–12.

Heinemann, N., M. Gussenhoven, D. Hardy, F. Rich, and H. Yeh (1989), Electron/ion precipitation differences in relation to region 2 field-aligned currents, *J. Geophys. Res*, *94*(A10), 13,593–13.

Heppner, J., and N. Maynard (1987), Empirical high-latitude electric field models, *J. Geophys. Res*, *92*(A5), 4467–4489.

Huang, C., and J. Foster (2007), Correlation of the subauroral polarization streams (SAPS) with the Dst index during severe magnetic storms, *J. Geophys. Res*, *112*(A11), A11,302.

Hundhausen, A. J. (1972), Coronal expansion and solar wind, *Coronal Expansion and Solar Wind, XII, 238 pp. 101 figs.. Springer-Verlag Berlin Heidelberg New York. Also Physics and Chemistry in Space, volume 5*, *1*.

Iyemori, T. (1990), Storm-time magnetospheric currents inferred from mid-latitude geomagnetic field variations, *J. Geomag. Geoelectr*, *42*(11), 1249–1265.

Karlsson, T., G. Marklund, and L. Blomberg (1998), Subauroral electric fields observed by the Freja satellite: A statistical study, *J. Geophys. Res*, *103*(A3), 4327–4341.

Kelley, M. C. (2009), *The Earth's Ionosphere: Plasma Physics & Electrodynamics*, vol. 96, Access Online via Elsevier.

King, J., and N. Papitashvili (2005), Solar wind spatial scales in and comparisons of hourly Wind and ACE plasma and magnetic field data, *J. Geophys. Res.*, *110*(A2), A02,104.

Kivelson, M. G., and C. T. Russell (1995), *Introduction to space physics*, Cambridge university press.

Klumpar, D. (1979), Relationships between auroral particle distributions and magnetic field perturbations associated with field-aligned currents, *Journal of Geophysical Research: Space Physics (1978–2012)*, *84*(A11), 6524–6532.

Koustov, A., R. Drayton, R. Makarevich, K. McWilliams, J. St-Maurice, T. Kikuchi, and H. Frey (2006), Observations of high-velocity SAPS-like flows with the King Salmon SuperDARN radar, in *Ann. Geophys*, vol. 24, pp. 1591–1608.

Kozlovsky, A., A. Koustov, W. Lyatsky, J. Kangas, G. Parks, and D. Chua (2002), Ionospheric convection in the postnoon auroral oval: Super Dual Auroral Radar Network (SuperDARN) and polar ultraviolet imager (UVI) observations, *J. Geophys. Res*, *107*(12), 1433.

Kozlovsky, A., T. Turunen, A. Koustov, and G. Parks (2003), IMF By effects in the magnetospheric convection on closed magnetic field lines, *Geophys. Res. Lett*, *30*(24), 2261.

Kunduri, B., J. Baker, J. Ruohoniemi, L. Clausen, A. Grocott, E. Thomas, M. Freeman, and E. Talaat (2012), An examination of inter-hemispheric conjugacy in a subauroral polarization stream, *J. Geophys. Res.*, *117*(A8), A08,225.

Le, G., J. Slavin, and R. Strangeway (2010), Space Technology 5 observations of the imbalance of regions 1 and 2 field-aligned currents and its implication to the cross-polar cap Pedersen currents, *Journal of Geophysical Research: Space Physics (1978–2012)*, *115*(A7).

Leontyev, S., and W. Lyatsky (1974), Electric field and currents connected with Y-component of interplanetary magnetic field, *Planet. Space Sci.*, *22*(5), 811–819.

Liemohn, M., J. Kozyra, M. Thomsen, J. Roeder, G. Lu, J. Borovsky, and T. Cayton (2001), Dominant role of the asymmetric ring current in producing the stormtime Dst*, *Journal of Geophysical Research: Space Physics (1978–2012)*, *106*(A6), 10,883–10,904.

Lukianova, R., and A. Kozlovsky (2011), IMF By effects in the plasma flow at the polar cap boundary, *Annales Geophysicae-Atmospheres Hydrospheresand Space Sciences*, *29*(7), 1305.

Lukianova, R., A. Kozlovsky, and F. Christiansen (2010), Asymmetric structures of field-aligned currents and convection of ionospheric plasma controlled by the IMF azimuthal component and season of year, *Geomagnetism and Aeronomy*, *50*(5), 667–678.

Lyons, L. (1980), Generation of large-scale regions of auroral currents, electric potentials, and precipitation by the divergence of the convection electric field, *Journal of Geophysical Research: Space Physics (1978–2012)*, *85*(A1), 17–24.

Maeda, H. (1974), Field-aligned current induced by asymmetric dynamo action in the ionosphere, *J. Atmos. Terr. Phys.*, *36*(8), 1395–1401.

Makarevich, R., and P. Dyson (2008), Dual HF radar study of the subauroral polarization stream, in *Ann. Geophys*, vol. 25, pp. 2579–2591.

Mansurov, S. (1970), New evidence of a relationship between magnetic fields in space and on earth, *Geomagn. Aeron.*, *9*, 622.

Milan, S., L. Baddeley, M. Lester, and N. Sato (2001), A seasonal variation in the convection response to IMF orientation, *Geophys. Res. Lett*, *28*(3), 471–474.

Newell, P., J. Ruohoniemi, and C.-I. Meng (2004), Maps of precipitation by source region, binned by IMF, with inertial convection streamlines, *Journal of geophysical research*, *109*(A10), A10,206.

Ohtani, S., G. Ueno, T. Higuchi, and H. Kawano (2005), Annual and semiannual variations of the location and intensity of large-scale field-aligned currents, *J. Geophys. Res*, *110*.

Oksavik, K., R. Greenwald, J. Ruohoniemi, M. Hairston, L. Paxton, J. Baker, J. Gjerloev, and R. Barnes (2006), First observations of the temporal/spatial variation of the sub-auroral polarization stream from the SuperDARN Wallops HF radar, *Geophys. Res. Lett*, *33*.

Østgaard, N., S. Mende, H. Frey, T. Immel, L. Frank, J. Sigwarth, and T. Stubbs (2004), Interplanetary magnetic field control of the location of substorm onset and auroral features in the conjugate hemispheres, *J. Geophys. Res*, *109*.

Parker, E. N. (1963), Interplanetary dynamical processes., *New York, Interscience Publishers, 1963.*, *1*.

Parkinson, M., M. Pinnock, H. Ye, M. Hairston, J. Devlin, P. Dyson, R. Morris, and P. Ponomarenko (2003), On the lifetime and extent of an auroral westward flow channel (AWFC) observed during a magnetospheric substorm, in *Ann. Geophys.*, vol. 21, pp. 893–913.

Parkinson, M., M. Pinnock, J. Wild, M. Lester, T. Yeoman, S. Milan, H. Ye, J. Devlin, H. Frey, and T. Kikuchi (2005), Interhemispheric asymmetries in the occurrence of magnetically conjugate sub-auroral polarisation streams, in *Ann. Geophys*, vol. 23, pp. 1371–1390.

Parkinson, M., J. Wild, C. Waters, M. Lester, E. Lucek, and P. Décréau (2007), An auroral westward flow channel (AWFC) and its relationship to field-aligned current, ring current, and plasmapause location determined using multiple spacecraft observations, in *Ann. Geophys*, vol. 25, pp. 59–76.

Peng, Z., C. Wang, and Y. Hu (2010), Role of IMF Bx in the solar wind-magnetosphere-ionosphere coupling, *J. Geophys. Res*, *115*, A08,224.

Reiff, P., and J. Burch (1985), IMF By-dependent plasma flow and Birkeland currents in the dayside magnetosphere, 2. A global model for northward and southward IMF, *J. Geophys. Res*, *90*(A2), 1595–1609.

Ribeiro, A., J. Ruohoniemi, J. Baker, L. Clausen, R. Greenwald, and M. Lester (2012), A survey of plasma irregularities as seen by the midlatitude Blackstone SuperDARN radar, *J. Geophys. Res.*, *117*(A2).

Rich, F. J., and M. Hairston (1994), Large-scale convection patterns observed by DMSP, *J. Geophys. Res.*, *99*(A3), 3827–3844.

Ridley, A. (2007), Effects of seasonal changes in the ionospheric conductances on magnetospheric field-aligned currents, *Geophys. Res. Lett*, *34*(5), 5101.

Ridley, A., T. Gombosi, and D. DeZeeuw (2004), Ionospheric control of the magnetosphere: Conductance, in *Ann. Geophys*, vol. 22, pp. 567–584, Copernicus.

Robinson, R., R. Vondrak, K. Miller, T. Dabbs, and D. Hardy (1987), On calculating ionospheric conductances from the flux and energy of precipitating electrons, *J. Geophys. Res*, *92*(A3), 2565–2569.

Ruohoniemi, J., and K. Baker (1998), Large-scale imaging of high-latitude convection with Super Dual Auroral Radar Network HF radar observations, *J. Geophys. Res*, *103*(A9), 20,797–20.

Ruohoniemi, J., and R. Greenwald (1996), Statistical patterns of high-latitude convection obtained from Goose Bay HF radar observations, *J. Geophys. Res*, *101*, 21–21.

Ruohoniemi, J., R. Greenwald, K. Baker, J. Villain, and M. McCready (1987), Drift motions of small-scale irregularities in the high-latitude F region: An experimental comparison with plasma drift motions, *J. Geophys. Res*, *92*(A5), 4553–4564.

Sato, N., and T. Saemundson (1987), Conjugacy of electron auroras observed by all-sky cameras and scanning photometers. Mem. Natl Inst, *Polar Res., Spec. Issue*, *48*, 58–71.

Sato, N., T. Nagaoka, K. Hashimoto, and T. Saemundsson (1998), Conjugacy of isolated auroral arcs and nonconjugate auroral breakups, *J. Geophys. Res.*, *103*, 11.

Schunk, R., and A. Nagy (2009), *Ionospheres: physics, plasma physics, and chemistry*, Cambridge university press.

Schunk, R. W., P. M. Banks, and W. J. Raitt (1976), Effects of electric fields and other processes upon the nighttime high-latitude F layer, *J. Geophys. Res.*, *81*(19), 3271–3282.

Southwood, D., and R. Wolf (1978), An assessment of the role of precipitation in magnetospheric convection, *Journal of Geophysical Research: Space Physics (1978–2012)*, *83*(A11), 5227–5232.

Spiro, R., R. Heelis, and W. Hanson (1978), Ion convection and the formation of the mid-latitude F region ionization trough, *J. Geophys. Res.*, *83*(A9), 4255–4264.

Spiro, R., R. Heelis, and W. Hanson (1979), Rapid subauroral ion drifts observed by Atmosphere Explorer C, *Geophys. Res. Lett*, *6*(8), 657–660.

Stening, R. (1977), Field-aligned currents driven by the ionospheric dynamo, *J. Atmos. Terr. Phys.*, *39*(8), 933–937.

Sugiura, M. (1964), Hourly values of equatorial Dst for the IGY, *Ann. Int. Geophys. Yr.*, *35*.

Svalgaard, L. (1973), Polar cap magnetic variations and their relationship with the interplanetary magnetic sector structure, *J. Geophys. Res.*, *78*(13), 2064–2078.

Thomas, E., J. Baker, J. Ruohoniemi, L. Clausen, A. Coster, J. Foster, and P. Erickson (2013), Direct observations of the role of convection electric field in the formation of a polar tongue of ionization from storm enhanced density, *J. Geophys. Res.*

Toffoletto, F., S. SAZYKIN, R. SPIRO, and R. WOLF (2003), Inner magnetospheric modeling with the rice convection model, *Space science reviews*, *107*(1-2), 175–196.

Tsyganenko, N. (2002a), A model of the near magnetosphere with a dawn-dusk asymmetry 1. Mathematical structure, *J. Geophys. Res*, *107*(A8), 1176.

Tsyganenko, N. (2002b), A model of the near magnetosphere with a dawn-dusk asymmetry 2. Parameterization and fitting to observations, *Journal of Geophysical Research: Space Physics (1978–2012)*, *107*(A8), SMP–10.

Tsyganenko, N., and M. Sitnov (2005), Modeling the dynamics of the inner magnetosphere during strong geomagnetic storms, *J. Geophys. Res*, *110*(A3), 10.

Tsyganenko, N., and D. Stern (1996), Modeling the global magnetic field of the large-scale Birkeland current systems, *J. Geophys. Res*, *101*(A12), 27,187–27.

Tsyganenko, N., H. Singer, and J. Kasper (2003), Storm-time distortion of the inner magnetosphere: How severe can it get, *J. Geophys. Res*, *108*(10.1029).

Wang, H., A. J. Ridley, H. Lühr, M. W. Liemohn, and S. Y. Ma (2008), Statistical study of the subauroral polarization stream: Its dependence on the cross–polar cap potential and subauroral conductance, *J. Geophys. Res.*, *113*(A12), A12,311.

Weimer, D. R., C. Goertz, D. Gurnett, N. Maynard, and J. Burch (1985), Auroral zone electric fields from DE 1 and 2 at magnetic conjunctions, *Journal of Geophysical Research: Space Physics (1978–2012)*, *90*(A8), 7479–7494.

Yeh, H.-C., J. Foster, F. Rich, and W. Swider (1991), Storm time electric field penetration observed at mid-latitude, *Journal of Geophysical Research: Space Physics (1978–2012)*, *96*(A4), 5707–5721.

Zheng, Y., P. C. Brandt, A. T. Lui, and M.-C. Fok (2008), On ionospheric trough conductance and subauroral polarization streams: Simulation results, *Journal of Geophysical Research*, *113*(A4), A04,209.